UNIVERSITE DE NEUCHATEL INSTITUT DE PHYSIQUE

EXCLUSIVE NEUTRAL STRANGE PARTICLE PRODUCTION AT LARGE ANGLES IN π^-p AND $\bar{p}p$ REACTIONS BETWEEN 3 AND 12 GeV/c

THESE

présentée à la Faculté des Sciences
de l'Université de Neuchâtel
pour l'obtention du grade de docteur ès sciences

par

Reinhard SCHWARZ

I. Staatsexamen
in Physik und Mathematik
der Universität Stuttgart

1982

IMPRIMATUR POUR LA THÈSE

Exclusive Neutral Strange Particle Production

at Large Angles in π^-p and $\bar{p}p$ Reactions

Between 3 and 12 GeV/c

de Monsieur Reinhard Schwarz

UNIVERSITÉ DE NEUCHATEL

FACULTÉ DES SCIENCES

La Faculté des sciences de l'Université de Neuchâtel,
sur le rapport des membres du jury,

Messieurs E. Jeannet, J. Rossel, J.-M. Brunet
(Paris) et P. Sonderegger (Genève)

autorise l'impression de la présente thèse.

Neuchâtel, le 22 octobre 1982

Le doyen:

A. Aeschlimann

A) Aeschlimann

Faust:

Daß ich nicht mehr mit saurem Schweiß
Zu sagen brauche, was ich nicht weiß;
Daß ich erkenne, was die Welt
Im Innersten zusammenhält ...

Goethe

TABLE OF CONTENTS

1. INTRODUCTION

1. I N T R O D U C T I O N

The study of hadron-hadron collision at large angles and high energies has dramatically changed the picture of strong interaction dynamics and of deep hadronic structure during the last decade.

We shall present mainly results from the analysis of two hadronic reactions at large angles :

$$\pi^- p \rightarrow K^0 \Lambda \qquad (1)$$

and

$$\bar{p}p \rightarrow \bar{\Lambda}\Lambda \qquad (2)$$

at incident beam momenta between 3 and 12 GeV/c from a fixed target counter experiment.

STRONG INTERACTIONS IN THE 1970's

"Classical" hadronic experiments based on bubble chamber techniques were able to extensively investigate the small scattering angle region in a large variety of exclusive reaction channels.

A frequent strong forward peak in the differential cross section distribution and the existence of secondary dips and peaks could be described adequately by diffraction phenomena or by the exchange of mesons or baryons within the framework of Regge models. Higher energies, in general, are accessible in counter experiments for which we give an illustrative example in fig. 1-1 for the hypercharge exchange reaction (1) at 5 GeV/c (from ref. [WAR73] and [AST75]), the question mark symbolizing the domain of interest of this thesis.

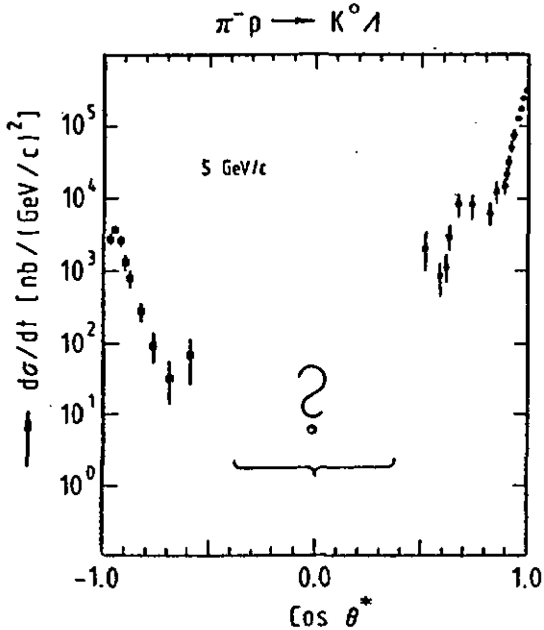

Fig. 1-1 : *Forward peak and backward region of the angular distribution of $\pi^-p \to K^0\Lambda$.*

The Regge model was also able to give predictions about the existence (or non-existence) of backward peaks according to whether or not the quantum numbers required for an exchanged object corresponded to an existing physical particle.

As a great surprise, early results from the ISR at CERN in 1973 showed that the probability of producing a particle with large transverse momentum p_T, though quite small, was actually several orders of magnitude higher than might have been expected on the basis of a simple extrapolation from small angle data. Thus, the fall-off in the invariant cross-section of inclusive π^0 production in p-p collisions at $\sqrt{s}$ = 52.7 GeV departed from the low transverse momentum exponential behaviour to a power law described by

$$E \frac{d^3\sigma}{dp^3} \sim p_T^{-m}$$

with $m = -(8.2 \pm .05)$ and p_T values up to ~ 8 GeV/c (see, e.g., the survey of experimental results in ref. [DAR80]).

This result stimulated fruitful "strong" interactions between theoretical developments and furthar experimental checks.

The first important candidate which was tested under the assumption of being able to account for the unexpected power law behaviour was the quark model, developed in the mid-sixties. It had already been successful in describing the spectroscopy of hadrons and their electromagnetic properties. In particular, electroproduction in the deep inelastic region led Bjorken (1969) to the formulation of the scaling behaviour of the nucleon structure functions, $F(x)$, with respect to the scaling variable

$$x = \frac{k_L}{p_{inc}} ,$$

where k_L is the longitudinal parton momentum. Also in 1969, Feynman proposed the parton model, according to which a hadron, when viewed in a frame in which it has infinite momentum, is composed of independent pointlike constituents (partons). An explicit parton model assumed the nucleon to contain "valence" quarks and "sea" quark-antiquark pairs.

As far as the above-mentioned power law behaviour of the ISR results is concerned, what are the predictions which can be made from the quark-parton model ?

If one supposes an underlying hard scattering process, as shown schematically in fig. 1-2, then three ingredients [FIE77] are necessary for a complete description of the collision process :

. the parton wave function, assumed to obey Bjorken scaling within the colliding hadrons (F),
. the scattering process describing the binary parton collision $\frac{d\bar{\sigma}}{d\bar{t}}$, and
. the fragmentation function (G) of the scattered partons, where G is assumed to be very similar to F.

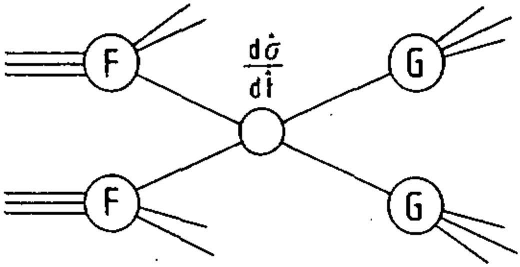

Fig. 1-2 : Hard scattering process.

If now the parton-parton interaction is assumed to be mediated via exchange of a photon or a vector gluon, the invariant cross section for hadron production would simply be :

$$E \frac{d^3\sigma}{dp^3} \sim p_T^{-4} \tag{1-1}$$

This is in clear contradiction to the experimental results.

A remedy was proposed in 1973 by the constituent interchange model (CIM) of Blankenbecler, Brodsky & Gunion (see ref. [GUN73]) which predicted the correct p_T dependence $\sim p_T^{-8}$. This prediction was based on the remark that the contribution of subprocesses such as :

$$M + q \longrightarrow M + q$$

where M and q stand for meson and quark partons respectively, might be dominant in large p_T hadronic interactions. Gluon exchange was believed to be suppressed.

But the CIM model did not only provide a description of inclusive processes; in their original paper, Blankenbecler et al. gave explicit formulae for the shape of the differential cross section at large angles and high energies for a large variety of exclusive hadronic processes. Their calculation led to a factorization of the following form :

$$\boxed{\frac{d\sigma}{dt} \sim s^{-n} \cdot f(t/s)} \tag{1-2}$$

The consequence of this prediction is twofold :

1. The shape of $d\sigma/dt$ only depends on the value t/s, i.e. asymptotically for large s and t, on the c.m.s. scattering angle θ^*.
2. At fixed angle θ^*, the differential cross section as a function of s should follow a simple power law.

EXCLUSIVE REACTIONS AT 90° CMS

Also in 1973 and independently from the CIM model Matveev, Muradyan & Tavkhelidze (see ref. [MAT73]) proposed the following form for the differential cross section at 90° c.m.s. which is based on dimensional considerations :

$$\boxed{\frac{d\sigma}{dt}\ (90^0\ \text{cms}) \sim s^{-(N-2)}} \qquad (1\text{-}3)$$

where N is the number of quarks inside the hadrons taking part in the collision. This is why eq. (1-3) is known as the <u>dimensional quark counting rule.</u> The example of an experimental test for the elastic reaction $pp \rightarrow pp$ is shown in fig. 1-3 [LAN73].

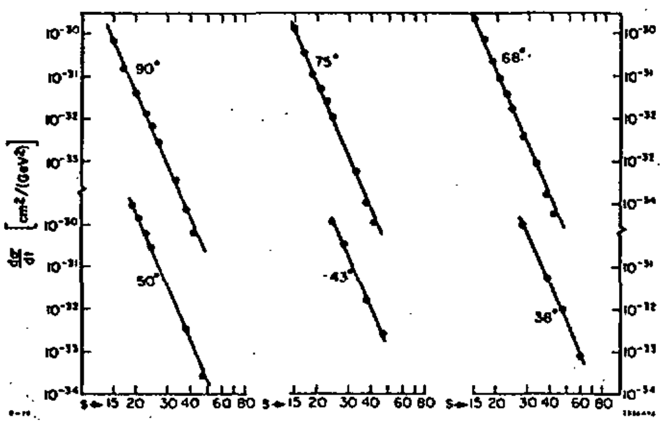

Fig. 1-3 : Test of power law s^{-10} for $pp \rightarrow pp$.

One of the goals of the WA13 experiment was to compare our results with predictions of the kind of eq. (1-2) and (1-3). The experiment was carried out at CERN in 1978, using the Omega spectrometer at the West Hall. Since we took advantage of the RF separated S1 beam line of the SPS, relatively high K^- and $\bar{p}$ beam intensitiea could be achieved and all the following reactions could be studied at beam momenta between 3 and 12 GeV/c :

Two-prong-reactions(*)

$$\pi^- p \rightarrow \pi^- p \tag{3}$$

$$K^- p \rightarrow K^- p$$

$$\bar{p}p \rightarrow \bar{p}p,\ K^-K^+,\ \pi^-\pi^+$$

Two-v^0-reactions

$$\pi^- p \rightarrow K^0\Lambda,\ K^0\Sigma^0$$

$$\bar{p}p \rightarrow \bar{\Lambda}\Lambda,\ \bar{\Lambda}\Sigma^0 + \text{c.c.}$$

POLARIZATION PHENOMENA

During analysis of the quasi-two-body reactions, which will be studied in this thesis, we could take advantage of the analysing power of the weak Λ-decay process in order to look for polarization phenomena. We will compare our resulta with predictions, where these exist, of the models presented above.

The importance of the measurement of spin effects is based on the fact that polarization is an observable depending on the difference in phase

---

(*) The analysis of the two body reactions (3) was assured mainly by our colleagues at the Collège de France in Paris, and the corresponding results are described in detail in the ref. [BIL82].

of helicity amplitudes. It enables one to detect non-leading amplitudes in the differential cross sections. The sensitivity of polarization phenomena as a function of s and t makes them a severe test for theoretical models.

It is interesting to note results on inclusive Λ-production in p-p interactions at 400 GeV/c from an experiment at Fermilab [HEL78], where a considerable negative Λ-polarization is reported which increases with transverse momentum p_T, their maximum p_T-value is $\sim$ 2.0 GeV/c. The authors suggest a gluon bremsstrahlung mechanism to be responsible for the polarization and the high p_T of the strange quark in the Λ-particle.

COULD QCD RESOLVE THE ISR PUZZLE ?

A final remark must be made as to recent results from inclusive π^0 production at the ISR. Angelis et al. [ANG78] reported in 1978 the behaviour of the invariant cross section for p_T values up to 16 GeV/c. It turned out that the p_T^{-8} scaling law is unable to describe the data, constituting a serious draw-back for the CIM model as far as this p_T range is concerned. On the other hand, since lower powers are measured (typically p_T^{-6}) one could hope to start sensing the gluon exchange quark-quark diagrams. This would support the idea that large p_T hadronic processes can be fully understood in the framework of QCD. Then all possible contributions from quark-quark, quark-gluon, and gluon-gluon interactions have to be taken into account [CON78].

The maximum p_T values in WA13 are $\sim$ 2.2 GeV/c. From Heisenberg's relation :

$$b \cdot p_T = \hbar = .197 \text{ GeV/c Fermi} \qquad (1-4)$$

we can deduce that this p_T value corresponds to objects of the size of 1/10 Fermi. As we have seen, ISR experiments cover a much larger p_T range. Hence our experiment seems to cover an intermediate region between diffractive processes and hard scattering processes.

We have organized the presentation of this thesis as follows :

In chapter 2, the reader will be made familiar with the hardware of our experiment, that is the Omega spectrometer itself and the labyrinth of electronics around it.

Chapter 3 will look in some detail into important parts of the software used for the off-line event reconstruction. Kinematical fits testing particle and reaction hypotheses will be the subject of chapter 4.

In order to be able to translate the raw angular distributions obtained after the kinematical analysis, we need a precise knowledge of the geometrical acceptance of the spectrometer and of various normalization factors. These calculations are done in chapter 5.

Results on differential cross sections and polarization data are presented in chapter 6, and they will be discussed and compared to theoretical models and to results from other experiments in chapter 7. Finally we conclude in chapter 8 with a summary of the subject discussed.

* * *

This is a notice for a "busy" reader : One can hurry along the different chapters by just reading the summarising introductory remarks without losing the logical sequence of the presentation and settle down more quietly at sections of special interest.

2. EXPERIMENTAL CONFIGURATION

2. EXPERIMENTAL CONFIGURATION

The heart of the experimental setup for WA13 was the Omega spectrometer situated in the RF separated S1 beam line in the West Hall at CERN. Counter experiments rún at Omega can take advantage of the powerful magnetic field of up to 18 kGauss produced by superconducting coils inside a 1.5 m gap and of the geometrical acceptance of virtually 4π.

In this chapter we shall describe the S1 beam characteristics, the experimental setup inside and around the Omega spectrometer including a special trigger chamber, and the data acquisition system which was designed for multiuser operation.

2.1 S1 Beam in West Hall

Protons accelerated to 200 GeV/c at the CERN SPS were guided on to a primary beryllium target producing secondary charged particles with maximum momentum of 40 GeV/c. It is the S1 beam line which assures the transport of particles of selected charge and momentum to the Omega spectrometer over a distance of about 230 m (see fig. 2-1). The beam is controlled mainly by 21 quadrupole magnets, 7 bending magnets, and several sextupole magnets.

The beam intensity and the ratio between different types of particles produced in the primary target was strongly dependent on the momentum chosen for a given period of the experiment. Design values for an unseparated beam as given in [PLA76] at a beam momentum $P_{lab} = -12$ GeV/c and during SPS operation at 10^{12} ppp (particles per pulse) were, for example :

π^-	K^-	$\bar{p}$
200×10^6	2.6×10^6	3×10^6

Hence a ratio $\pi^-/\bar{p}$ of about 67.

How this ratio could be brought down to values which assured a high intensity $\bar{p}$-beam with relatively low π^- content shall be presented in the next section.

Two Čerenkov counters Č2 and Č3 were used for particle identification. As an example, we give the operational values for $p_{lab} = -12$ GeV/c :

	HT	gas filling	signature
Č2	1.120 kV	CO_2 at 3 atm	π^- and K^-
Č3	2.100 kV	N_2 at 1.4 atm	π^-

Thus the identification of a particle which had been signaled by scintillator counters in the beam line (giving rise to a signal B) was possible from the following definitions:

$$\pi^- = \check{C}2 \cdot \check{C}3 \cdot B$$

$$K^- = \check{C}2 \cdot \overline{\check{C}3} \cdot B$$

$$\bar{p} = \overline{\check{C}2} \cdot \overline{\check{C}3} \cdot B$$

A possibility to reduce the electron content of the beam without affecting the $\bar{p}$ intensity was to put a thin sheet (2-4 mm) of lead in the beam line where electrons lost energy due to bremsstrahlung.

Small inefficiencies of the Č-counters and possible misidentifications had to be corrected during normalization of the results for each momentum separately.

(a)

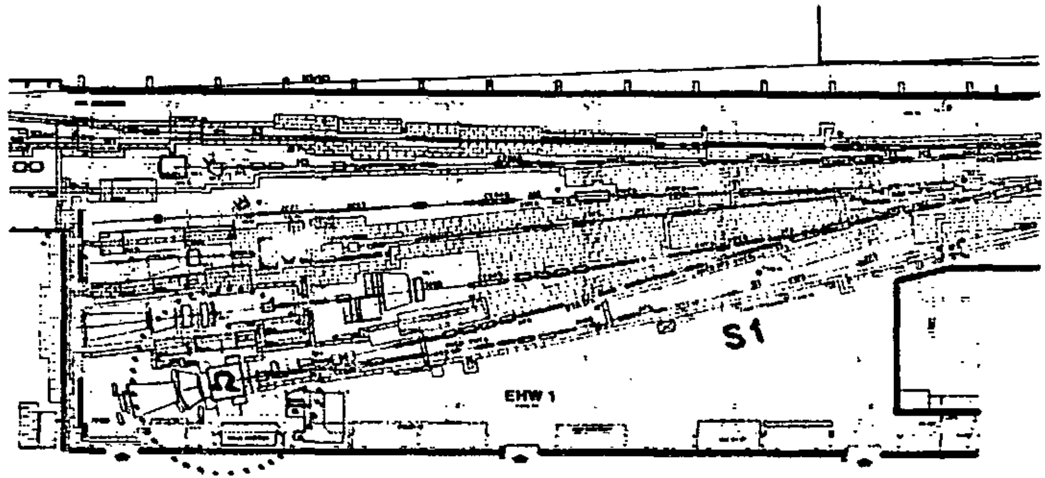

(b)

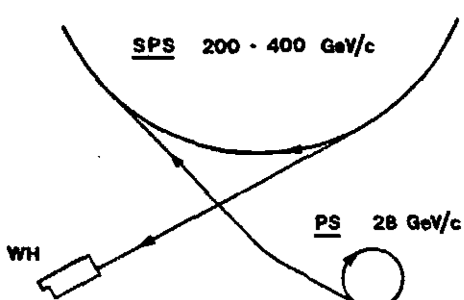

Fig. 2-1 : (a) S1 beam line in the West Hall at CERN.

(b) Acceleration of protons in the Proton Synchrotron (PS) and the Super Proton Synchrotron (SPS), arrival at the West Hall (WH).

2.2 RF-Separator

The composition of the S1 beam after the primary target was characterized by an abundance of π^- particles. The RF separator was designed to enrich the contents of K^- and $\bar{p}$ particles in the beam. Several experiments at Omega have taken advantage of this facility (see ref. [GAG78]) since its installation in 1977.

The principle of one of the possible operation modes of the separator is shown in fig. 2-2 : Two cavities, each 2.74 m long, are installed in the beam line and operated at a temperature of 1.8°K (superfluid He-II). Two 1 kW RF-generators at 2'855 MHz create a deflecting field which results in a transverse momentum component of the beam particles of about 2 MeV/c.

Due to the difference in time of flight between the cavities for particles of different mass, they acquire a phase slip relative to each other. The relative phase of the deflectors is adjusted in order to cancel the deflection of unwanted particles. A central beam stopper behind the second RF cavity then stops the unwanted particles whereas most of the wanted particles are deflected above and below and are brought to the detector.

Whenever the relative phase of the wanted and the unwanted particles is a multiple of 2π, no separation is possible. For instance, no separation is possible between $\bar{p}$ and π^- at 13.1 GeV/c. Below about 8 GeV/c and at high intensity, electrons represent an important fraction of the beam; $\pi^-/\bar{p}$ separation must then be considered in a compromise with minimum electron intensity.

As is indicated in fig. 2-2 (b) at p_{lab} = - 11.7 GeV/c, we used a relative phase PHI = 151°, which gave the following particle intensities at $1.9 \cdot 10^{12}$ ppp on T1 :

π^-	K^-	$\bar{p}$
570 000	250 000	750 000

The ratio $\pi^-/\bar{p}$ of about 0.8 shows that an excellent relative enrichment of $\bar{p}$ in the beam was achieved at this energy.

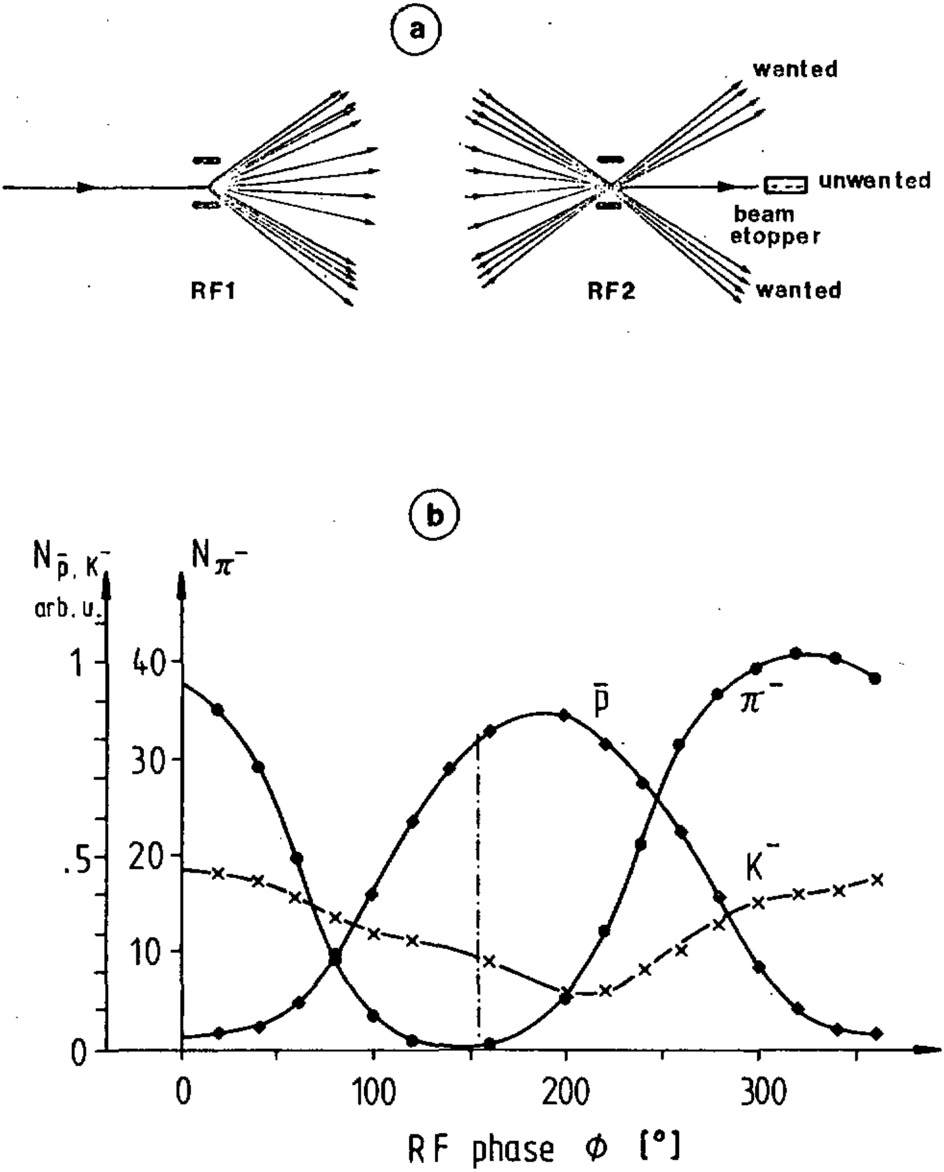

Fig. 2-2 : *(a) Principle of RF separation.*
(b) Particle intensities as a function of RF phase.

2.3 Omega Spectrometer

For WA13, the Omega spectrometer was equipped with spark chamber modules inside the magnet gap. In a later version (1979), the optical chambers and their associated stereoscopic video camera system were replaced by multiwire proportional chambers, the spectrometer being called Ω' since then.

Superconducting magnet coils produce inside the 1.5 m gap of Ω a relatively homogeneous field of up to 18 kGauss. The average power consumption of Ω with all its cryogenica around is roughly 600 kW. For beam energies below 5 GeV/c, the magnetic field was scaled accordingly for WA13, as listed in the table below :

p_{lab} (GeV/c)	Current (A)	Field (kG)
3.0	2904	11.00
3.1	3015	11.42
3.2	3102	11.75
3.3	3168	12.00
4.95	4800	18.18
7.8	4800	18.18
11.7	4800	18.18

Table 2-1 : Omega magnetic field.

The Ω coordinate system will be used throughout the following chapters. It has the x-axis along the beam direction, the positive y-axis pointing to the left of the beam, and the z-axis vertically in upward direction. The origin (0,0,0) coincides with the geometrical center of the Ω magnet. For WA13 negative incoming beam particles were deflected to the right in a horizontal plane, i.e. the Ω was operated with a negative magnetic field.

A photograph taken in the early days of Ω is reproduced in fig. 2-3 (a). One can distinguish the spark chamber modules withdrawn from the magnet core. Also visible in the top left corner are the bending magnets of the S1 beam line before entering the spectrometer.

2.3.1 Experimental Lay-Out

A top view of the experimental lay-out for WA13 is shown in fig. 2-3 (b). The set of optical chambers is divided into two groups :

- . Geometry I region : 7 optical modules with spark chamber gaps perpendicular to the beam direction and thus detecting forward outgoing tracks (fig. 2-4 (a)),
- . Geometry II region : with 8 modules installed to left and right of the target (fig. 2-4 (b)).

A minimum amount of material was used for the construction of the spark chambers. Thin layers of aluminum foil (25 μm) as electrode material and the supporting structure of a 10 gap Geometry I module correspond to a radiation length equivalent of $L_r \approx 35$ m. The Geometry II modules had only 8 gaps each and a value of $L_r \approx 60$ m.

After event occurrence, the optical chambers are "fired" by switching on a high tension pulse of 12 and 13 kV. This happened only if the electronics trigger had decided to record this event.

In comparison to a standard bubble chamber experiment, this technique has the advantage of recording only "good" event candidates. On the

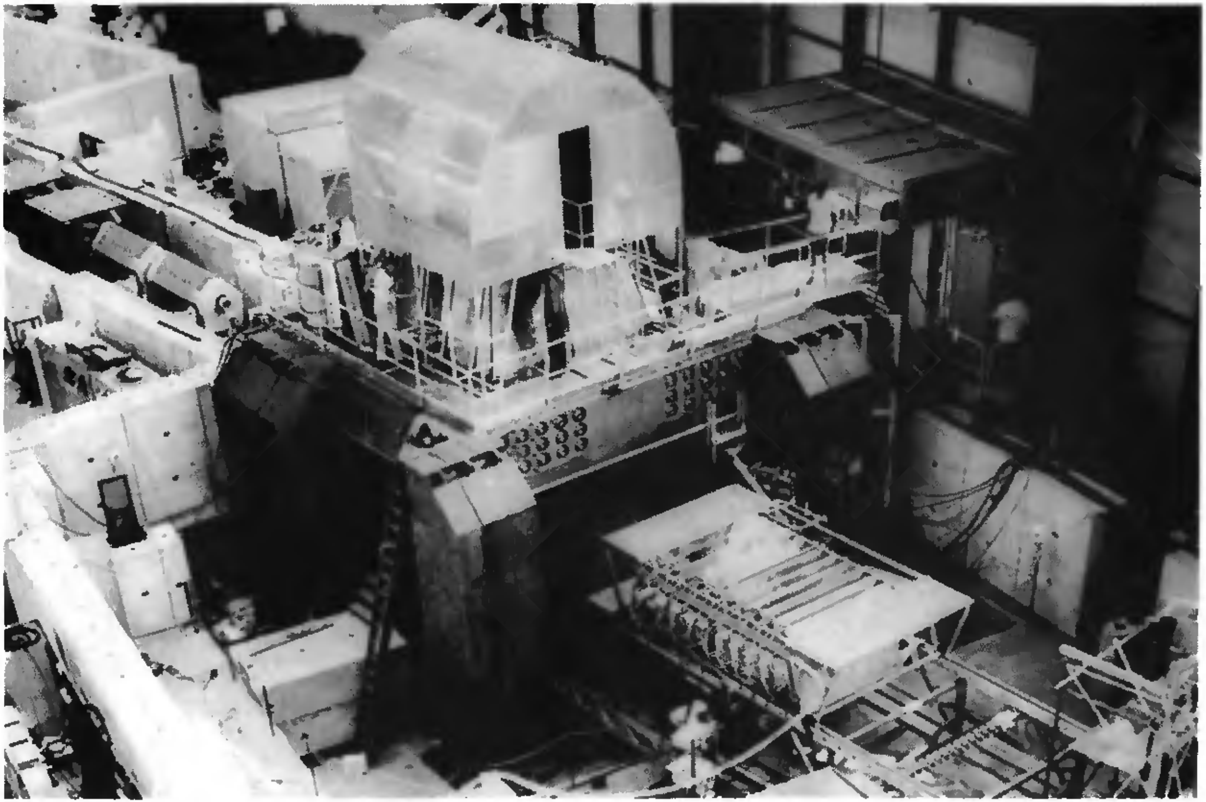

<u>Fig. 2-3</u> : (a) The Ω spectrometer in its early days (courtesy CERN Public Information Office).

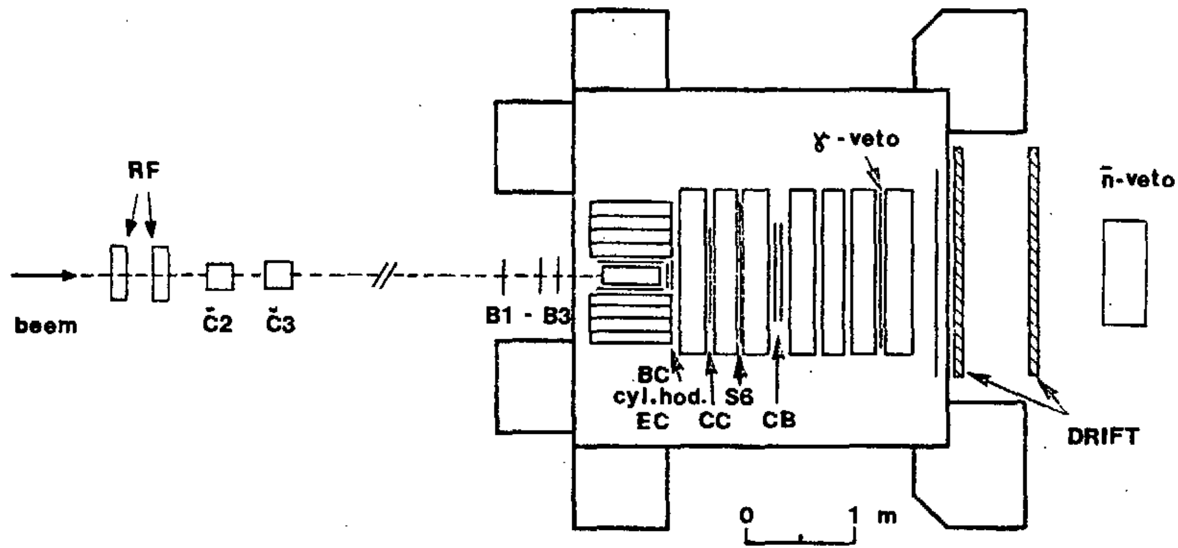

Fig. 2-3 (cont.) : *(b) Top view of WA13 experimental lay-out.*

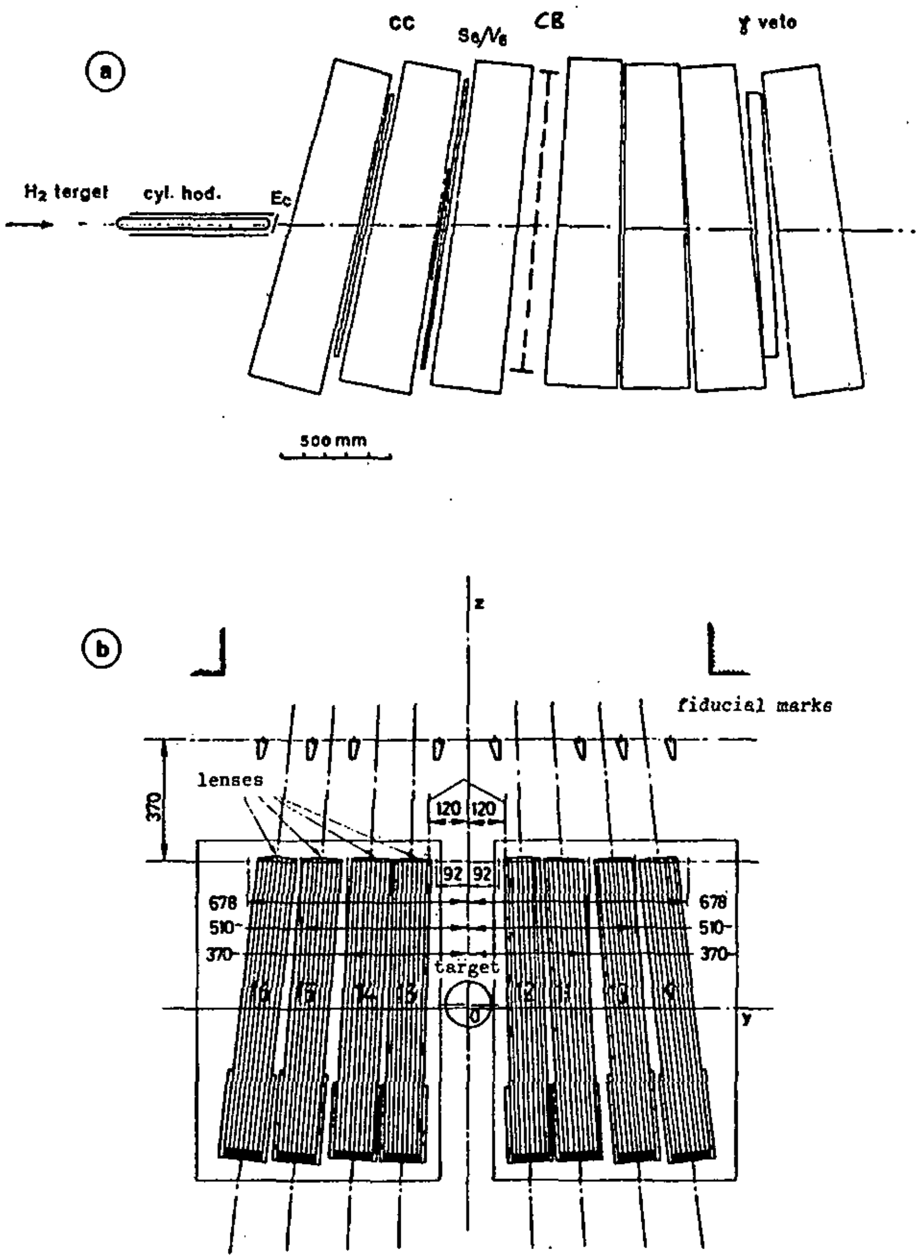

Fig. 2-4 : (a) Lateral view of Geometry I spark chambers.
(b) Front view of Geometry II spark chambers.

other hand, the maximum number of events/burst which can be recorded is limited by :

1. beam intensity, which, in turn, had to be adapted to the memory time of spark chambers of about 1.5 μsec (possible multi-event recordings),

2. read-out time of spark chamber information of about 25 msec per event.

The liquid hydrogen target (diameter 4 cm, length 65 cm) was surrounded by several scintillators which were part of the trigger system :

- end cap EC : which vetoed charged particles in the forward direction,
- barrel counter BC : a set of 24 scintillator slabs parallel to the target for multiplicity trigger information,
- cylindrical scintillator CYL : which vetoed outgoing charged particles for 2V0 events.

Sandwiched in between the spark chamber modules more scintillators and multiwire proportional chambers (MWPC) were installed (see fig. 2-3 (b)):

- two sets of MWPC's, one at the exit of the target, the other one in the center of Ω, the "chambre à Beusch" CB,
- 6 scintillator slabs S6 : each about 30 cm large, which were used to assure the up-down symmetry of events,
- a special proportional chamber CC : consisting of 57 radial sensitive sectors. This chamber will be described more precisely in the next subsection.

Although we recorded the drift chamber information during a certain period of WA13, we did not exploit it for analysis since typical events at large angles had outgoing tracks which normally left the Ω spectrometer before they reached the drift chambers, this was the case in particular for 2V0 triggers. In addition a γ-veto (consisting of a thin lead sheet and plastic scintillator sandwich arrangement) was installed after the 6th spark chamber module where many tracks underwent secondary interaction.

A copper plate-plastic scintillator sandwich device of limited acceptance behind Ω was used as $\bar{n}$-veto, in order to reduce final state configuration like $K^0\Lambda\bar{n}$ after p-$\bar{p}$ interaction.

The incoming beam was defined in its position (Y,Z) at X = - 175 cm and angles λ,ϕ by three MWPC B1, B2, and B3 constituting 7 planes of parallel wires with a 1 mm wire spacing.

2.3.2 Electronics Trigger

The whole set of particle detectors described above can now be regrouped and combined in order to build the final trigger signal.

In other words, upon consideration of coincidence, anti-coincidence, and correct timing of all detector signals, a decision is taken whether to fire the spark chambers and record the event on the data acquisition computer or to reset all signals and drop the information accumulated so far.

The principle is, upon arrival of a beam particle inside Ω, to build up the trigger step by step by adding up information which is available at a certain moment. Different parts of the detector system may need different time intervals (ranging from about 10 to 400 nsec) to digest their information. Thus different trigger levels are reached as is summarized in the schematic diagram of fig. 2-5 :

. AT1 trigger level : which is set if a beam particle has undergone interaction inside the target,
. ILT trigger level (intermediate trigger) : which indicates that further counters (like BC,S6) suspect an acceptable event,
. UFT trigger level (user fast trigger) : final trigger which is reached upon beam identification and after decision from the logic of the coplanarity chamber.

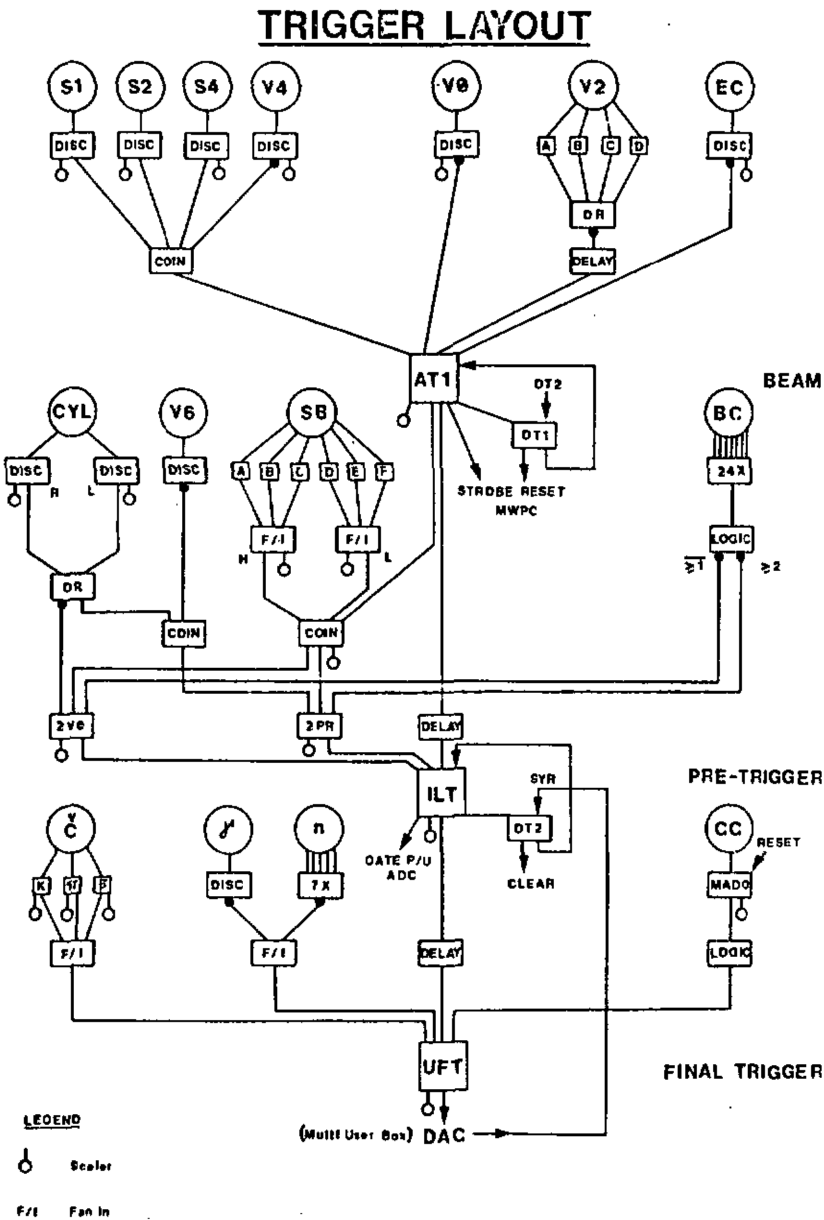

Fig. 2-5 : WA13 electronics trigger.

For WA13, two types of events were looked for :

1. two-prong events, i.e. two body final states and
2. two-body reactions with 2 V0's, i.e. 4 outgoing charged particles in the final state.

So we had in summary the following two electronic triggers :

$$\text{"2-prong"} = \mathrm{BEAM} \cdot \overline{\mathrm{EC}} \cdot (\mathrm{BC} = 2) \cdot \text{CC-logic} \cdot \mathrm{S6} \cdot \overline{\mathrm{V6}} \cdot \overline{\mathrm{n}} \cdot \overline{\gamma}$$

$$\text{"2-V0"} = \mathrm{BEAM} \cdot \overline{\mathrm{EC}} \cdot \overline{\mathrm{BC}} \cdot \overline{\mathrm{CYL}} \cdot \text{CC-logic} \cdot \mathrm{S6} \cdot \overline{\mathrm{n}} \cdot \overline{\gamma}$$

The arrival of a beam particle was defined by $\mathrm{BEAM} = \mathrm{S1} \cdot \mathrm{S2} \cdot \mathrm{S4} \cdot \overline{\mathrm{V4}}$, i.e. a coincidence (and anti-coincidence) of signals from scintillators installed in the beam line before entry into the Ω spectrometer.

A specialty in WA13 was the use of a proportional chamber (CC) with nearly radial symmetry which assured the coplanarity of wanted events. (Construction and tests of this chamber was one of the contributions of our colleagues at the Collège de France in Paris.) Its associated electronics supplied a positive decision signal if two opposite sectors (including one or two additional nearest neighbours in some configurations) were hit by charged particles. The list of all possible configurations of hit sectors, modulo a rotation of $2\pi/57$ and $2\pi/19$ for 2-prong and 2-V0 triggers respectively, is summarized in the following reference table :

2CH/2V0	Ser. Nr.	1st	2nd	3rd	4th	Times
1	1	1	29	0	0	57
1	2	1	29	30	0	57
1	3	1	28	0	0	57
1	4	1	28	29	0	57
1	5	1	30	31	0	57
3	1	3	30	33	0	19
3	2	3	6	30	0	19
3	3	3	6	36	0	19
3	4	3	6	30	33	19
3	5	6	33	0	0	18
3	6	3	9	33	0	19
3	7	3	9	36	0	19
3	8	3	9	33	36	19

Table 2-2 : Reference table of coplanarity chamber.

The first column labels the trigger type (1 for 2-prong, 3 for 2-V0), the second one gives the number of the series for a given type, the next four columns contain the possible hits, and the last one states how often this reference configuration could occur. For the 2-V0 trigger, 3 sectors each were regrouped into one logical sector.

A typical configuration of a 2-V0 event is sketched in fig. 2-6 (a).

Possible cross talk between neighbouring sectors was partially included in the choice of the above configurations. Fig. 2-6 (b) gives an idea of the extent of cross-talk.

The decision logic electronics was operated according to a timesaving look-up procedure based on "hash coding" (or scatter storage technique, see ref. [BEL77]) which was designed by F. Bourgeois et al. at CERN : instead of comparing the actual configuration, say C, with all possible configurations stored in a look-up table T (a maximum time of 6 μsec might have been necessary to do this !) the result, say R, of a simple algorithm executed upon C was used in order to read the contents C_r at the address R in a specially arranged memorized table T_r. If the configuration C was equal to the reference C_r, the event was a good candidate. If $C_r = 0$, the event had to be rejected.

Conflicts were possible when the algorithm led to the same result R for two configurations C_1 and C_2. In this case, the table T_r contained at the location R, the address of the second possible configuration C_2. Depending on the cleverness of the choice of an appropriate algorithm, the size of T_r can be much smaller than the one of table T.

With the aid of this technique, the maximum decision time of the coplanarity logic could be brought down to about 200 nsec.

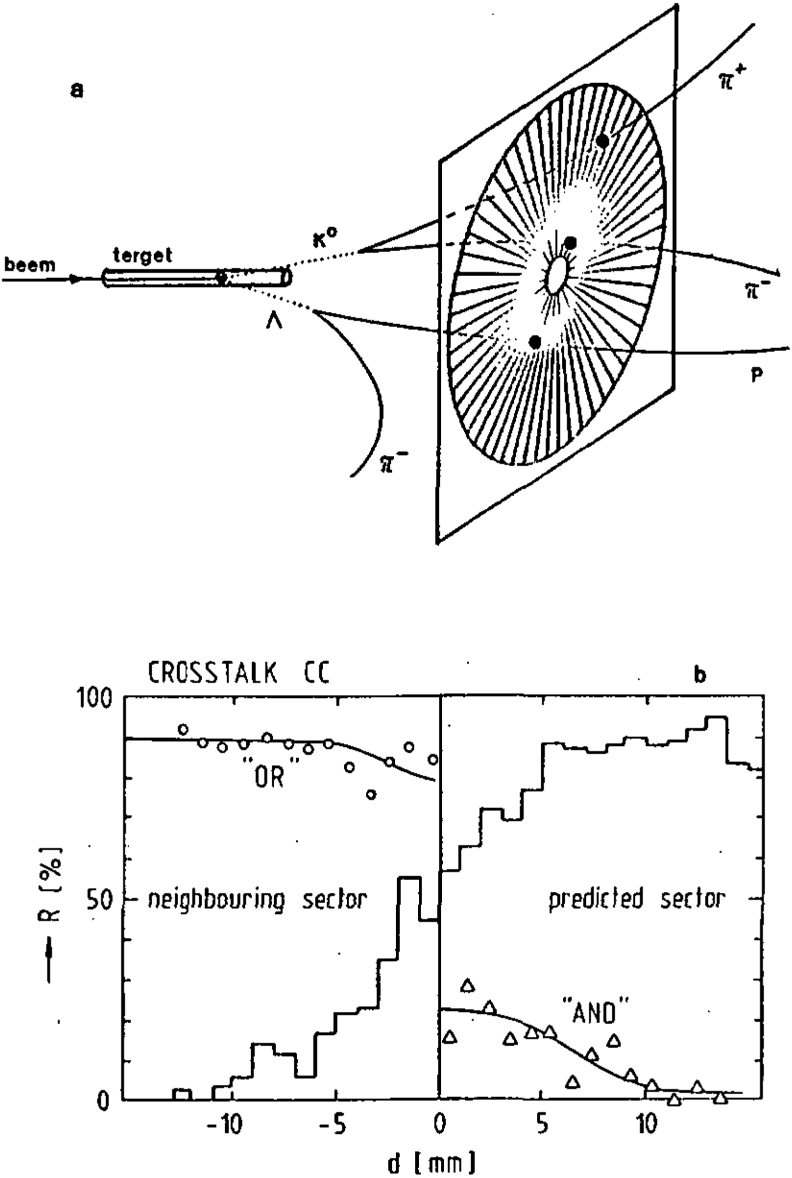

Fig. 2-6 : *(a) Typical topology of an event $\pi^- p \to K^0 \Lambda$ with 3 hits in the coplanarity chamber CC.*

(b) Crosstalk between sectors of the CC. d is the distance between the particle impact and the nearest edge of the sector.

2.4 Data Acquisition System

If an event occured in the Ω spectrometer and the electronics trigger accepted it, a fast signal (UFT) was sent to the data acquisition computer (DAC) in order to tell it to start its main job, that is to read all event information from the CAMAC crates and write it on to the raw data tape.

In principle, several users could send trigger signals to the DAC. During WA13, however, only one further experiment was running with lower priority at the same time. Each user had his own small computer (PDP 11) for data monitoring and eventual electronics control, its own set of counters, and its NIM electronics, i.e. mainly ADC's (analog-to-digital converter), scalers, and PU's (pattern units containing simple 1-0 information).

A physical event which the DAC had to digest consisted of different types of data (fiducial events containing fiducial mark recording were simpler) :

. beam counters,
. spark chambers,
. MWPC's (CS,..)
. user defined data (ADC's, PU's,..)

In general, all information coming from the spectrometer was transformed into NIM standard signals (0 and - 800 mV into 50 Ohm, negative logic), and collected and structured in CAMAC crates which were read via CAMAC links into the DAC computer (PDP 11/40). The hardware structure, i.e. the arrangement of the CAMAC crates and their subdivision into branches (which may contain certain data or which may themselves lead to further crates) gave rise to a special event structure called ROMULUS. This structure supplied the event data with block numbers, pointers, and word counts. Thus during off-line analysis data stored in a certain block could easily be extracted from the event by a corresponding forward-backward reading scheme.

All components of the data acquisition system communicated with one another by sending signals indicating that they were "busy" (and could not receive any orders for the moment) or that they were "ready" to accept another task. An idea of how the system was composed is given in fig. 2-7.

The following important signals had to be handled :

USR : "user ready" : a user is normally "ready", and he declares himself "not ready" to the system at the moment he sends a UFT trigger. He then remains "not ready" until he has re-initialized his own electronics (NIM, CAMAC and associated user computer PDP-11).

SYR : the system is "ready" when the DAC computer and the plumbicon system are "ready", and when a beam signal is present.

The arrival of signals and the definition of resulting logic signals was handled in the MULTIUSERBOX (which controlled multiplexing of data arriving from different authorized users) and in THEBIGBOX which coordinated camera operation, plumbicon read-out, and DAC interrupt control, i.e. it defined the system ready signal SYR.

The operation of the whole system can be described in short like this :

1. When the system is ready an authorized user may send a fast trigger (UFT, - 800 mV/50 Ohm during 10 ns). This will make the system "busy".

2. The spark chambers are fired and the plumbicon information is collected. This takes about 16-20 ms. All event data is stored into a buffer.

3. The system becomes "ready" (SYR) again when (a) all users are ready again, (b) the DAC computer has finished its working cycle, and (c) the plumbicon system is ready.

The SYR signal is sent to the user (as indicated on fig. 2-5 in the lower right corner), informing him that the next event can be taken and stored into the buffer.

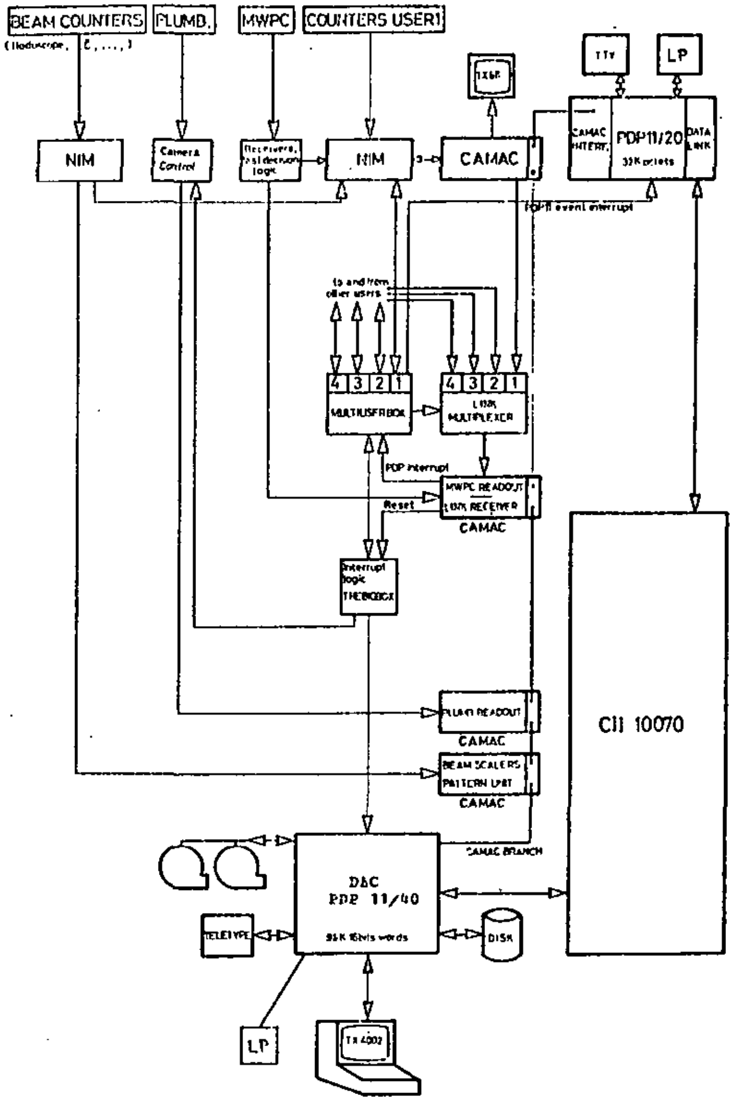

Fig. 2-7 : Multiuser data acquisition system.

Since writing an event on tape took more time than reading it from the CAMAC crates (e.g. to write a 1500 word event needed $\sim$ 45 msec); the maximal number of events recorded per beam burst was about 35 events/burst.

A number of programs were run on-line on the user computers to accumulate histograms of different counters, ADC's or PU's, in order to detect possible failures as soon as possible. One of the programs could visualize the data of the plumbicons and some of the trigger information event by event. A typical(*) example of a 2-V0 candidate is given in fig. 2-8.

As soon as the first raw data tapes were completed, checking programs were run on the CII computer (see fig. 2-7) for control of overall performance of the experiment.

The total number of triggers recorded during the experiment and $\pi^-/\bar{p}$ ratio of the S1 beam at different beam moments is given in table 2-3.

ORGANIZATION OF THE OFF-LINE ANALYSIS

The off-line analysis, as described in the next chapter, was done outside CERN, namely for 2-prong triggers, mostly in Paris, and for the 2-V0 triggers, mainly in Neuchâtel. Since the off-line programs (ROMEO) were too large to fit into the small computers (PDP-11 and VAX) available in Neuchâtel itself, we were grateful to be welcomed on the CYBER 7328 of the Ecole Polytechnique Fédérale at Lausanne which could

----

(*)To be honest, this is an exceptionally beautiful example without any additional accidental beams, old tracks from previous events, spark parasites, module failures, secondary particle interactions, track losses between modules, and what not; all features that characterized most of the 2-V0 triggers and made their off-line analysis somehow tedious and lengthy...

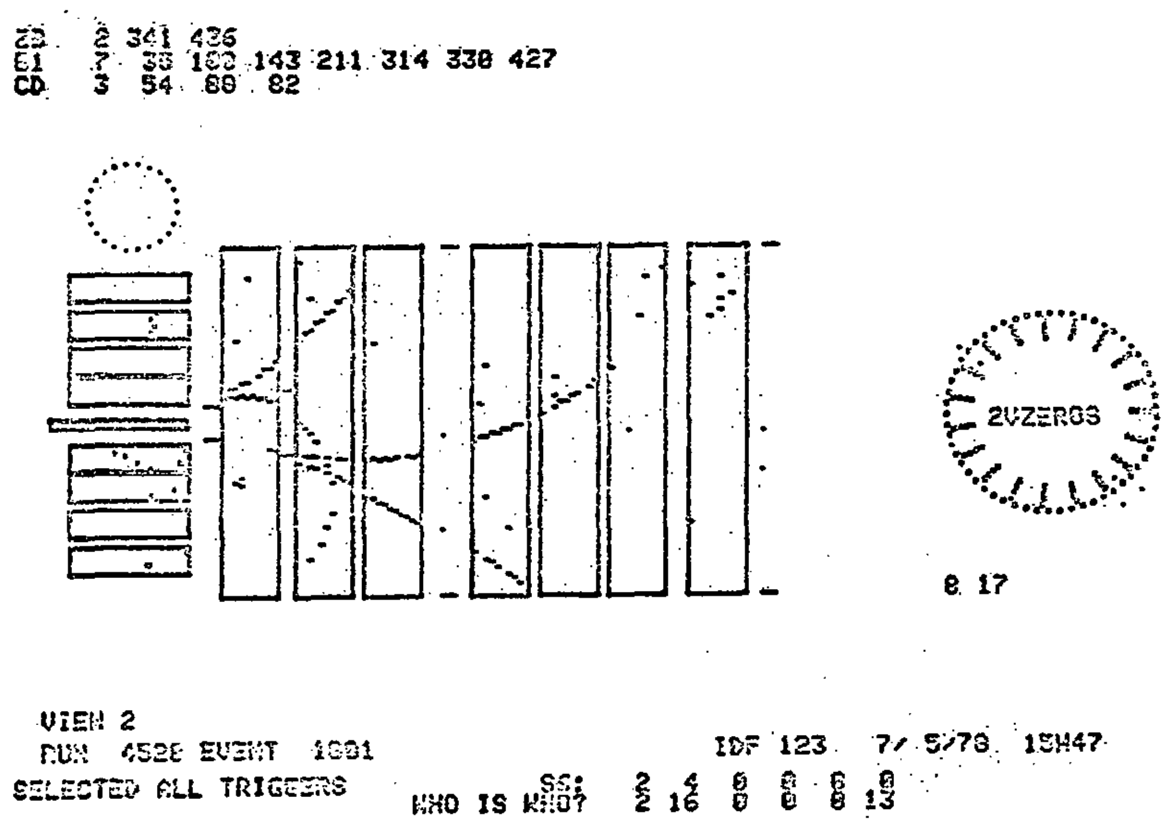

Fig. 2-8 : *Event configuration as visualized during on-line control.*

communicate with an underground remote input/output UT200 station in the Institut de Physique de l'Université at Neuchâtel, using a PTT line at 4800 baud.

p_{lab} [GeV/c]	# triggers all	2-V0	beam π^- : $\bar{p}$
3.0	32 600	4 600	4 : 1
3.1	54 800	8 800	
3.2	79 200	9 200	
3.3	35 200	3 700	
4.95	47 700	5 200	45 : 1
7.8	365 000	35 000	3 : 4
11.7	465 000	85 000	5 : 6
total	1 079 500	151 500	

Table 2-3 : WA13 events on raw data tapes.

3. EVENT RECONSTRUCTION

3. E V E N T   R E C O N S T R U C T I O N

In this chapter, we shall follow eventa from raw data tapes written during the run of WA13 along their off-line analysis.

For the reconstruction of charged tracka and the fit of their parameters, i.e. inverse momentum 1/P and angles λ, ϕ and the search for V0-candidates, the ROMEO program (Reconatruction of OMega Events Off-line) was used mainly. Special versions are needed for calibration purposes like :

. alignment of spark chamber modules

. calibration of beam momentum.

We will look in some detail into error treatment for the above mentioned parameters : spark fluctuations, measurement errors, and multiple Coulomb scattering errors will be important.

Finally, the procedures, used either within ROMEO or in separate programs, for the determination and fit of V0's of neutral particles and of the main vertex inside the target will be discussed.

3.1 ROMEO Pattern Recognition

Details about the structure of ROMEO can be found in [ROM75].

We shall limit ourselves here to the description of the most important steps and of routines special to WA13.

The main task of the pattern recognition module ia to try to recognize track segments from the sparks recorded for the two stereoscopic views. This comprises :

. fiducial mark interpolation

. spark decoding

- track following
- track matching
- elimination of accidental beams
- extra track finding.

3.1.1 Fiducial Marks

The fiducial mark system consists of 12 bars with 11 flash tubes each for the Geometry 1 region and of 8 bars with 5 flash tubes in Geometry II, as shown in fig. 3-1. The bars which are mounted at $z = 81.65$ cm, just above the spark chambers, are fired between two bursts of the SPS and recorded by the plumbicon system in the same manner as ordinary events.

If the camera positions and the fiducial bar coordinates are known exactly, ROMEO can determine the position of a spark in the $z = 0$ plane.

Let Y_{ij} be the coordinate of the ith fiducial mark belonging to the jth bar, furthermore, let M_{ij} be a mean measured value of the fiducial mark position, as detected by the plumbicons. Then ROMEO calculates correction coefficients $A_n, n = 0..5$, for Geometry I and $B_k, k = 0..3$, for Geometry II by adjusting a polynomial of order 5 and 3 respectively on the measured coordinates :

$$Y_{ij} = \sum_n A_n M_{ij}^n \quad \text{(Geometry I)} \tag{3-1}$$

$$Y_{ij} = \sum_k B_k M_{ij}^k \quad \text{(Geometry II)}$$

These two equations resolve two problems at a time :

1. the transformation from the plumbicon coordinate system (measurement (M_{ij})) to the XY-plane coordinates (Y_{ij}) and
2. the correction of distortions in the plumbicons and their associated electronics. In fact, as all fiducial marks on one bar are perfectly aligned in a straight line, all coefficients in eq. (3-1) except A_0, A_1 and B_0, B_1 should vanish.

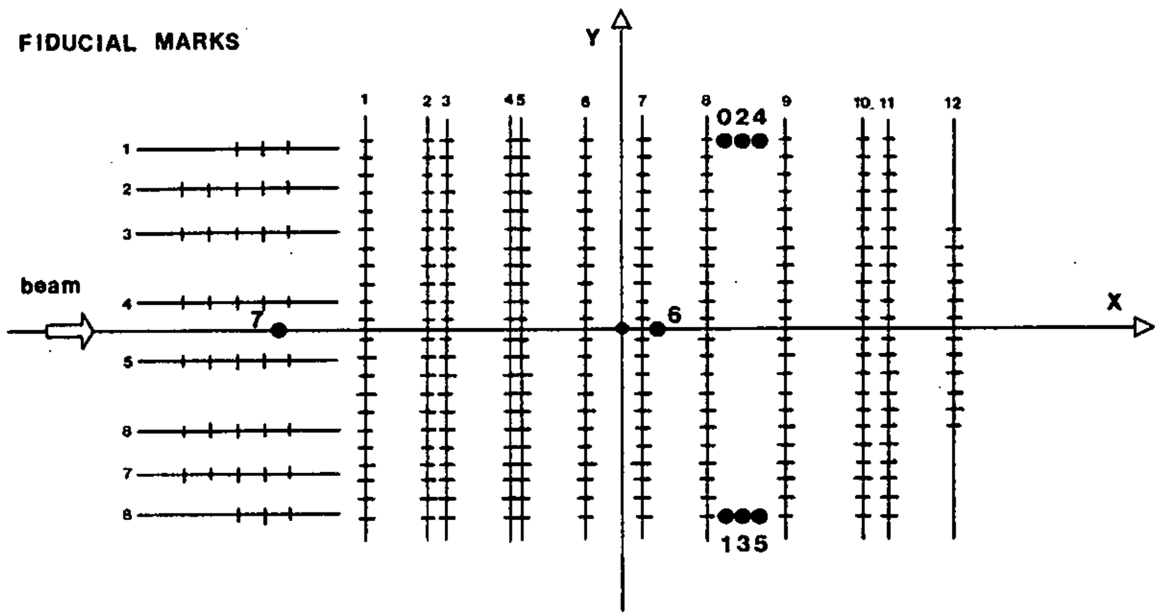

Fig. 3-1 : *Fiducial mark system of Ω. Projected positions of cameras are marked 0-2-4-6 for view 1, and 1-3-5-7 for view 2.*

If the coordinates of a spark inside an optical module have to be determined, a linear interpolation between the coefficients of adjacent bars is used to calculate the correction coefficients for this individual spark. Therefore, it is no surprise that these operations, though very simple, require a considerable part of the CPU time of an event.

3.1.2 Track Finding

From the procedure described above, to each spark two pairs of coordinates (X,Y_1) and (X,Y_2) are assigned for view 1 and view 2 respectively, the X-value being known from the gap number in which the spark was detected. Each gap is viewed by two cameras in order to obtain a stereoscopic view of the sparks. The correspondence of view M to camera N is given in the following table (see also fig. 3-1) :

Camera N		View M
0 - 2 - 4	6	1
1 - 3 - 5	7	2
Geometry I	II	

Now ROMEO has to attack the difficult task of deciding which subset of sparks may constitute a physical track. An especially timesaving procedure was developed at CERN by F. Bourgeois et al. [BOU70]. So-called track segments are established separately for the two views. The search is *done in odd (or even) numbered gaps alone for a start. Thus, staggering* effects can be treated later.

Controlled by the steering routine FTRACK, tracks are followed from the last module in Geometry I towards the target and from the innermost modules in Geometry II away from the target (cf. fig. 2-3). Starting trials look for 3 consecutive successful associations in order to open a new track bank or, in the case of 2 consecutive failed associations, to give up the attempt. A set of sparks can be considered as a track segment if there are 3 sparks, and the distance between any two consecutive sparks is not greater than two (double) gaps. In addition, an upper limit on the angle of a straight line between two sparks and the normal to the spark chamber gaps has to be respected.

The criteria to accept or reject the association of further sparks depends on the predictions and tolerances calculated by the fit of a curve on the set of the last found sparks : 4 last for a circle, 3 last for a parabola, 2 last for a straight line.

When the last gap is reached, the track segments are followed backwards (subroutine BACK), i.e. from the segment tail towards the head established above. This process allows the program to recover sparks which could not be associated to a segment during the starting trials.

This search is done in both views.

Next the segments found are used to search systematically for sparks in gaps with the complementary parity. As will be explained in more detail in the next subsection, the "staggering", i.e. the displacement of a spark in a gap of given parity with respect to the neighbouring sparks in gaps with different parity, can be computed as :

$$\Delta Y_{st} = \sigma_0 + \sigma_1 \tan\alpha \tag{3-2}$$

where σ_0 and σ_1 are constants and $\tan\alpha$ is the slope of the track. Hence, the positions of sparks can be predicted and the sparks are searched for. This process is called the track complementation and is done in the routine TRCOMP.

After elimination of accidental beam tracks in the routine ACBEAM on the basis of momentum estimates and track positions the track segments found in the two views separately must be matched in order to know which ones are the projection of a track in space.

Finally, some non-matched segments or isolated sparks may be left over which could belong to tracks that are strongly curved or which were lost while "bridging" between Geometry I and II. The routines XTFIND and XTLINK assure this job of extra track finding.

All track coordinates written on to the output record are given in the $z = 0$ projection of the Omega coordinate system without any correction for staggering so far.

3.1.3 Staggering Corrections

A clearing field (of the order of some 100 V) is applied to the spark chamber gaps in such a way that its direction is opposite in neighbouring gaps. Hence the Lorentz force will lead to opposite spark displacements during the time interval between the passage of an ionising particle and the firing of the modules (high tension of 13 kV and 12 kV for Geometry I and II respectively). In fig. 3-2, examples of the staggering effect are illustrated for an "old" track, which might belong to the previous event, and for a "young" track, normally an accidental beam particle which traversed the detector during its memory time.

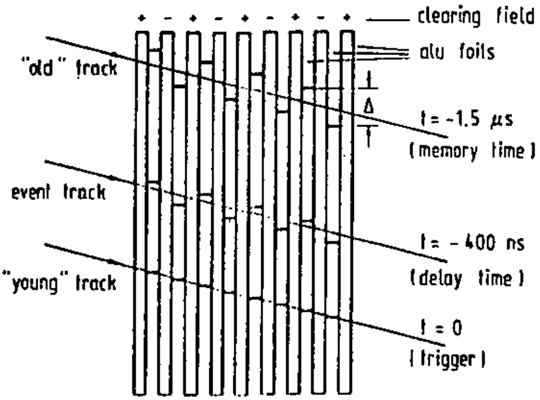

Fig. 3-2 : Staggering effect in spark chambers.

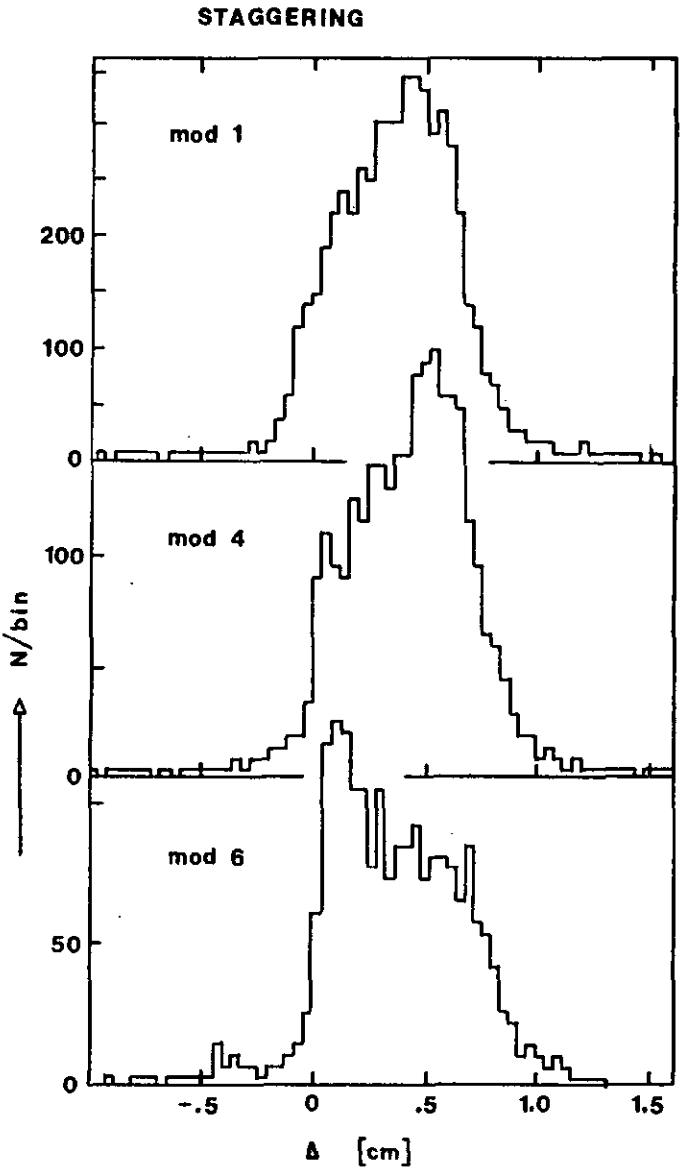

Fig. 3-3 : *Staggering in Geometry I modules. "Young" beam tracks produced the peak near zero.*

Since the negative field of the spectrometer magnet was changed for different beam momenta during the run of WA13, we had to determine different sets of parameters σ_0 and σ_1 for eq. (3-2). This is done by setting all staggering values to zero and calculating the difference $\Delta = Y_1 - Y_2 = 2 * \Delta Y_{st}$ of two consecutive sparks. An example of the distribution of Δ in spark chamber modules of Geometry I is given in fig. 3-3.

The contribution from "young" accidental beam tracks is clearly visible at $\Delta = 0.1$ cm. The following values are an example for the constants in the expression $\Delta Y_{st} = \sigma_0 + \sigma_1 \tan\alpha$ used at 4.95 GeV/c with 18 kG magnetic field :

	Geometry I	II	
σ_0	0.25	0.35	cm
σ_1	0.06	0.03	cm

3.2 Romeo Geometry

This part of ROMEO will establish the track parameters $(1/p, \lambda, \phi)$ and search for V0 candidates.

At this stage, not only the spark chamber information, i.e. the track segments found for both stereoscopic views in the pattern recognition part, but also the wire chamber data is exploited for the determination of the beam momentum and for the rejection of out-of-time tracks. As will be described in section 3.3, several experiment-dependent calibration constants are needed which can only be determined accurately once the geometry part has been executed using default values.

The flow chart in fig. 3-4 gives an idea of the structure of the ROMEO geometry part.

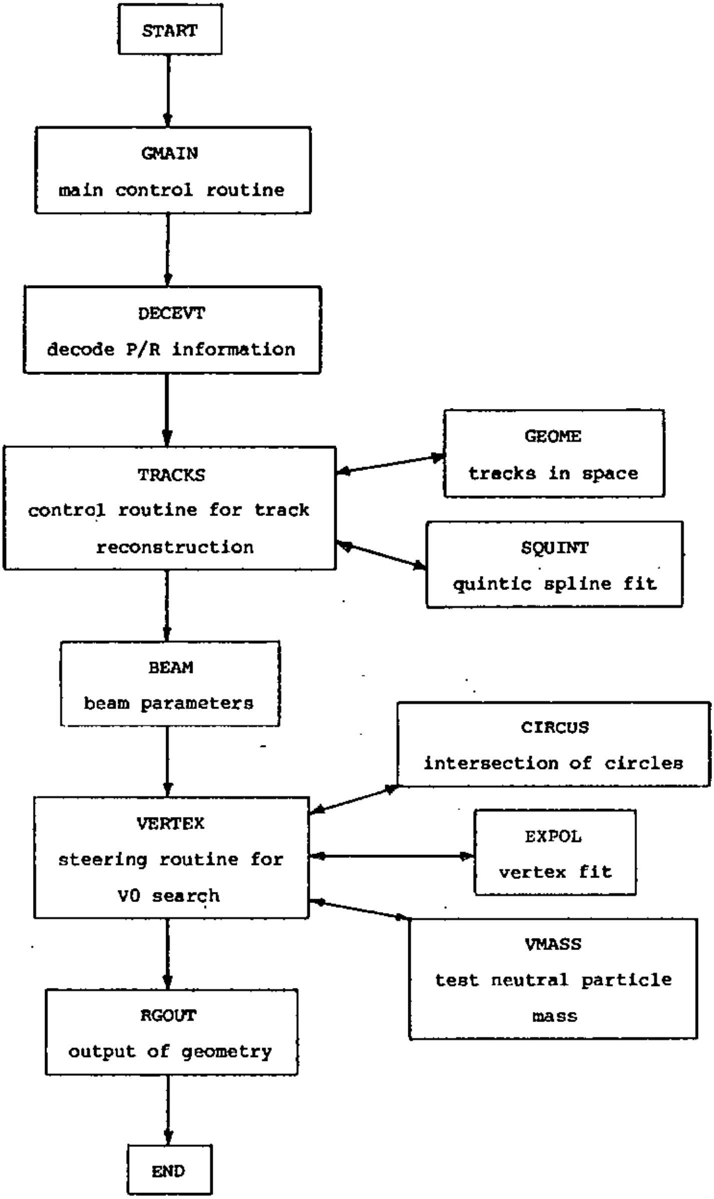

Fig. 3-4 : Flowchart of ROMEO Geometry.

Now let us look at some important steps in more detail.

A. SPACE POINTS

From pattern recognition one has obtained two coordinate pairs : (X,Y_1) and (X,Y_2) for the 2 views. In order to reconstruct the corresponding space point (x,y,z), one simply has to resolve the following set of linear equations representing the "light rays" (see fig. 3-5) :

$$\underline{\text{XZ projection}}: \quad X = X_{c1} + (x - X_{c1}) * r_z \qquad (3\text{-}3)$$

$$\text{with} \quad r_z = Z_c/(Z_c - z)$$

$$\underline{\text{YZ projection}}: \quad Y_1 = Y_{c1} + (y - Y_{c1}) * r_z$$

$$Y_2 = Y_{c2} + (y - Y_{c2}) * r_z$$

The position of the cameras is denoted (X_c, Y_c, Z_c).

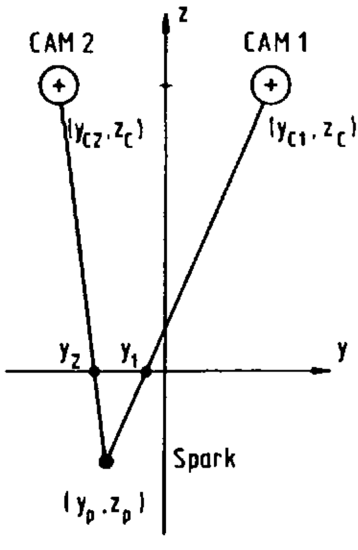

Fig. 3-5 : "Light rays" between spark and cameras.

A small correction term has to be introduced into eq. (3-3) in order to account for the glass plate installed on top of the spark chamber modules. All calculations are done in the subroutine GEOME.

B. Track Parameters

From all space points belonging to a track, one can now calculate in a first approximation the track parameters $(1/p_0, \lambda_0, \phi_0)$ at the first measured point (A,B,C). The momentum p_0 is calculated from the radius ρ_0 of a circle which can be adjusted on to the XY-projection of the track :

$$\rho_0 = p_0 * \cos\lambda_0/(.0003 * B_z) \qquad (3\text{-}4)$$

where λ_0 is the dip angle (p_0 in GeV/c, ρ_0 in cm, B in kGauss). λ_0 can be calculated by adjusting a straight line on to the ZX-projection :

$$z = C + x\tan\lambda_0' \quad \text{with } \tan\lambda_0 = \tan\lambda_0' \cos\phi_0 \qquad (3\text{-}5)$$

Finally, the polar angle ϕ_0 represents the tangent to the circle at the first measured point.

The parameters $(1/p_0, \lambda_0, \phi_0)$ are used as starting values in a quintic spline fit (routine FITPLF). As will be discussed in more detail in section 4.3 on error treatment in ROMEO, this fit leads to the final track parameters :

$$(1/p, \lambda, \phi, A, S).$$

3.3 Calibration For WA13

The Omega detector consists of different groups of chambers which are read for each event trigger :

. spark chambers of Geometry I

. spark chambers of Geometry II

. drift chambers (not used for WA13)

. MWPC inside Omega

. MWPC for beam.

During the calibration procedure, one has to find the accurate positions of all modules and wire chambers with respect to a given reference frame. For many Omega experiments, one uses the drift chambers installed at the downstream end of the detector as a reference, since their spatial resolution is extremely good (25 µm !). For WA13, many tracks leave the detector volume before reaching the drift chambers, so we used the optical chambers as reference and aligned the remaining detector accordingly (see ref. [SCH79]).

In order to adjust the spatial relative position of the spark chamber modules themselves, we have analysed tapes which contain recordings of straight wires.

3.3.1 Straight Wire Data

It has been found that, in spite of using fiducial mark information, ROMEO calculates points in space which may deviate slightly from the actual spark positions.

Our aim is to correct the Y and Z positions of each spark chamber gap independently for the Geometry I modules. This means finding the correction coefficients which have to be applied before a track fit is done in the geometry part of ROMEO. Straight wire data offers a solution to this problem.

There are 6 wires mounted in Omega just above the spark chamber modules of Geometry I. By varying a capacitance, the wires are illuminated with different intensities of light from flash tubes. Thus, the plumbicon system will detect all different spark intensities (0,1,2...7), and an event will be recorded where the straight wires are treated as normal tracks in the z = 0 plane.

On reconstruction of these events, ROMEO (in a special version) normally does not find exactly a straight line. A linear fit will then enable the determination of coefficients which account for two types of corrections :

. Slewing corrections : compensate the effect that the spark position (in Y), detected by the plumbicon system, depends on the spark intensity.

. Distortion corrections : compensate the deviation of the straight wire data from straight lines by correcting the Y-position of sparks for each Geometry I region (corresponding to a certain wire), for each view, and for each gap independently.

We have checked the influence of corrections from the straight wire data analysis for different magnetic field values by applying them to beam tracks at various energies. The result on a straight wire itself is illustrated for one example in fig. 3-6. The reconstructed wire has become "really straight" after applying full field slewing and distortion corrections.

It seems reasonable to suppose that during over two months of running time of WA13, drift effects in the plumbicon electronical (and mechanical) system should be taken into account. Unfortunately, this could not be verified since the straight wire data was only taken at the end of the experiment.

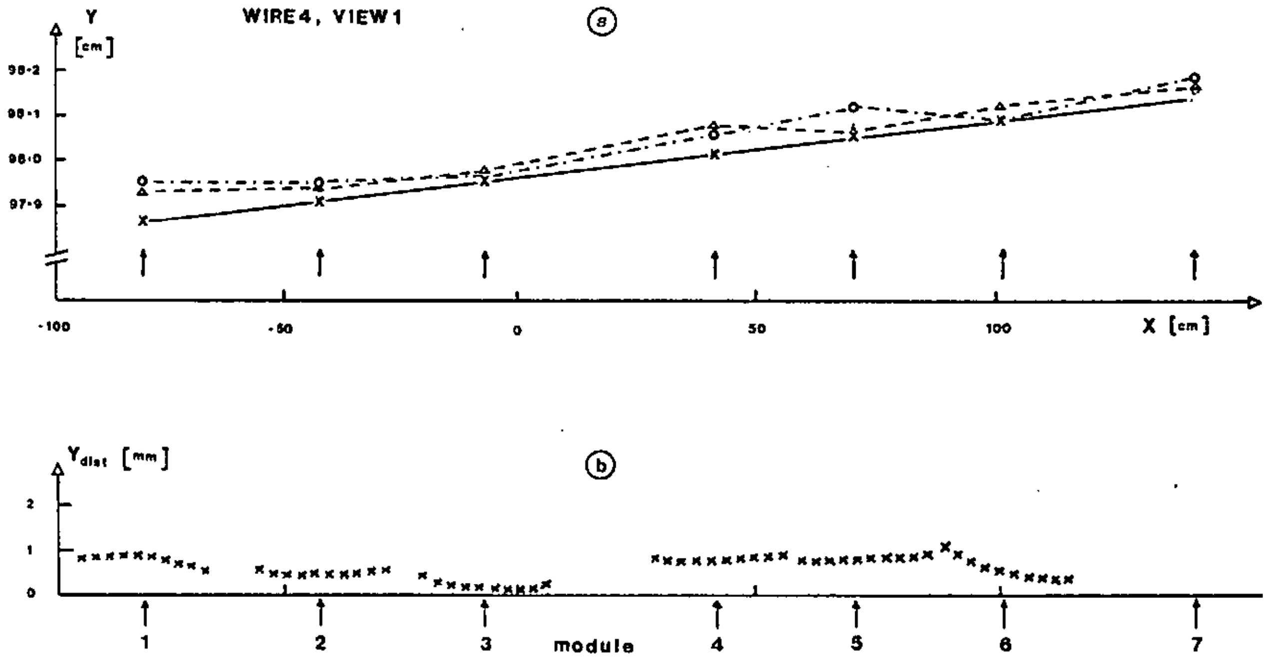

<u>Fig. 3-6</u> : (a) *Straight wire coordinates in Geometry I of (Δ) uncorrected data, (o) after applying slewing corrections, and (x) after slewing + distortion corrections.*

(b) Individual corrections for each gap.

3.3.2 Beam Calibration

Special runs were recorded at all beam momenta without requiring a positive electronic trigger signal at reduced beam intensity. Thus, a large number of beam tracks were produced in the spark chambers and recorded as beam track events.

This data enables a double calibration :

. calibration of beam momentum P_{lab}

. calibration of Y and Z positions of beam chambers B1-B3.

First, the beam momentum, as determined by ROMEO, was compared to the value of the EA spectrometer situated far upstream in the S1 beam line. It consists of a set of MWPC. Only for a certain number of events (abour 50 - 70%, according to beam momentum) could the value of P_{lab} be determined since one required non-ambiguous hits in at least 3 planes. The resulting distribution defined the default value for the remaining events.

Furthermore, by comparison of the P_{lab}-distribution from the EA spectrometer and the one obtained from ROMEO, we detected a slight displacement of the first spark chamber module of the Geometry I region in the X direction.

In order to calibrate the position (Y and Z) of the beam wire chambers at the entrance to Omega, a linear extrapolation of the beam tracks for $x < -175$ cm gave predictions of hits in these chambers.

Comparison to the actual hits found yielded the wanted calibration coefficients.

The influence of the magnet field outside Omega is small and was neglected in this extrapolation.

Using the calibration constants for the analysis of the real events, the two independent couples (Y,ϕ) and (Z,λ) characterizing the beam track at the entrance of the target were determined by a linear fit to the beam chamber information. One required in both the Y and Z direction at least two single hits. If double hits occured in one plane, the point nearest to the linear fit from the other single hits was used, and the fitting procesa was repeated including this new point.

Typical distributions for the beam momentum P_{lab} and the angles λ, ϕ are shown in fig. 3-7.

The FWHM value of the beam momentum distribution for $P_{lab} = 3.1$ GeV/c was :

$$\text{FWHM } (P_{lab}) = .104 \text{ GeV/c}$$

which corresponds to a momentum resolution of :

$$\Delta P/P \text{ (nom)} = 1.4\%$$

for nominal beam values. The resolution for measured beams (EA spectrometer) was much better :

$$\Delta P/P \text{ (meas)} = .2\%$$

The structure in the λ distribution in fig. 3-7 (b) reflects the wire spacing of 1 mm of the beam chambers. The angular precision is typically :

$$\Delta\lambda \approx \Delta\phi \approx .6 \text{ mrad.}$$

Considering the distance between the first beam chamber and the center of the target, this corresponds to a possible maximal beam displacement of $\Delta Y \approx \Delta Z \approx 1.5$ mm.

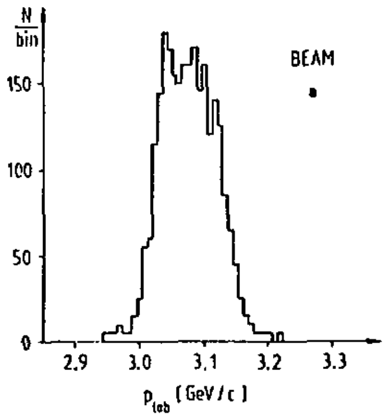

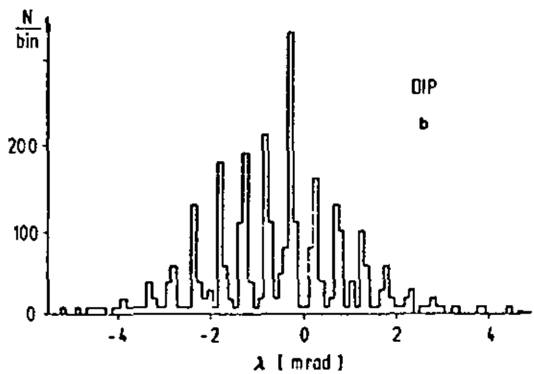

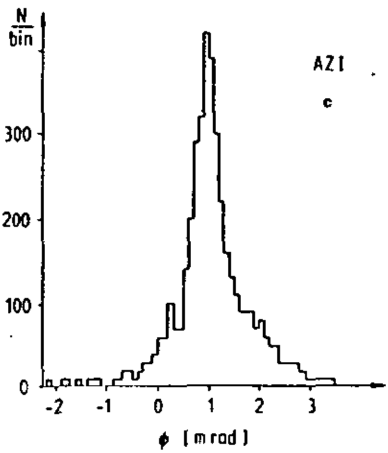

Fig. 3-7 :

Beam parameters at 3.1 GeV/c
(a) momentum $\bar{p}$ = (3.08 ± .04) GeV/c
(b) dip angle λ, peaks show the wire spacing of 1 mm
(c) azimuth angle φ at x = - 175 cm.

3.3.3 Alignment of Geometry II

A crucial region of the Omega spectrometer for the detection of 2V0 event triggers is the Geometry II spark chamber modules. Consider, for example, a $K^0\Lambda$ or an $\bar{\Lambda}\Lambda$ final state, where the relatively slow Λ particle will disintegrate into even slower charged particles which have a good chance of travelling, at least partially, through this region. The importance of these modules is underlined by the fact that without the Geometry II information we would have lost as much as 65% of the 2V0 candidates at 3.1 GeV/c.

We have checked the positions in the Y and Z directions (measured in the Omega coordinate system) by first reconstructing tracks in Geometry I modules alone, then extrapolating them into the Geometry II region, and finally comparing the spark coordinate predictions with those actually found. It was quite a surprise to realize that each of the 8 modules had to be shifted individually in the positive Z direction by roughly 3.6 mm.

The Y positions of the modules, as indicated by the survey measurements of Omega, proved to be correct.

The corrections introduced into ROMEO were checked by looking at the track residuals R_y and R_z after the quintic spline fit (where $R_y = Y_{spark} - Y_{fit}$ and $R_z = Z_{spark} - Z_{fit}$). From fig. 3-8 one can see that the resulting distributions are well centered.

As an additional result, we can deduce from fig. 3-8 the spatial resolution of the reconstruction of tracks in ROMEO :

	Geometry I	II	
σ_y	.3	.5	mm
σ_z	1.2	2.2	mm

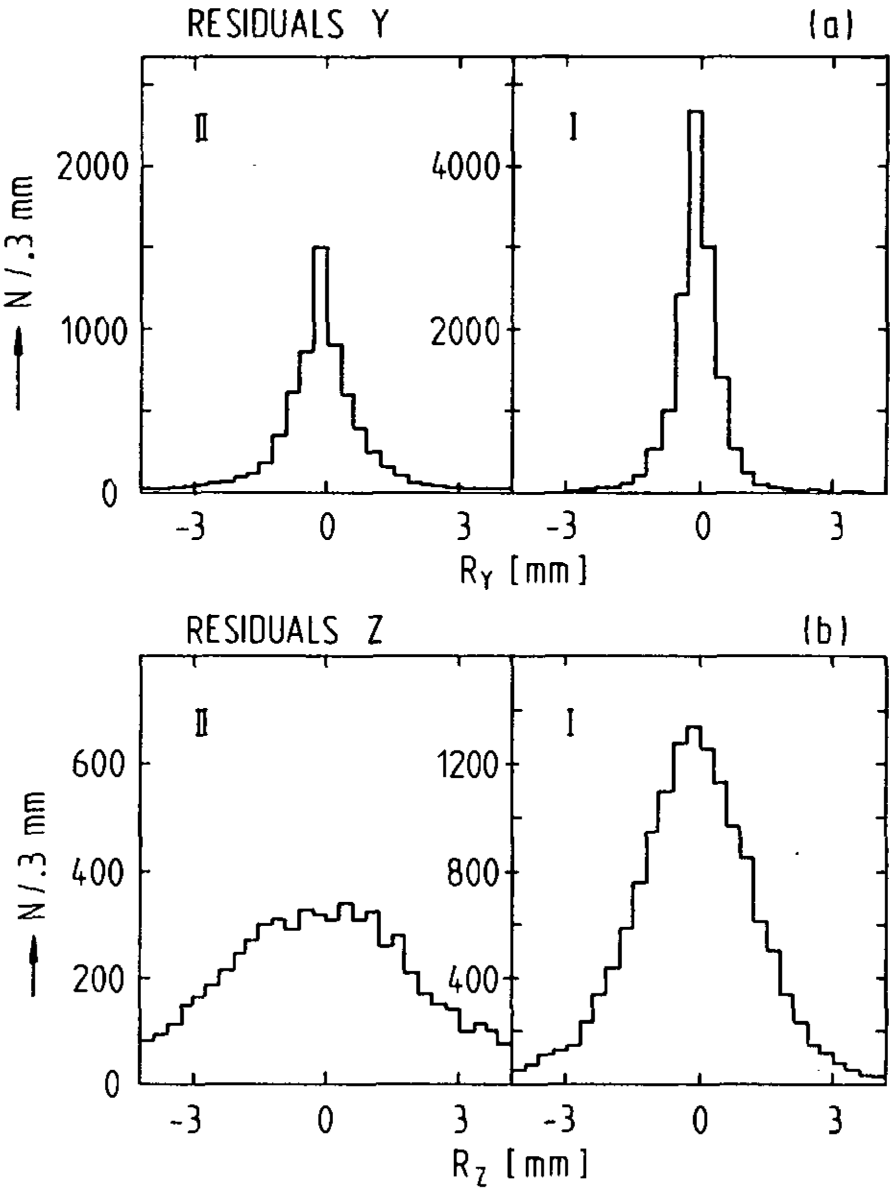

Fig. 3-8 : *Residuals after spline fit in (a) Y-direction and (b) Z-direction for Geometry II and I modules. The widths of the distributions indicate the spatial resolutions of track measurements.*

3.4 Error Treatment in ROMEO

During pattern recognition in ROMEO a weight is assigned to each spark, according to an estimate of its fluctuation in the optical chambers and to the measurement error which characterizes the optical and electronical detection systems, i.e. the stereoscopic video cameras and their calibration by fiducial marks.

These errors will determine the precision of the track parameters (momentum p, angles ϕ and λ) calculated during execution of the geometry part of ROMEO.

3.4.1 Spark Errors

For each spark seen by the plumbicon system, two errors and their corresponding error matrices have to be considered [TOW76] :

. fluctuation errors σ_f

. measurement errors σ_m.

A. SPARK FLUCTUATION ERROR

The fluctuation error σ_f represents a displacement of the spark seen by the cameras from the actual position of the track. The approximation in ROMEO is to assume that the fluctuation introduces an error in the Y position of the space point (Y_p,Z_p). There is probably also a Z fluctuation, but this is neglected in this approximation as the main effect on the sparks of the crossed electric and magnetic fields is in the y-direction. Thus, the error matrix for the space point from fluctuation only is :

$$E_f(Y_p,Z_p) = \begin{pmatrix} \sigma_f^2 & 0 \\ 0 & 0 \end{pmatrix} \qquad (3\text{-}6)$$

The effect of the fluctuation on the measurements Y_1 and Y_2 (view 1 and view 2 respectively) is obtained by transforming $E_1 = E_f(Y_p,Z_p)$ to the error matrix $E_2 = E_f(Y_1,Y_2)$ using the general error transformation equation

$$E_2 = R\, E_1\, R^t \tag{3-7}$$

R is the derivative matrix (Jacobi) of the transformation TR of the variables $(Y_p,Z_p) \longrightarrow (Y_1,Y_2)$ at a given value X. R^t is the transpose of R :

$$R = \begin{pmatrix} \dfrac{dY_1}{dY_p} & \dfrac{dY_1}{dZ_p} \\ & \\ \dfrac{dY_2}{dY_p} & \dfrac{dY_2}{dZ_p} \end{pmatrix} \tag{3-8}$$

The transformation TR is given by the equation (3-3) of the light rays (see fig. 3-5) :

$$\begin{aligned} Y_1 &= Y_{c1} + (Y_p - Y_{c1}) * (Z_c/(Z_c - Z_p)) \\ Y_2 &= Y_{c2} + (Y_p - Y_{c2}) * (Z_c/(Z_c - Z_p)) \end{aligned} \tag{3-3}$$

where (Y_{c1},Z_c) and (Y_{c2},Z_c) are the positions of camera 1 and 2, respectively.

Applying eq. (3-7) the fluctuation error matrix, we get :

$$E_f(Y_1,Y_2) = \begin{pmatrix} S_f^2 & S_f^2 \\ S_f^2 & S_f^2 \end{pmatrix} \tag{3-9}$$

where $S_f = \sigma_f * (Z_c/(Z_c - Z_p))$.

It is here where correlation terms between the two views are introduced into the error matrix.

B. MEASUREMENT ERRORS

The measurement errors on Y_1 and Y_2 are σ_1 and σ_2, respectively. They are uncorrelated. The full error matrix $E(Y_1,Y_2)$ is the sum of fluctuation and measurement errors :

$$E(Y_1,Y_2) = \begin{pmatrix} \sigma_1^2 + s_f^2 & s_f^2 \\ s_f^2 & \sigma_2^2 + s_f^2 \end{pmatrix} \tag{3-10}$$

Using the inverse of transformation (3-3) (light rays), one can now calculate the error matrix $E(Y_p,Z_p)$ on the space points. The weights W_y, W_z, W_{yz} used in ROMEO are obtained by inversion of the error matrix :

$$W(Y_p,Z_p) = \begin{pmatrix} W_y & W_{yz} \\ W_{yz} & W_z \end{pmatrix} = E^{-1}(Y_p,Z_p) \tag{3-11}$$

C. ROMEO VALUES FOR SPARK ERRORS

The values for the input errors σ_1,σ_2 used in ROMEO are different for the three categories of tracks :

paired tracks :	FLAG =	1	$\sigma_i = .04/\sqrt{2}$ $i = 1,2$
unpaired tracks :		0	.04
un-matched tracks :		-1	.04 * (1. + 2.*STEP)

where STEP = interpolation distance for the missing spark.

The criteria for the classification of the tracks depends on the minimum number of paired points NMINPR (for paired tracks) and the minimum number of corresponding points NMINCR (for matched tracks).

For WA13, we have used the values :

NMINPR = NMINCR = 8

The fluctuation error σ_f has two parts : σ_a = angle independent and σ_b = dependent on the angle ϕ of the track w.r.t. the normal to the spark chamber gap :

$$\sigma_f^{2'} = \sigma_a^2 + \sigma_b^2 * \phi^4 \tag{3-12}$$

The values used in ROMEO are :

$$\sigma_a = .018 \text{ cm}$$
$$\sigma_b = .170 \text{ cm.}$$

From these values one can see that the angle-dependent contribution σ_b becomes relevant for tracks passing a spark chamber gap with an angle ϕ > .5 rad. Tracks of this type are e.g. those belonging to a slow π^- particle from a Λ-decay of a $K^0\Lambda$ final state, the Λ itself being already slow with respect to the K^0. This is one of the reasons why the reconstruction efficiency for Λ's is rather poor, as we shall see in section 4.

3.4.2 Track Errors After Spline Fit

A. ERRORS ON SPLINE FIT PARAMETERS

For each track, a quintic spline fit is done in the routine SPHINX in order to adjust the following parametrization of the track in the XY and XZ projections [WIN74] :

$$\begin{aligned} Y_i &= A_1 + A_2 * X_i + D * YY(X_i) \\ Z_i &= B_1 + B_2 * X_i + D * ZZ(X_i) \end{aligned} \tag{3-13}$$

where A_1, B_1 are the positions and A_2, B_2 are the directions of the track at $X_i = X_1$. $YY(X_i)$ and $ZZ(X_i)$ are double integrals of the field functions, finally D = ± .0002998 / P, the sign depending on the sign of the magnetic field. It is negative for WA13.

As a result of the spline fit, one obtains the 5×5 error matrix for the variables

$$(A_1 \; A_2 \; D \; B_1 \; B_2)$$

which is stored in the track bank of the ROMEO output.

B. TRANSFORMATION $(A_1, A_2, D, B_1, B_2) \longrightarrow (1/P, \lambda, \phi, Y, Z)$

A convenient way to characterize a track is to choose its kinematic variables at $x = X_1$ of the first measured point :

$$(1/p \; \lambda \; \phi \; Y \; Z)$$

The transformation between the two sets of variables mentioned above is the following :

$$\begin{aligned} 1/p &= -D/.0002998 \\ \lambda &= \arctan(B_2/\sqrt{1. + A_2^2}) \\ \phi &= \arctan(A_2) \\ Y &= A_1 + A_2 * X_1 \\ Z &= B_1 + B_2 * X_1 \end{aligned} \qquad (3\text{-}14)$$

The 3×3 error matrix on the reduced set of kinematic variables $(1/P, \lambda, \phi)$ is calculated by applying, once again, the general error transformation formula (3-7) with a 5×3 Jacobi matrix.

C. "EXTERNAL ERRORS"

Up to now, the track error matrix was established on the grounds of individual spark errors alone. An alternative approach can be chosen once the geometrical track parameters like curvature ρ (in the XY projection plane), dip angle λ, polar angle ϕ, number of points NPT, and track length L are known. A reasonable estimation of the spark measurement error σ can be taken from the previous chapter. The following error formulae are based on the error on the sagitta F (see fig. 3-9) which was determined empirically by Roberts [AST67] :

$$\Delta(F) = 3.5\ \sigma/\sqrt{NPT} \tag{3-15}$$

The errors on $1/\rho$, λ, and ϕ are the same as used in the GRIND program [GRI68] and read as follows :

$$\boxed{\begin{aligned} \Delta(1/\rho) &= 28\ \sigma/(\sqrt{NPT}\ L^2 \cos^2\lambda) \\ \Delta\lambda &= 21\ \sigma \cos\lambda/(L\ \sqrt{NPT}) \\ \Delta\phi &= \frac{L}{2} \cos\lambda * \Delta(1/\rho) \end{aligned}} \tag{3-16}$$

The last equation can be deduced from fig. 3-9 which shows the relation between $1/\rho$ and ϕ :

$$\phi \doteq \alpha - L \cos\lambda/(2\rho), \qquad L \ll \rho \tag{3-17}$$

In addition, eq. (3-17) yields the (negative) correlation term between the errors on $1/\rho$ and ϕ :

$$\boxed{\Delta(1/\rho,\phi) = -.5\ L \cos\lambda\ \Delta^2(1/\rho)} \tag{3-18}$$

whereas the other correlation terms $\Delta(1/\rho,\lambda)$ and $\Delta(\lambda,\phi)$ are vanishing.

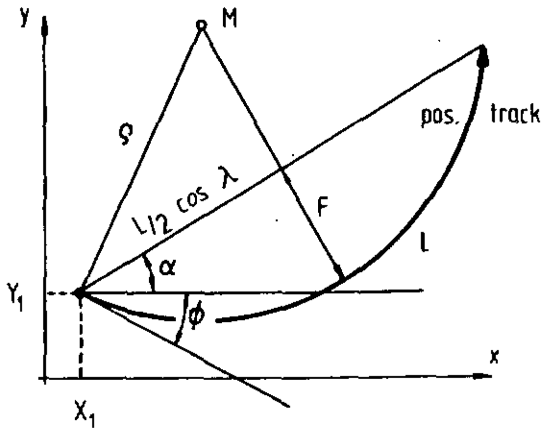

Fig. 3-9 : XY-projection of a track.

D. EXAMPLE OF NUMERICAL VALUES

The following table 3-1 compares the "external" errors from eq. (3-16) with the errors, as calculated in ROMEO for WA13 for a positive low momentum track and a negative medium momentum track from an event at 3.0 GeV/c beam : (EV 4402 906)

P	NPT		external errors	ROMEO errors	
.251 (GeV/c)	11	$\Delta(1/P)$	.0247	.0964	[1/GeV/c]
		$\Delta\lambda$	.0058	.0051	[rad]
		$\Delta\phi$	.0031	.0126	[rad]
		$\Delta(1/P,\lambda)$	-	-.98E-5	(≈ 2%)
		$\Delta(1/P,\phi)$	-.7E-4	-.12E-2	(≈ 98%)
-1.632 (GeV/c)	32	$\Delta(1/P)$	.0013	.0025	
		$\Delta\lambda$	.0008	.0004	
		$\Delta\phi$	.0005	.0006	
		$\Delta(1/P,\lambda)$	-	.34E-7	(≈ 1%)
		$\Delta(1/P,\phi)$	-.6E-6	.27E-6	(≈ 18%)

Table 3-1 : Track errors.

The comparison shows that occasionally the error formulas (3-16) underestimate the errors on the track parameters - if we assume that the ROMEO errors are reasonably well established. The correlation between $1/\rho$ and λ, which is neglected by the "external" errors, is in fact very small.

An illustration of a momentum error distribution w.r.t. the track length L is given in fig. 3-10. The beam momentum for this sample is 3 GeV/c, and the mean relative momentum error of the charged outgoing tracks is :

$$\Delta p/p \approx 1\%$$

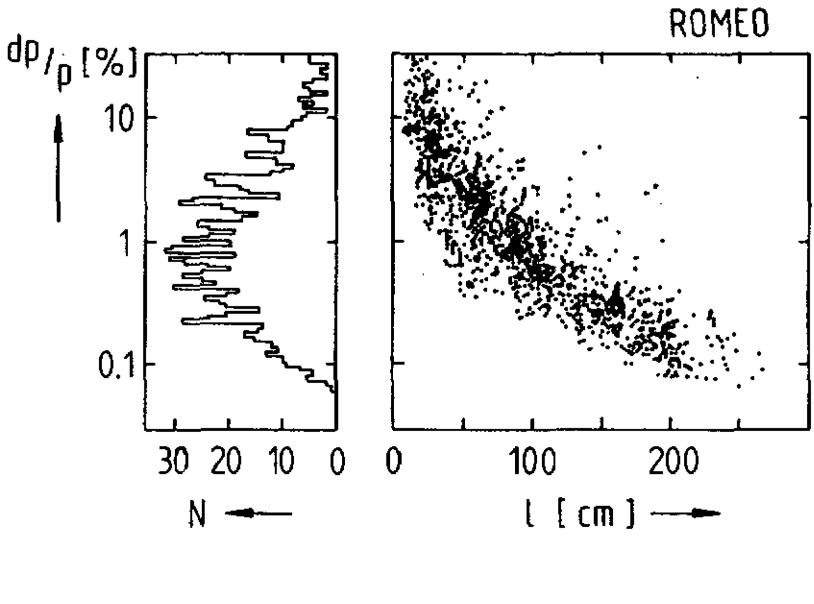

Fig. 3-10 : ROMEO error calculation on momentum p.

3.5 Multiple Scattering Errors

The charged particles from strange particle decays undergo multiple independent Coulomb scatterings while travelling through the detector volume. This is also true for the beam particle during its passage through liquid hydrogen inside the target.

Multiple scattering gives an additive contribution to the error matrix on the set of variables (A_1 A_2 D B_1 B_2) in the ROMEO output. The geometrical track parameters themselves are not changed.

A. MULTIPLE SCATTERING ANGLE

For small-angle scattering, the projected (plane) distribution is of Gaussian form [JAC62]. The dispersion of the plane angle (see fig. 3-11) is approximately [REV80] :

$$\Delta\theta = K * \sqrt{L/L_r} \qquad \text{with} \qquad K = .014/(P\beta) \qquad (3\text{-}19)$$

L/L_r is the thickness, in radiation lengths L_r, of the scattering medium. For WA13, this consists mainly of the spark chamber volume (L_r = 3500 cm), eventually the coplanarity chamber and S6/V6 (L_r = 40 cm). For the beam, the density of the liquid hydrogen is important : L_r = 890 cm.

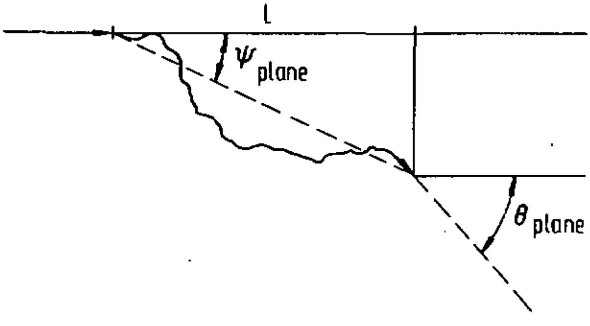

Fig. 3-11 : Multiple scattering angle.

For the evaluation of the multiple scattering errors w.r.t. the track parameters $(1/\rho, \lambda, \phi)$ we used the same formulae as derived in the analysis of the beam dump experiment at CERN [ROM80] :

$$\Delta^2(1/\rho) = \frac{4}{3} \frac{1}{(L \cos^2\lambda)^2} \Delta^2\theta \qquad (3\text{-}20)$$

$$\Delta^2\lambda = \frac{1}{3} * \Delta^2\theta$$

$$\Delta^2\phi = \frac{1}{6} \frac{1}{\cos^2\lambda} \Delta^2\theta$$

The correlation terms $\Delta(\lambda,\phi)$ and $\Delta(1/\rho,\lambda)$ can be neglected, whereas the relation between ϕ and $1/\rho$ was already illustrated in fig. 3-9 and analytically given in eq. (3-17).

This yields a (negative) covariance term :

$$\Delta(1/\rho,\phi) = -\frac{1}{3} * \frac{1}{L \cos^3\lambda} * \Delta^2\theta \qquad (3\text{-}21)$$

B. FULL ERROR MATRIX FOR (1/P,λ,φ,Y,Z)

First, the multiple scattering errors on $(1/\rho, \lambda, \phi)$ will be transformed into those for $(1/P, \lambda, \phi)$. Then, errors on Y and Z are discussed.

The transformation between the "geometrical" and the "kinematical" variables is given by (ρ in cm, B_Z in kG, P in GeV/c) :

$$\cos\lambda * p = \text{const} * B_Z * \rho \qquad (3\text{-}22)$$

We use it to calculate the derivative matrix (const = .0002998) :

$$D = \begin{pmatrix} \cos\lambda/(\text{const} * B_Z) & \frac{-\tan\lambda}{p} & 0 \\ 1/\tan\lambda & 1 & 0 \\ 0 & 0 & 1 \end{pmatrix}$$

One can see that for tracks with small dip angle λ and/or large momentum P, the correlation term between 1/P and λ should become negligible.

With the matrix transformation $E_{kin} = D\, E_{geom}\, D^t$ (cf. eq. (3-7)), we derive the new quantities :

$$\boxed{\begin{aligned}
\Delta^2(1/p) &= \cos^2\lambda/(\text{const} \cdot B_z)^2 \cdot \Delta^2(1/\rho) + \left|\frac{\tan\lambda}{p}\right|^2 \cdot \Delta^2\lambda \\
\Delta^2\lambda &= \frac{1}{3}\,\Delta^2\theta \\
\Delta^2\phi &= \frac{1}{6}\,\frac{1}{\cos^2\lambda}\,\Delta^2\theta \\
\Delta(1/p,\lambda) &= -\,\frac{\tan\lambda}{p} \cdot \Delta^2\lambda + \frac{\rho^2}{p^3\tan\lambda}\,\Delta^2(1/\rho) \\
\Delta(1/p,\phi) &= \frac{\cos\lambda}{\text{const} \cdot B_z}\,\Delta(1/\rho,\phi)
\end{aligned}} \qquad (3\text{-}23)$$

One should notice that the influence of variations ΔB_z of the vertical component of the magnetic field are sufficiently small, compared to the other errors, so they are dropped. As for the correlation between 1/P and λ, it can be seen from table 3-1 that it is in fact very small.

In addition, to be as correct as possible, one should regard how the multiple scattering errors, which increase along the track, influence the determination of the track parameters during the spline fit. Tracks which cross an important amount of material in between the spark chamber modules may even have been cut into two segments by the reconstruction program due to sufficiently large deviations in space. The track parameters in these cases could be improved by combining the track fits on the two separate segments.

Obviously the charged tracks have undergone some multiple Coulomb scattering already between the vertex of a V0 and the first measured space point.

Its amount will strongly depend on the distance x between those two points. In general, however, x is very small w.r.t. L_r.

Referring to the track parametrization used by Beusch [BEU81] the following variances and co-variances can be deduced :

$$\Delta^2 Y = K^2 \frac{x^3}{3L_r} \frac{1}{\cos^2\phi} \tag{3-24}$$

$$\Delta^2 Z = K^2 \frac{x^3}{3L_r} \frac{1}{\cos^2\lambda}$$

$$\Delta(Y,\phi) = K^2 \frac{x}{2L_r} \frac{1}{\cos\lambda}$$

$$\Delta(Z,\lambda) = K^2 \frac{x^2}{2L_r}$$

Again, correlations between "horizontal" and "vertical" variables vanish.

C. NUMERICAL VALUES

The following table 3-2 gives an idea about the order of magnitude of what was derived above. Two charged tracks, a π^+ and an $\bar{p}$ from an $\bar{\Lambda}$ decay are used as an example (cf. table 3-2 on next page).

The errors due to multiple scattering on $(1/p,\lambda,\phi)$ are surprisingly large w.r.t. the measurement errors, especially for the second track. This is because it is a rather long track which also passes through the scintillator S6/V6. The additional errors on Y and Z are negligible in both casea, as can be expected for secondary tracks from a V0.

In the scatter plot of fig. 3-12, the multiple scattering error on the momentum p of outgoing charged particles is shown w.r.t. the track length L for a sample at 3 GeV/c beam momentum. One can clearly distinguish the relatively small contribution from the spark chamber volume, followed by the influence of the coplanarity chamber, and finally the scintillator S6. In general, if compared to the fluctuation and measurement errors, multiple scattering errors are most important forlong tracks.

π^+ track			measurement errors	multiple scattering
nom. p	.251 GeV/c	$\Delta(1/p)$	.0964	.0017
flag	0	$\Delta\lambda$	.0051	.0053
NPT	11	$\Delta\phi$	.0126	.0037
L	80.5 cm	ΔY	.061	.006
L/L_Y	.027	ΔZ	.260	.006
		$\Delta(1/p,\lambda)$		-.14E-4
		$\Delta(1/p,\phi)$		-.54E-4
		$\Delta(Y,\phi)$	-.11E-3	.60E-5
		$\Delta(Z,\lambda)$	-.13E-2	.50E-5
$\bar{p}$-track			measurement errors	multiple scattering
nom. p	-1.632 GeV/c	$\Delta(1/p)$	.0025	.0055
flag	1	$\Delta\lambda$	.0004	.0022
NPT	32	$\Delta\phi$	.0006	.0016
L	258.7 cm	ΔY	.028	.001
L/L_Y	.200	ΔZ	.070	.001
		$\Delta(1/p,\lambda)$		.34E-7
		$\Delta(1/p,\phi)$		.27E-6
		$\Delta(Y,\phi)$	-.12E-4	.40E-7
		$\Delta(Z,\lambda)$	-.16E-5	.35E-7

Table 3-2 : Multiple scattering errors.

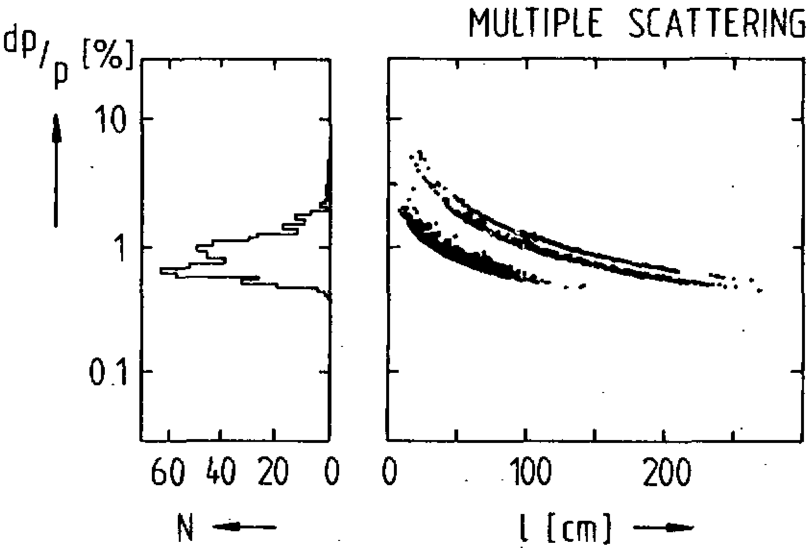

Fig. 3-12 : *Relative error on momentum p as a function of track length L due to multiple Coulomb scattering.*

Before the above errors can finally be introduced into the ROMEO track bank, we have to transform them into errors w.r.t. to the set of variables (A1,A2,D,B1,B2). This procedure uses the inversion of eq. (3-14) and, as usual, eq. (3-7).

3.6 Vertex Reconstruction

In the case of a 2-V0 trigger, we look for one or two track pairs which may constitute a K^0, Λ, or $\bar{\Lambda}$. ROMEO has very weak rejection criteria for V0's, e.g. e^+e^- pairs are easily accepted. Hence often different track assignments are possible which may lead to different geometry blocks in the output record. These ambiguities have to be resolved later on during the kinematical analysis.

In section 3.6.1 we describe the way in which a reasonably well established vertex is calculated for each V0 candidate in the ROMEO subroutine EXPOL [DUF76].

As far as the errors on the vertex coordinates (x_v, y_v, z_v) are concerned ROMEO only calculates a 3×3 error matrix. Obvious correlations with the kinematical variables $(1/p, \lambda, \phi)$ for each track are ignored.

A vertex fit using the full 5×5 error matrix for each track is done with the program VTXFIT [BIL82] described in the following section 3.6.2. In this case, additional errors due to multiple scattering (see section 3.5) should be taken into account beforehand.

3.6.1 ROMEO Vertex Fit

The method used in EXPOL to find a vertex (x_v, y_v, z_v) is described in [DUF76] which in turn uses the general fit procedure as described by P. Mühlemann [MÜH70].

The determination of the vertex of n tracks by this iteration method proceeds as follows :

1) First we choose a starting value x_v^0 for the x-coordinate of the vertex and compute the track intersections with the plane $x = \text{const.} = x_v^0$ and the tangents to the tracks at these points. That is, we evaluate the constants a_i, b_i $(i = 1,2, \ldots 2n)$ which

represent the tangents to the tracks (cf. the track parametrization in eq. 3-13) :

$$
\begin{aligned}
y &= a_1 x + b_1 \\
z &= a_2 x + b_2 \\
y &= a_3 x + b_3 \\
z &= a_{2n} x + b_{2n}
\end{aligned}
\tag{3-25}
$$

2) Then we determine the point of closest approach of the set of n tangents by the matrix method outlined below. This is the first approximation of the vertex $(x_v^1, y_v^1, z_v^1) = X^1$.

3) Replacing x_v^0 by x_v^1, we compute again intersection coordinates and tangents, in other words, new constants a_i, b_i.

4) The point of closest approach of the tangents gives the second vertex approximation (x_v^2, y_v^2, z_v^2).

5) Repeating this iteration process, we usually reach convergence after 3-5 steps.

4. MATRIX METHOD

To find the point of closest approach of the n tracks, we have to minimize the righthand side of the 2n equations with residuals $r_1, r_2, \ldots r_{2n}$:

$$
\begin{aligned}
a_1 x_v^1 + b_1 - y_v^1 &= r_1 \\
a_2 x_v^1 + b_2 - z_v^1 &= r_2 \\
a_3 x_v^1 + b_3 - y_v^1 &= r_3 \\
&\ldots \\
&\ldots \\
a_{2n} x_v^1 + b_n - z_v^1 &= r_{2n}
\end{aligned}
\tag{3-26}
$$

Using matrix notation, we have

$$A\, X^1 + B = R$$

and we can immediately formulate the weighted least squares condition :

$$\chi^2 = R^t\, W R = (A\, X^1 + B)^t\, W (A\, X^1 + B) = \text{minimum} \qquad (3\text{-}27)$$

which corresponds to :

$$\frac{d\chi^2}{dX^1} = 0 \quad \text{or} \quad A^t\, W (A\, X^1 + B) = 0 \qquad (3\text{-}28)$$

with t denoting the transposed matrix. The weight matrix W contains the errors on the vertex coordinates :

$$W = E^{-1}$$

The improved vertex vector is now :

$$X^1 = -\,(A^t\, W A)^{-1}\, A^t\, W B \qquad (3\text{-}29)$$

and the statistical error on X^1 is given by the error matrix

$$E(X^1) = (A^t\, W A)^{-1} \qquad (3\text{-}30)$$

B. STARTING VALUE

In order to find a starting value X^0 for the above iteration scheme ROMEO proceeds like this :

1. For each pair of tracks, one positive and one negative, calculate, in the XY plane, the two intersections of the circles representing each track in this plane, and this for both stereoscopic view separately.

2. Choose the correct intersection (x_v^0, y_v^0) by checking the corresponding z_v^0 values.

3. Reject V0 candidates for which the sum of the (reversed) momentum vectors does not point towards the target.

After the fit, we obtain a 3×3 error matrix on the vertex coordinates (x_v, y_v, z_v). The track parameters $(1/p, \lambda, \phi)$ are not changed during this procedure.

In order to check whether ROMEO has missed any V0's, a subsequent program VZERO(*) searched for V0 candidates among the so-called extra tracks which ROMEO had not assigned to a V0 beforehand.

3.6.2 Vertex Fit With Full Error Matrix

After the passage of ROMEO, a refined vertex fit can be done with the program VTXFIT, taking into account the full 5×5 error matrix for each track. The following sets of variables are used during the fit :

$(A_1\ A_2\ D\ B_1\ B_2)$	ROMEO OUTPUT
$(1/p\ \lambda\ \phi\ Y\ Z)$	AT FIRST POINT
$(Y\ Z\ A\ B\ 1/p)$	PROPAGATED NEAR VERTEX

The transformation between the first two sets was already given in section 3.4.2 (see eq. (3-14)). In the last set, we use the definitions $A = p_y/p_z$ and $B = p_z/p_x$. Thus, the last two sets of variables transform into each other by :

$$A = \tan\phi \qquad (3\text{-}31)$$

$$B = \tan\lambda \cdot \sqrt{1 + \tan^2}$$

(*) We are grateful to Mr. Baubillier, Paris, for transmitting the VZERO program, which originally was used for the analysis of the experiment WA48 at CERN.

At the beginning of the fit procedure, both tracks are extrapolated from the first measured point to the starting value x_v^0 which is given (as a good first estimate) by ROMEO. For the extrapolation, the tracks are parametrized by a helix of the following form :

$$\boxed{\begin{aligned} x &= X + \rho * (\cos\beta - \cos\beta_0) \\ y &= Y + \rho * (\sin\beta - \sin\beta_0) \\ z &= Z + S * \rho * (\beta - \beta_0) * \tan\lambda \end{aligned}} \qquad (3\text{-}32)$$

where S is the geometrical sign of the track and ρ is given by :

$$\cos\lambda * P = .0002998 * B_Z * \rho \qquad (3\text{-}22)$$

and $\beta = \phi - \frac{S \cdot \pi}{2}$ (see fig. 3-13).

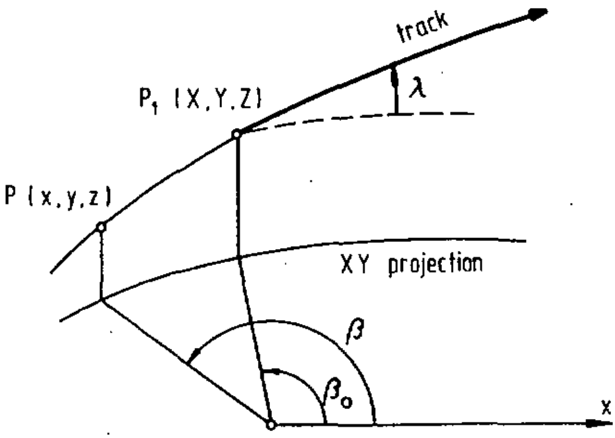

Fig. 3-13 : Helix parametrization.

Actually the track extrapolation is calculated using the routine RKUTAS [WIL74]. For the error determination at the propagated point, the helix parametrization formulae and their derivatives are used, applying, as usual, the error transformation formula eq. (3-7).

The 5 variables x_i adjusted by VTXFIT are $(1/p, \lambda, \phi, Y, Z)$ for each charged track. In principle, an iteration scheme is used to minimize the χ^2-value defined by :

$$\chi^2 = \sum_{i,j} \frac{(x_i^f - x_i^m)(x_j^f - x_j^m)}{\sigma_{ij}} \tag{3-33}$$

It is usually sufficient to leave the iteration loop after the first pass.

As result of the fit a 9×9 covariance matrix is written on to the output record for the 9 variables :

$$(X\ Y\ Z\ 1/p_1\ A_1\ B_1\ 1/p_2\ A_2\ B_2)$$

This "global" error matrix will be used for the fit of the main vertex inside the target (APEX fit) as described in the following section.

As an example, we give the probability distribution of fig. 3-14 which was obtained for V0's belonging to events with at least two V0-candidates found by ROMEO. The beam momentum was 3.-3.3 GeV/c.

Except for low probability values, the distribution is flat indicating that our estimates of errors in ROMEO and the multiple scattering errors are quite good.

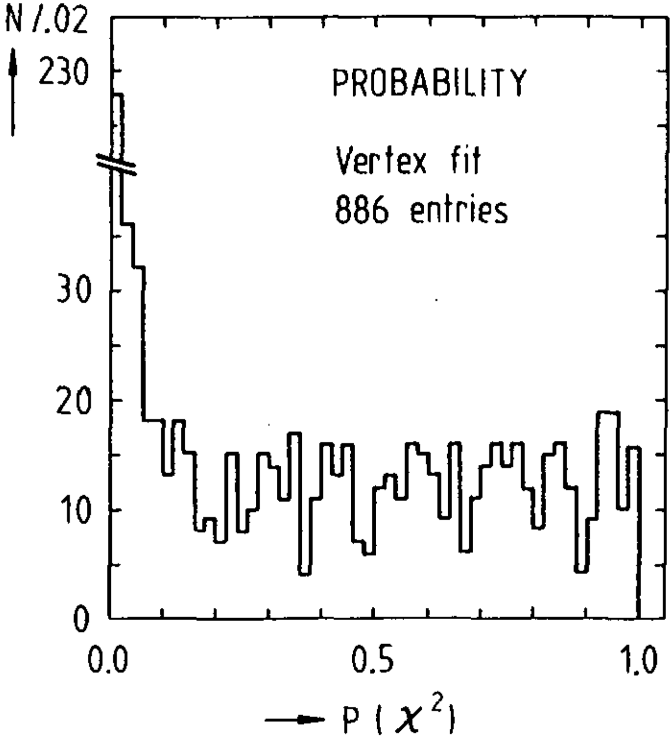

Fig. 3-14 : Probability distribution after the vertex fit of single V0's in 2V0 event candidates.

3.7 Apex Fit

Once a first estimate is found for the main vertex (= apex) inside the hydrogen target and after correction of the beam momentum for eventual energy losses, the fit program described in the preceeding section can be applied.

A. FIRST APEX ESTIMATE

Up to now, ROMEO and the subsequent vertex fitting program have established one or two V0's with momentum $\vec{p}_{V0} = \vec{p}_1 + \vec{p}_2$, where $\vec{p}_1$ and $\vec{p}_2$ are the momenta of the corresponding charged tracks. Extrapolating in the direction $-\vec{p}_{V0}$ towards the target yields one (or two) points P_j of closest approach (see fig. 3-15) with respect to the target axis at positions x_j, $j = 1,2$.

Next the beam is extrapolated from the beginning of the target until the mean value $\bar{x} = (x_1 + x_2)/2$, using the RKUTAS subroutine. This extrapolated point $A_0(\bar{x}, y_{beam}, z_{beam})$ proved to be a good first extimate for the apex position.

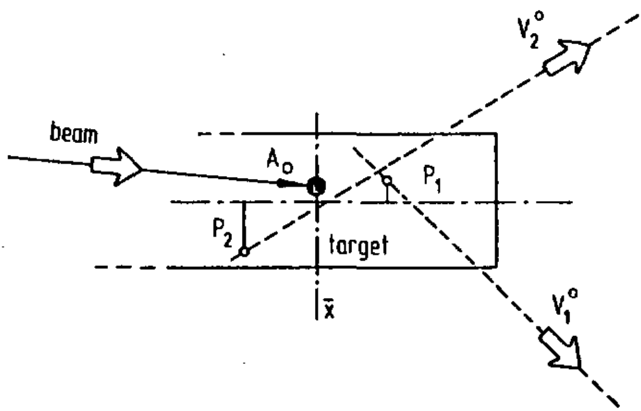

Fig. 3-15 : First apex estimate A_0 from the points of nearest approach P_1 and P_2.

If a point P_j of nearest approach lies too far outside the target w.r.t. the errors on the x,y,z-coordinates, this V0 either does not belong to the event or does not represent a neutral particle, and hence the V0 is dropped.

B. ENERGY LOSS CORRECTIONS

According to the distance which the beam particle travelled through the hydrogen target prior to the collision with a proton, a suitable correction for the energy loss due to electromagnetic interaction must be included. From bubble chamber experiments, Garbincius and Hyman [GAR70] have found :

$$dE/dx = .26 \text{ MeV/cm} \tag{3-34}$$

for $p(\pi^-) > 200$ MeV/c and $p(\bar{p}) > 1300$ MeV/c. This value corresponds to an average ionization potential for H_2 of $I = 20$ eV.

In our case with a target length of 65 cm the maximum energy loss is thus ($\rho_{H_2} = .071 \text{ g/cm}^3$) :

$$\Delta E_{max} = 19 \text{ MeV/c},$$

which corresponds to .64% and .25% of the beam momentum at 3.0 GeV/c and 7.8 GeV/c respectively.

C. ERROR PROPAGATION FOR VO'S

The VTXFIT program which we used for the apex fit needs a 5×5 error matrix on the variables (Y Z A B 1/p) for each track, that is the neutral VO "tracks" and the beam track. For the neutral tracks, we can use the information of the "global" error matrix on the variables (X Y Z A_1 B_1 $1/p_1$ A_2 B_2 $1/p_2$) written on to the output record during the preceeding fit (cf. section 3.6.2). Using the definition of the track tangents $A_i = p_y^i/p_x^i$ and $B_i = p_z^i/p_x^i$ and the vector sum $\vec{p}_{V0} = \vec{p}_1 + \vec{p}_2$, together with the neutral track projections :

$$y = Y_v + A_i \ (x - X_v)$$

$$z = Z_v + B_i \ (x - X_v)$$

we can transform the errors for the two charged tracks into errors for the neutral track, using, as usual, the error transformation formula eq. (3-7).

Finally, we have introduced multiple scattering errors for the beam particle, as described in section 3.5. As an example, we show the probability distribution (fig. 3-16) as obtained during apex fit of events with one or two VO's for the sample at 3. - 3.3 GeV/c.

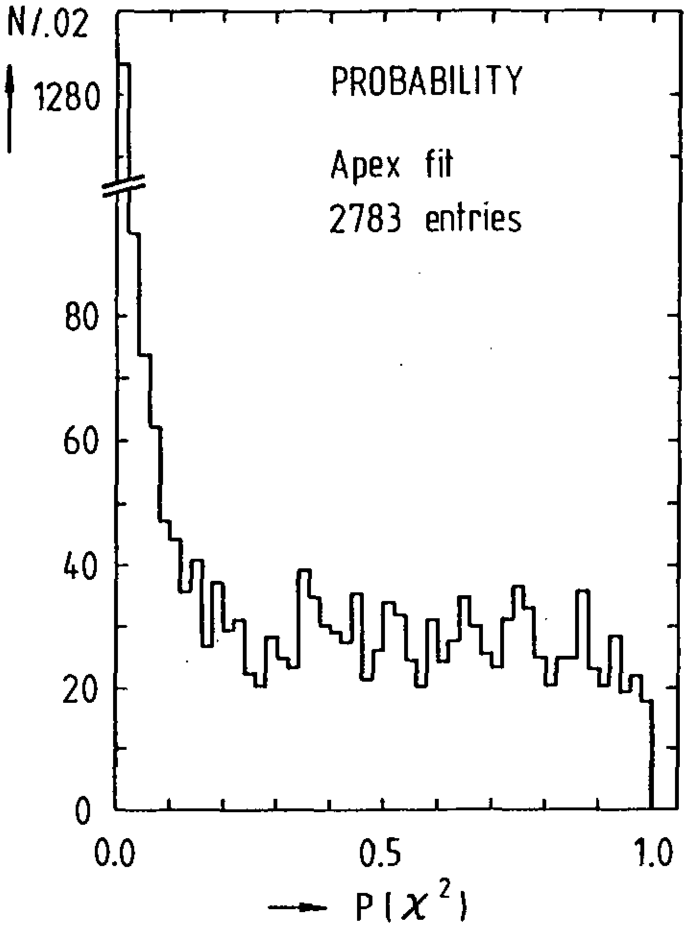

Fig. 3-16 : *Probability distribution after apex fit of 1V0 and 2V0 events.*

4. RESULTS FROM KINEMATICAL ANALYSIS

4. RESULTS FROM KINEMATICAL ANALYSIS

Up to now, only geometrical information, i.e. space coordinates of sparks, and fitted track parameters ($1/p, \lambda, \phi$) have been used to first reconstruct all tracks in space, and then to look for V0 candidates.

If at least one V0 was found, a fit of the main vertex inside the target was supposed to improve a first estimate calculated from points of nearest approach.

In this chapter, we shall test those results under the assumption of representing real physical particles and their interactions. Ambiguities will arise at different stages.

All reaction channels we shall investigate belong to one of the following topologies :

(T_1) 1 - V0 + missing neutral particle MN

(T_2) 2 - V0

(T_3) 2 - V0 + missing neutral particle MN

The topology T_1 category contains two-body events where the second neutral particle was lost during event detection and data acquisition or during off-line analysis (notation, e.g., $\pi^- p \to K^0(\Lambda)$ if the Λ was not detected). Examples of category T3 are found when producing excited neutral particle states which, in turn, decay into two neutrals where only one is detected, as for example in the reaction $\pi^- p \to K^0 \Sigma^{*0} \to K^0 \Lambda(\pi^0)$.

First, a constrained kinematical fit (1 - C) was run on single V0's for all events using the program KOMEGA (described in the next subsection) in order to test the particle hypothesis K^0, Λ, and $\bar{\Lambda}$. Secondly, all 2V0 events with 2 successful particle fits were tested under the hypothesis of belonging to one of the exclusive reaction final states $K^0\Lambda$, $\bar{\Lambda}\Lambda$, or $K^0_S K^0_S$. Since all particles taking part in the reaction are supposed to be known from measurement, imposing energy and momentum conservation makes this test a four constraint fit (4 -C).

Finally, a 1 -C fit with KOMEGA was attempted for 2V0 candidates with a third missing neutral particle γ, π^0 or $n(\bar{n})$. Successful fits may belong to final states like $K^0\Sigma^0$, $\bar{\Lambda}\Sigma^0$ +c.c. (charge conjugate), $K^{*0}\Lambda$, $K^0\Lambda$ $(\bar{n})$, etc.

Results of these kinematical fits will lead to unnormalized raw angular distributions. We will be able to translate them into final differential cross section distributions only after the acceptance of the Omega spectrometer and various normalization coefficients have been established.

4.1 Survey of Overall Analysis

One can discuss which way of doing the total analysis of an event is the best. In fact, after event reconstruction (with ROMEO) mainly two different fit procedures for a 2V0 event could be suggested :

1. First exploit all geometrical information available for each V0 and execute a vertex fit on the track variables $(1/p,\lambda,\phi,Y,Z)$, using the VTXFIT program. Then, after fitting the main vertex (apex), test the particle and reaction hypothesis with KOMEGA.

2. First pass a physical test on the V0's, i.e. test the hypothesis K^0, Λ, $\bar{\Lambda}$ with the KOMEGA program in a 1 -C fit on the track parameters $(1/p,\lambda,\phi)$. Then use these results for a main vertex fit and the final test of reaction hypothesis.

We have tried both ways and comparing the results did not give a clear answer, since both possibilities have advantages and disadvantages : the VTXFIT program failed to fit some of the delicate V0 candidates, like those where one track is badly measured and the error estimates are not very realistic because, e.g., it has turned very quickly (slow track), or because the extrapolation distance to the vertex was too long for the linear approximation to hold during error propagation. The

KOMEGA program disregarded the track and vertex position and easily fitted those candidates.

On the other hand, the VTXFIT program rejected many of the V0's which did not belong to a neutral particle decay and thus reduced the background signal significantly.

We have chosen the first possibility for our analysis. The overall procedure is summarized in the flowchart of fig. 4-1.

4.2 Constrained Single Particle Fit

Testing each V0-candidate under neutral particle hypotheses will not give unique results for all V0's. This may lead to normalization problems, especially in the case of 1-V0 events. Some ambiguities, however, can be resolved by considering their missing mass values and their fit probabilities.

4.2.1 KOMEGA Programs

The program used at this stage of analysis is KOMEGA (Kinematics OMEGA) which is written under conventions of the HYDRA system [HYD74]. For a neutral particle fit, the following results from the analysis, as described in chapter 3, are used as input data for KOMEGA :

- track parameters ($1/p, \lambda, \phi$) for the 2 charged tracks belonging to a V0 candidate,
- errors (measurement and multiple scattering errors) on the parameters and their correlations,
- mass assignments.

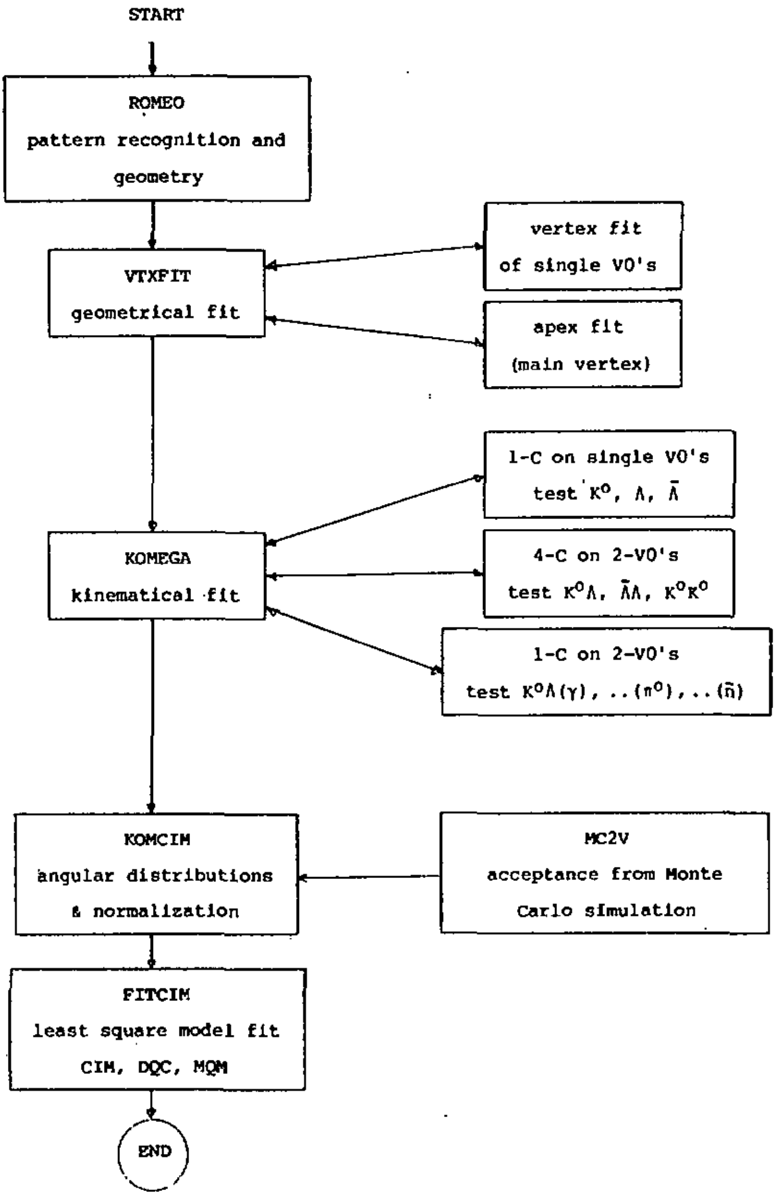

Fig. 4-1 : *Survey of off-line analysis after event reconstruction.*

KOMEGA then tries to adjust energy and momentum conservation for a chosen neutral particle hypothesis :

$$E_{V0} = E_1 + E_2 = \sqrt{m_1^2 + p_1^2} + \sqrt{m_2^2 + p_2^2} \tag{4-1}$$

$$\vec{p}_{V0} = \vec{p}_1 + \vec{p}_2$$

This is a system of 4 independent equations where 3 quantities, however, are not measured : $\vec{p}_{V0}$ or $(1/p_{V0}, \lambda_{V0}, \phi_{V0})$. This is why we are dealing with a one constraint fit (1 -C). In the appendix, a description can be found for a general constrained kinematical fit procedure.

The result of the fit will consist of fitted parameters $(1/p_{V0}, \lambda_{V0}, \phi_{V0})$ and their covariance matrix used for further analysis.

In order to check the validity of the fit, one can calculate the "pull" distributions, i.e. for each fitted quantity x_ν one determines :

$$\mathrm{pull}(x_\nu) = \frac{x_\nu^m - x_\nu^f}{\sqrt{\sigma^2_{x_\nu^m} - \sigma^2_{x_\nu^f}}} \tag{4-2}$$

We have presented the pull distributions of the kinematical variables of 2 charged tracks which are supposed to belong to the decay of a Λ particle in fig. 4-2.

"Ideal" pull distributions are normal distributions with a mean value of 0 and a standard deviation of 1. From fig. 4-2, we can be assured that our 1 -C fit was done correctly and, above all, that the error determination on track variables described in chapter 3 has provided correct input data for the fit.

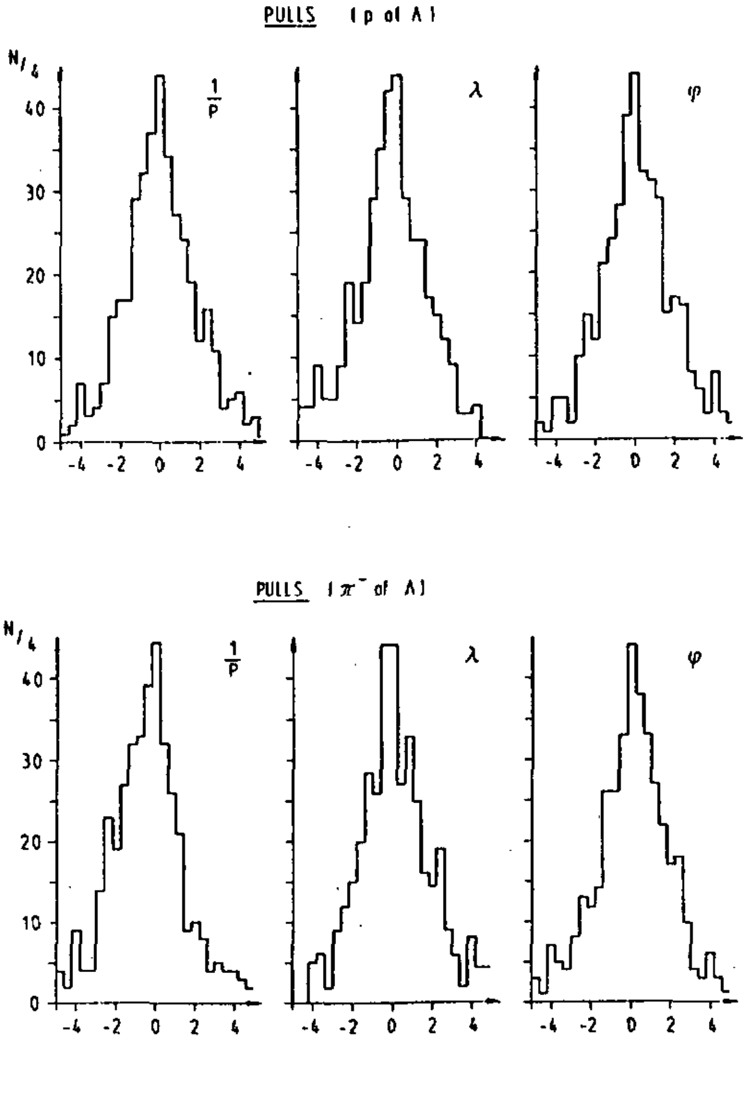

Fig. 4-2 : *Pull distributions after a 1-C KOMEGA fit under the Λ hypothesis.*

4.2.2 Neutral Particle Ambiguities

The fit procedure of V0's may lead to a successful fit for different mass assignments of the two charged tracks. We have investigated how often ambiguities between K^0, Λ, and $\bar{\Lambda}$ hypotheses occures.

In fig. 4-3, a scatter plot with corresponding projections shows the effective mass squared $M^2_{eff}(\pi^+\pi^-)$ versus $M^2_{eff}(p\pi^-)$ for all 2-V0 candidates at p_{lab} = 3. - 3.3 GeV/c where KOMEGA successfully fitted both V0's. No cut in probability was applied so far.

This figure demonstrates that many of the (real) Λ particles may simulate a K^0, whereas only a few K^0 particles simulate a Λ. The difference in contamination is due to different Q-values of K^0 and Λ particles.

An important question is whether these ambiguities can affect the final 2-V0 sample. Without any attempts to reduce single neutral particle ambiguities, we have, e.g., found that for 12 out of 314 2-V0 candidates at 3. - 3.3 GeV/c, both the $K^0\Lambda$ and the ΛK^0 assignment was possible, representing a 4% ambiguity in the $K^0\Lambda$ sample. Separation on the grounds of the product of fit probabilities assured an error of less than 2% for the final normalization which is much smaller than the statistical errors alone.

In the case of 1-V0 events, we have slightly reduced the number of ambiguities : If one of two successful assignments had a probability $P(\chi^2)$ smaller than 5%, we have chosen the fit with probability at least twice as large as the other one. Using event data from the Monte Carlo simulation and imposing track errors according to the distributions found for physical data, we have checked that no neutral particles were lost in the KOMEGA fit.

As an example, we list in table 4-1 the number of successful fits at p_{lab} = 3. - 3.3 GeV/c where the $\pi^-:\bar{p}$ ratio of the beam was about 4:1.

In order to estimate the possible contamination in the number of successful 1-C fits, we used the 2-V0 subsample where an unambiguous $K^0\Lambda$ final state was found from a 4-C kinematical fit (as described later on).

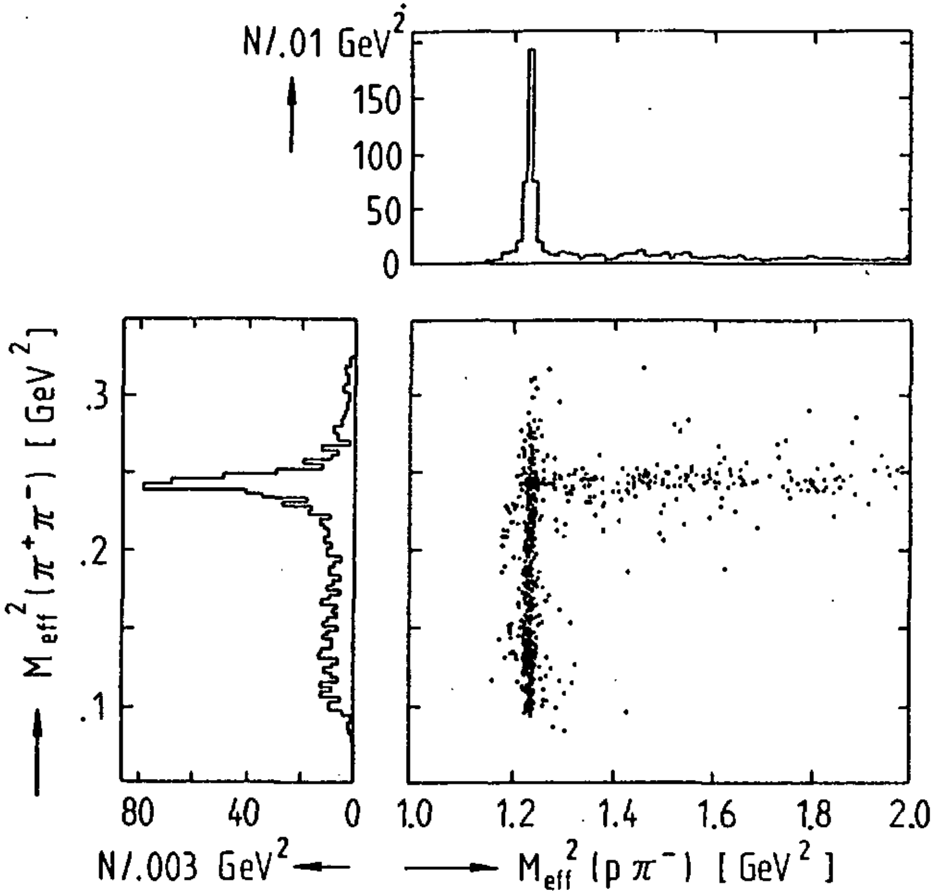

Fig. 4-3 : *Scatter plot of the squared effective masses of single V0's found in 2V0 candidates at p_{lab} around 3 GeV/c under ($p\pi^-$) and ($\pi^+\pi^-$) assignments. The projections show the corresponding Λ and K^0 peaks.*

particle	successful fit	ambiguous with Λ	$\bar{\Lambda}$	K^0
Λ	1414	-	15	395
$\bar{\Lambda}$	630		-	163
K^0	2214			-

Table 4-1 : Neutral particle ambiguities.

Secondly, the Monte Carlo data together with appropriate errors was used to check the consistency of the contamination figures with larger statistics. Thus, neutral particle ambiguities are possible as follows :

$\sim$ 21% of the Λ's (or $\bar{\Lambda}$'s) simulate K^0's

$\sim$ 8% of the K^0's simulate Λ's (or $\bar{\Lambda}$'s)

no ambiguities occur between Λ's and $\bar{\Lambda}$'s

These figures change with the momentum resolution of measured tracks. The $\Lambda/\bar{\Lambda}$ ambiguities listed above were extremely badly measured candidates and hence were assigned to the hypothesis with higher probability.

Ambiguities between K^0 and $\bar{\Lambda}$ assignments are shown in fig. 4-4 (a) for the same sample of V0's, as in the previous figure.

Finally, ambiguities between Λ and γ assignments have to be considered. Fig. 4-4 (b) shows the 2-dimensional plot of the corresponding effective masses.

As we shall show in the chapter on simulation, we could have evicted all γ's already at this stage by introducing a cut in the decay angle distribution (or alternatively in the transverse momentum distribution, which is a more convenient choice) without losing many of the Λ's. But since we checked our reaction hypothesis with the missing mass w.r.t. the properly reconstructed V0, these ambiguities did not survive until the final angular distributions.

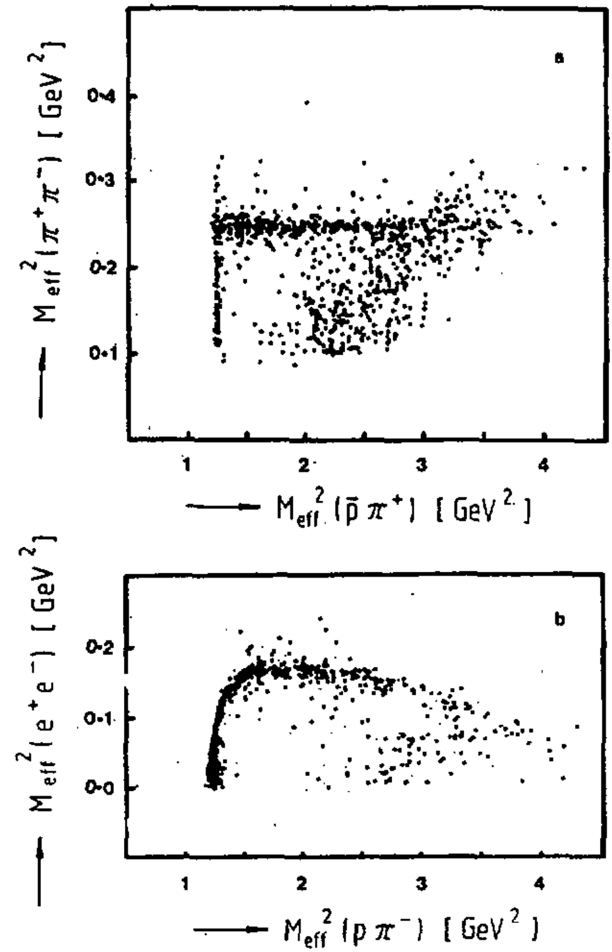

<u>Fig. 4-4</u> : (a) Squared effective masses under the $\bar{\Lambda}$ and K^0 hypothesis for the same V0 sample as in fig. 4-3.

(b) γ hypothesis versus Λ hypothesis.

MASS RESOLUTION IN WA13

The projections of fig. 4-3 are presented again in fig. 4-5 but with the x-axis linear in the effective mass M_{eff}.

From the width of the peak, we can deduce the mass resolution of the spectrometer for our experiment :

$$\boxed{M_{eff}(K^0) = 498 \pm 3.5 \text{ MeV}} \quad (m_0 = 497.67 \text{ MeV})$$

$$\boxed{M_{eff}(\Lambda) = 1116 \pm 1.7 \text{ MeV}} \quad (m_0 = 1115.60 \text{ MeV})$$

This agrees with the values m_0 given by the Particle Data Group [REV80].

4.2.3 Missing Mass Spectra of One V0 Events

Since we have already calculated the beam parameters at the interaction vertex during the apex fit, we can now calculate the missing mass MM(V0) w.r.t. the V0's which successfully fitted a neutral particle hypothesis. MM(V0) is defined as follows :

$$MM^2(V0) = (E_{lab} - E_{V0})^2 - (|\vec{p}_{lab} - \vec{p}_{V0}|)^2 \tag{4-3}$$

where $E_{lab} = E_{beam} + E_{target} = \sqrt{m^2 + p_{lab}^2} + m_p$.

Fig. 4-6 shows the missing mass distributions w.r.t. Λ (a) and w.r.t. K^0-particles (b) at $p_{lab} = 3. - 3.3$ GeV/c in the π^- beam. Ambiguities are <u>not</u> removed. The contribution which is due to 2-V0 events only is also shown : events assigned to the $K^0\Lambda$ reaction channel are given by the dotted line, those assigned to the $K^0\Sigma^0$ channel by the dashed line.

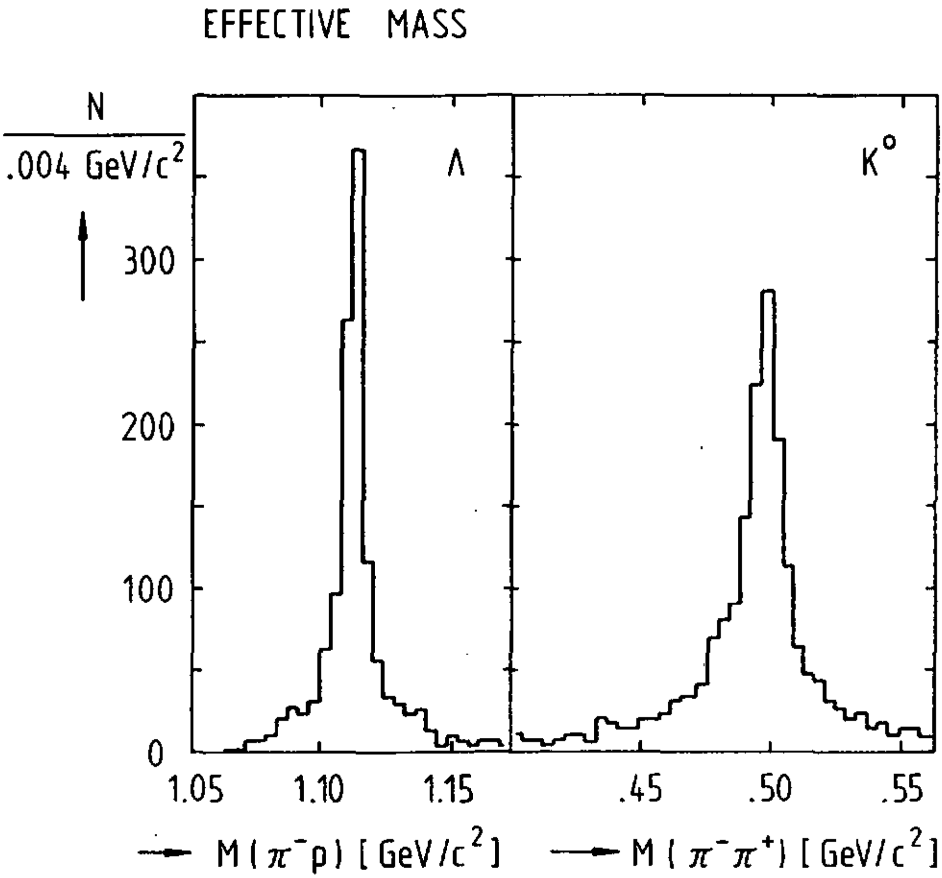

Fig. 4-6 : Effective mass distributions including all V0's at 3 GeV/c which were assigned to the Λ and K^0 sample after the KOMEGA fit. The mass resolution of WA13 can be deduced from the widths of the distributions.

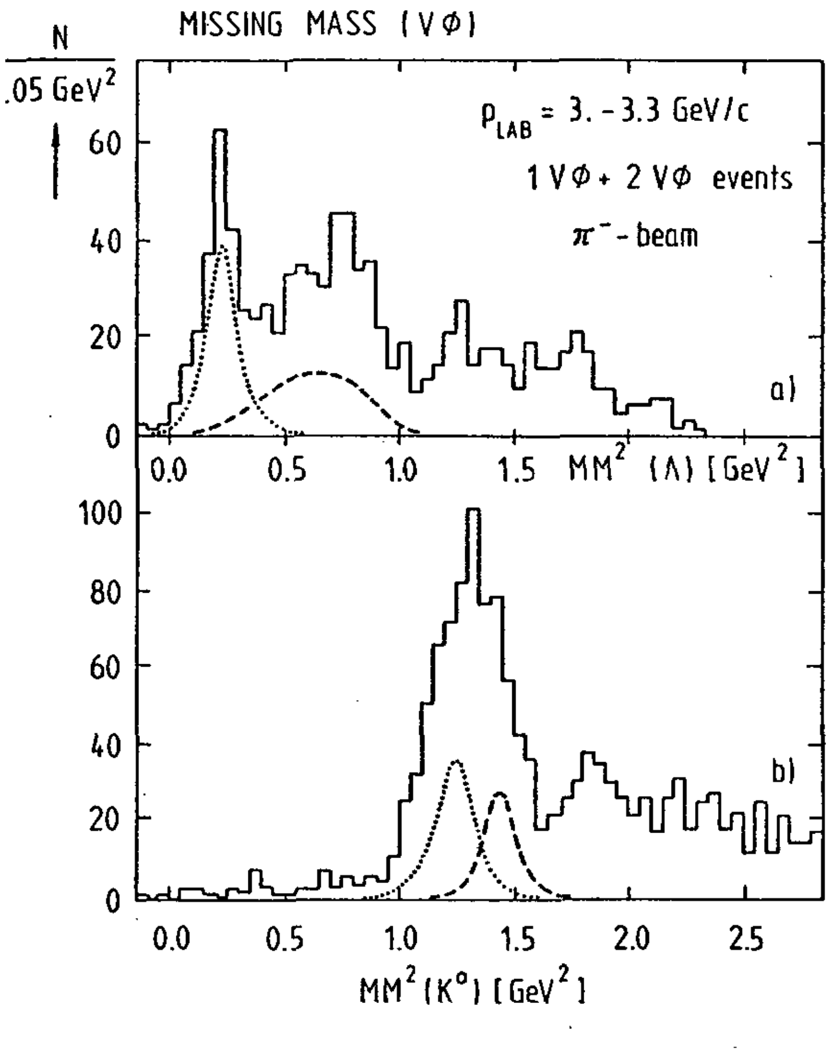

Fig. 4-6 : *Squared missing mass with respect to (a) Λ and (b) K^0 at p_{lab} around 3 GeV/c for 1V0 and 2V0 events. The dotted and dashed line indicate the contribution from 2V0 events which were assigned to the $K^0\Lambda$ and $K^0\Sigma^0$ sample respectively.*

First one realizes that the peaks from missing Λ's and missing Σ^0's overlap considerably even at low beam momenta. Next, one can deduce that most of the K^0's anticipated from the peak in the missing mass distribution w.r.t. Λ will reappear in the 2-V0 event sample, whereas about half of the Λ's forseeable from the Λ/Σ^0 peak in the missing mass distribution w.r.t. K^0 were not reconstructed. We will have to find the reasons for this before normalizing the resulting angular distributions.

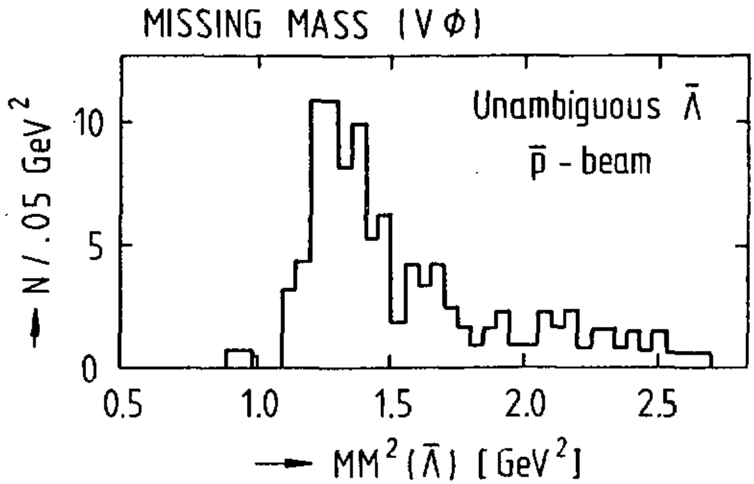

Fig. 4-7 : *Squared missing mass distribution with respect to $\bar{\Lambda}$ at p_{lab} around 3 GeV/c in the $\bar{p}$ beam.*

To be complete, the missing mass distribution w.r.t. $\bar{\Lambda}$ is shown in fig. 4-7. Only unambiguously assigned $\bar{\Lambda}$'s from $\bar{p}p$ events are represented.

Again the large peak in the spectrum belongs to associated Λ or Σ^0 particles.

4.3 Final Fit of Reaction Hypotheses

All 2-V0 candidates where both V0's have successfully fitted at least one of the neutral particle hypotheses will now be tested under the assumption of belonging to a physical reaction channel.

Ambiguities arising frequently for reactions with a (third) missing neutral particle can be resolved in most cases by considering the missing mass values and corresponding errors, the probability of the fit, and the effective mass values of appropriate particle combinations.

4.3.1 4-C Fit And 1-C Fit For 2-V0 Events

Once again we employed the KOMEGA program to perform a constrained kinematical fit on 2-V0 events. For channels where one of the neutral final state particles could not be detected, the four constraints from energy and momentum conservation are reduced to one constraint.

In table 4-2, a survey of all tested channels is given.

All topologies belong either to the category 2-V0 (T2) or to the category 2-V0 + missing neutral particle MN (T3). The last column in the table lists the most important reaction channels tested, p.s. stands for the phase space contribution. The hypotheses 1 - 5 are the most important ones as far as the event numbers are concerned.

hypotheses Nr.	topology		KOMEGA fit	reaction channels (p.s. = phase space)
1	$\bar{\Lambda}\Lambda$	T2	4-C	$\bar{p}p \rightarrow \bar{\Lambda}\Lambda$
2	$K^0\Lambda$	T2	4-C	$\pi^-p \rightarrow K^0\Lambda$
3	K^0K^0	T2	4-C	$\bar{p}p \rightarrow K^0K^0$
4	$\bar{\Lambda}\Lambda(\gamma)$	T3	1-C	$\bar{p}p \rightarrow \bar{\Lambda}\Sigma^0 + \bar{\Sigma}^0\Lambda$
5	$K^0\Lambda(\gamma)$	T3	1-C	$\pi^-p \rightarrow K^0\Sigma^0$
6	$\bar{\Lambda}\Lambda(\pi^0)$	T3	1-C	$\bar{p}p \rightarrow \bar{\Lambda}\Sigma^{0*}$ + c.c., p.s.
7	$K^0\Lambda(\pi^0)$	T3	1-C	$\pi^-p \rightarrow K^0\Sigma^{0*}$, $K^{0*}\Lambda$, p.s.
8	$K^0\Lambda(\bar{n})$	T3	1-C	$\bar{p}p \rightarrow \bar{\Lambda}^*\Lambda$, p.s.
9	$\bar{\Lambda}K^0(n)$	T3	1-C	$\bar{p}p \rightarrow \bar{\Lambda}\Lambda^*$, p.s.
10	$K^0K^0(n)$	T3	1-C	$\pi^-p \rightarrow K^0\Lambda^*$, fn, p.s.

Table 4-2 : Reaction hypotheses tested by KOMEGA.

4.3.2 Separation Criteria

Reactions we are most interested in are those numbered 1 and 2 (topology T2) in table 4-2 and the reactions 4 and 5 (topology T3) with a missing γ from the shortlived Σ^0 particle decaying electromagnetically via $\Sigma^0 \rightarrow \Lambda\gamma$.

Ambiguities which were difficult to separate occurred for successful missing γ and missing π^0 assignments.

An example of possible ambiguous results after the KOMEGA fit is given in table 4-3 for 412 2-V0 candidates at 3. - 3.3 GeV/c.

hypotheses		1 $\bar{\Lambda}\Lambda$	2 $K^0\Lambda$	4 $\bar{\Lambda}\Lambda(\gamma)$	5 $K^0\Lambda(\gamma)$	6 $\bar{\Lambda}\Lambda(\pi^0)$	7 $K^0\Lambda(\pi^0)$	10 $K^0K^0(n)$
1	$\bar{\Lambda}\Lambda$	27	--	5	--	--	--	--
2	$K^0\Lambda$	--	140	--	27	--	5	--
4	$\bar{\Lambda}\Lambda(\gamma)$	--	--	37	--	6	--	--
5	$K^0\Lambda(\gamma)$	--	--	--	167	--	43	--
6	$\bar{\Lambda}\Lambda(\pi^0)$	--	--	--	--	15	--	--
7	$K^0\Lambda(\pi^0)$	--	--	--	--	--	98	--
10	$K^0K^0(n)$	--	--	--	--	--	--	42

Table 4-3 : Reaction ambiguities.

While no cut in probability has been applied so far, we rejected those 1-C fits where the squared missing mass MM^2(tot) w.r.t. the 2-V0's found is more than 3 standard deviations away from the predicted squared missing neutral particle mass (γ,π^0 or n). The definition of MM(tot) is analogous to eq. (4-3) :

$$MM^2(\text{tot}) = (E_{lab} - E_{2V0})^2 - \left(|\vec{p}_{lab} - \vec{p}_{2V0}|\right)^2$$

where E_{2V0} = sum of the two neutral particle energies and $\vec{p}_{2V0}$ = sum of the corresponding 3-momenta.

The widths of these distributions were established from unambiguous events. At higher energies, poor statistics did not allow the use of these distributions, but the expected widths could be roughly predicted from low momentum extrapolations and checked with the Monte Carlo data.

Thus, we are certain that no events have been lost in table 4-3.

None of the reconstructed events fitted the annihilation process $\bar{p}p \rightarrow \bar{K}^0K^0$.

It is interesting to illustrate the different results in a 2-dimensional plot which shows the measured squared missing mass MM^2 w.r.t. the first V0 versus MM^2 w.r.t. the second V0. Fig. 4-8 contains results for the topologies T2 and T3 in the π^- beam (2-V0 = K^0 Λ) and fig. 4-9 contains the same topologies in the $\bar{p}$-beam with 2-V0 = $\bar{\Lambda}\Lambda$. The dotted line marks the allowed domain of different reaction channels.

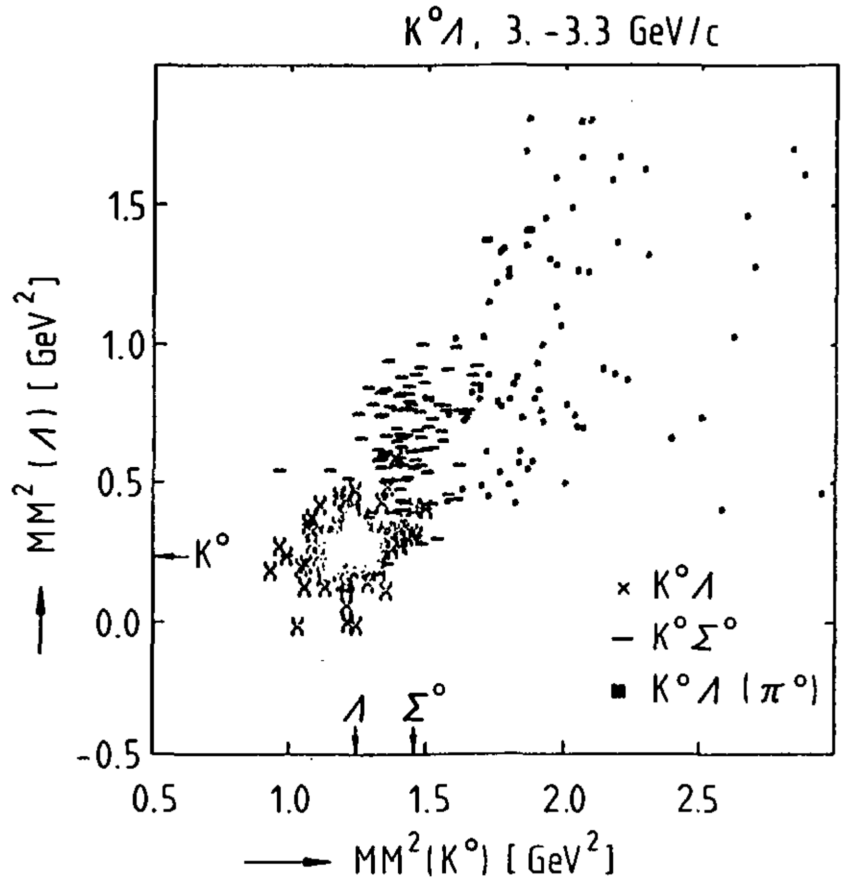

Fig. 4-8 : *Scatter plot of squared missing masses with respect to K^0 and Λ including all 2V0 events which successfully fitted the $K^0\Lambda$, $K^0\Sigma^0$ and $K^0\Lambda(\pi^0)$ final state hypotheses. Double assignments are possible.*

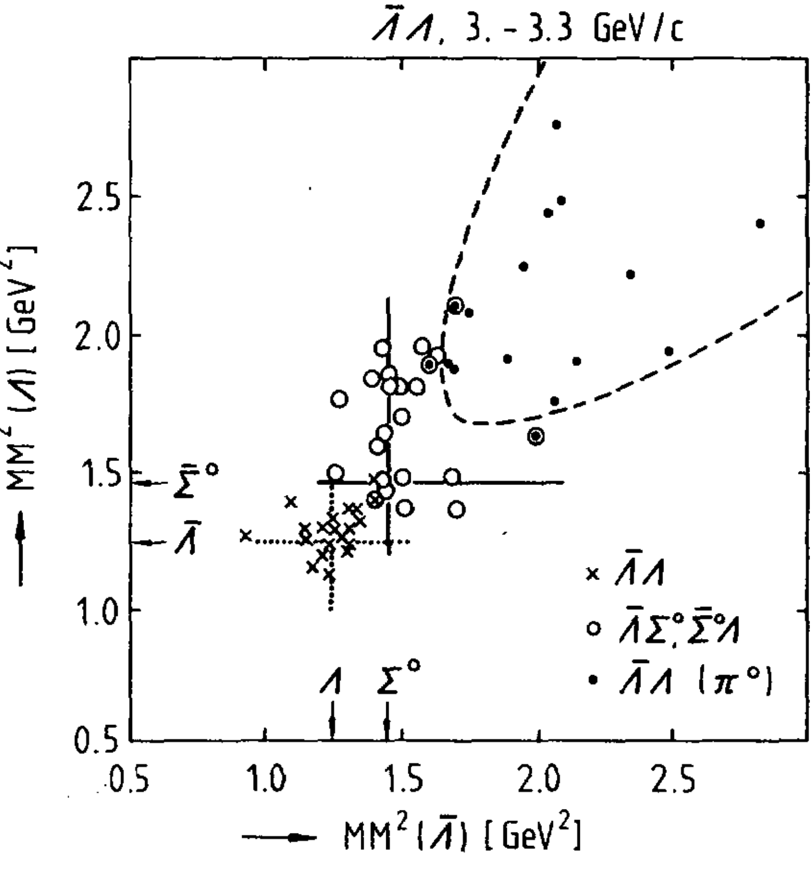

Fig. 4-9 : *Scatter plot of squared missing masses w.r.t. $\bar{\Lambda}$ and Λ $\bar{\Lambda}\Lambda$, $\bar{\Lambda}\Sigma^0$, $\bar{\Sigma}^0\Lambda$, and $\bar{\Lambda}\Lambda(\pi^0)$ final state hypotheses at p_{lab} around 3 GeV/c. Ambiguities are included.*

Now let us say a few words about how the ambiguities listed above were assigned to the different reaction channels.

TOPOLOGY T2 EVENTS

It was not difficult to isolate the exclusive hypothesis of topology *T2*, i.e. $K^o\Lambda$ and $\bar{\Lambda}\Lambda$ final states. Since their kinematical fit is most constrained, we accepted all T2 candidates in table 4-3 if their total missing mass was compatible with 0. The remaining events belonged to the T3 topology 2-V0 + missing neutral MN, where MN is either γ or π^o.

No ambiguities are possible with missing neutron events.

The resulting missing mass distributions for events *assigned to the channel* $\pi^- p \to K^o\Lambda$ are given in fig. 4-10.

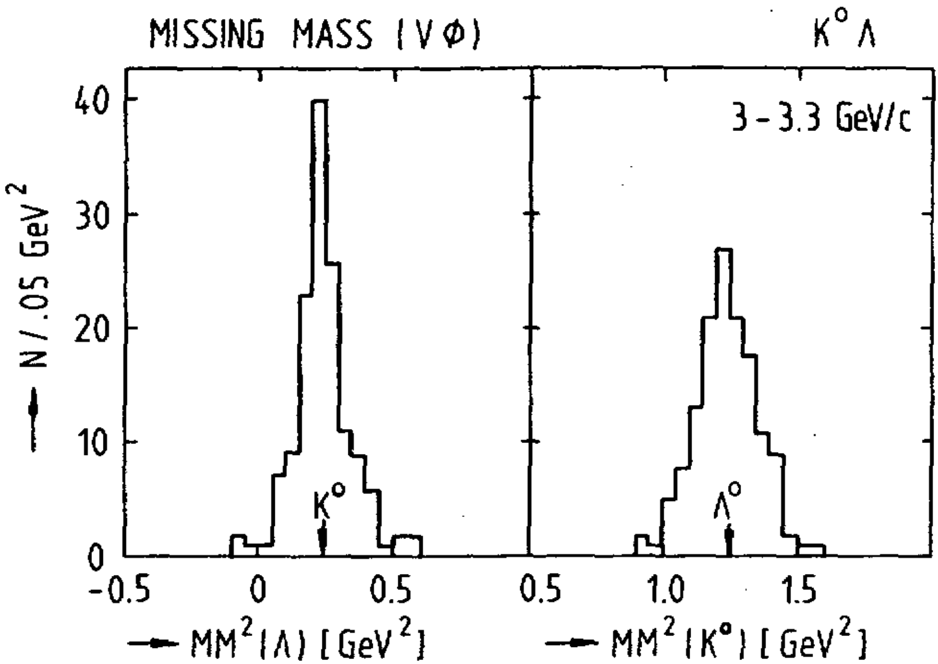

Fig. 4-10 : Squared missing mass distributions w.r.t. Λ *and* K^o *in the final* $K^o\Lambda$ *event sample at* $p_{lab} = 3$ *GeV/c.*

TOPOLOGY T3 EVENTS

The final attribution of ambiguous T3 topologies to one of the possible reaction channels was done by deciding upon the following criteria :

1. Reject the 2-V0 + γ hypothesis if the effective mass $M_{eff}(\Lambda\gamma)$ or $M_{eff}(\bar{\Lambda}\gamma)$, using fitted quantities, is incompatible with Σ^0 or $\bar{\Sigma}^0$ mass respectively.

2. Reject the 2-V0 + π^0 hypothesis if the (measured) squared missing mass w.r.t. the first V0 lies below the corresponding limits, within errors, of the squared effective mass of the second V0 and the π^0, that is, if MM (V0) is incompatible with the phase space distribution. For example, $M^2_{eff}(\Lambda\pi^0) > 1.564$ GeV^2 and $M^2_{eff}(K^0\pi^0) > .401$ GeV^2 within errors.

3. Decide for the remaining ambiguities by selecting the hypothesis with higher fit probability $P(\chi^2)$.

TOPOLOGY T1 EVENTS

In order to increase the statistics obtained from topology T2 events alone, we included some of the T1 events (1-V0 + MN) when the missing mass MM(V0) indicated the correct anticipated mass m_m of the missing neutral particle. The decision to include a candidate was based on the following tests :

1. probability $P(\chi^2)$ of geometrical vertex fit,
2. probability $P(\chi^2)$ of apex fit,
3. no ambiguities from neutral particle kinematical fit,
4. $|MM^2(V0) - m_m^2|$ < one standard deviation σ_m.

At P_{lab} = 3 GeV/c, for example, the width of the missing mass distribution σ_m was 0.1 GeV^2, as can be seen from fig. 4-10.

Some of the accepted 1-V0 events gave contributions to the angular distributions in strong forward (and, in same cases, in strong backward) direction where the acceptance is not well known.

4.3.3 Λ/Σ^0 Ambiguities

Since we shall later on combine the differential cross section of exclusive final states $K^0\Lambda$ and $\bar{\Lambda}\Lambda$ from topology T2 with $K^0\Sigma^0$ and $\bar{\Lambda}\Sigma^0$, respectively from topology T3, the resolution of Λ/Σ^0 ambiguities is not important while establishing the angular distributions. However, for extracting the polarization data and for comparison with other experiments, it is useful to know both contributions.

For the $K^0\Sigma^0$ final state hypothesis, we have given the probability $P(\chi^2)$ distribution in fig. 4-11 (a). The effective mass between the (fitted Λ and γ particle for all successful 1-C fits is given in fig. 4-11 (b). One clearly obtains a Σ^0 peak with some events belonging to the $K^0\Lambda$ (π^0) sample (indicated by the dashed line). The dotted lines delimit the region outside of which no Σ^0 particle assignment was accepted.

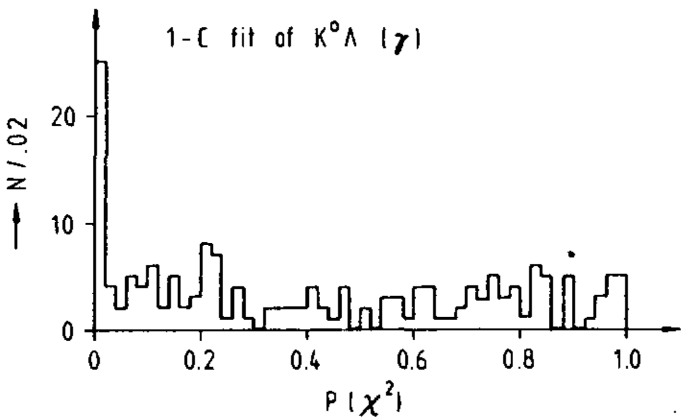

Fig. 4-11 : (a) Probability distribution from the one constraint fit of the reaction hypothesis $\pi^-p \rightarrow K^0\Sigma^0$ at 3 GeV/c.

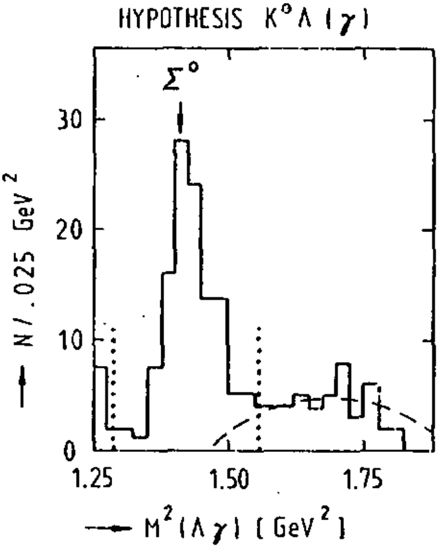

Fig. 4-11 (cont.) : *(b) Squared effective mass between Λ and (fitted) γ in the $K^0\Lambda(\gamma)$ sample at 3 GeV/c.*

Following the separation criteria described in the last subsection yields the final sample of $K^0\Sigma^0$. One can check the consistency of the $K^0\Lambda$ and $K^0\Sigma^0$ sample by plotting the decay angle distribution of the Σ^0 in its center of mass system : it should be flat for real $K^0\Sigma^0$ events. Fig. 4-12 shows the result for both the K^0 Λ and the $K^0\Sigma^0$ sample if one plots the distribution in $\cos\theta_\Sigma$, where θ_Σ is defined as the angle between the measured Λ momentum and the missing momentum $\vec{p}_m$ w.r.t. the fitted K^0 momentum, i.e. $\vec{p}_m = \vec{p}_{lab} - \vec{p}_{K^0}$. For the K^0 Λ sample alone, one expects a sharp peak at $\cos\theta_\Sigma = 1.0$ ($\vec{p}_m = \vec{p}_\Lambda$).

The shaded area in fig. 4-12 represents the events of the K^0 Λ final states alone. As expected, there is a peak at $\cos\theta_\Sigma = 1.0$ followed by a tail due to the errors on measured quantities. The $K^0\Sigma^0$ sample on the other hand, gives a uniformly distributed contribution indicating that our separation procedure worked quite well.

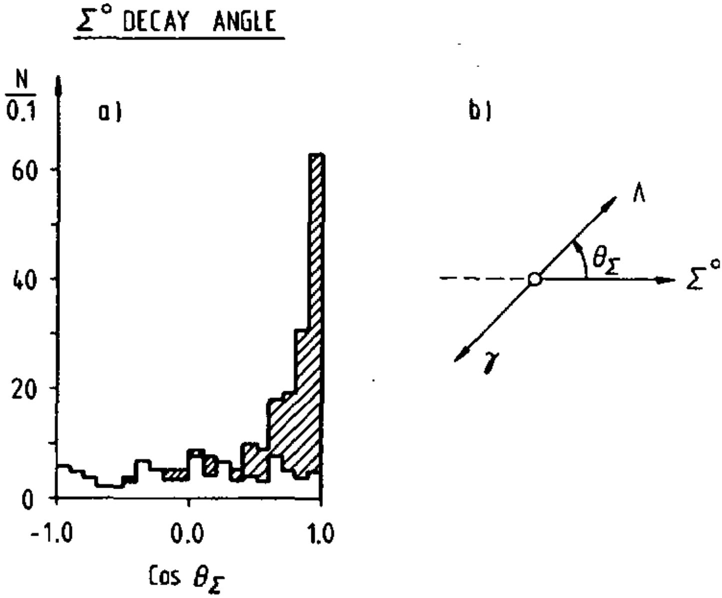

Fig. 4-12 : (a) *c.m. decay angle distribution for the* Σ^0 *from* $K^0\Sigma^0$ *final states. The shaded area represents* $K^0\Lambda$ *final states.*

(b) *Definition of* Σ^0 *decay angle in the* Σ^0 *rest frame.*

4.3.4 Events with Missing π^0 or n

Finally, some of the successful 1-C KOMEGA fits came from the $K^0\Lambda$ + MN and $\bar{\Lambda}\Lambda$ + MN hypothesis, where MN = π^0 or n. In both cases, the unavoidable background signal imposes the search for a compromise between background reduction and real event rejection since we cannot, except for some special reaction channels, apply cuts in effective mass, as was the case for $K^0\Sigma^0$ and $\bar{\Lambda}\Sigma^0$ final states.

In general, we will have two contributions : The first one from phase space, and the second one from excited neutral meson or baryon states which decay into π^0 (or n) and the second detected neutral particle. Possible candidates are given in table 4-5 (numerical values from [REV80]). Some decay modes with important branching ratios are included, though we did not analyse them in this experiment.

excited state [MeV]	decay mode	branching ratio [%]	$I(J^P)$	decay width [MeV]
K^* (892)	$\longrightarrow K\pi$	$\sim$ 100	1/2(1-)	50.3 ± .8
K^* (1430)	$\longrightarrow K\pi$	$\sim$ 49.1	1/2(2+)	100. ± 10
	$\longrightarrow K^*\pi$	$\sim$ 27.0		
Λ^* (1520)	$\longrightarrow \bar{K}n$	46 ± 1	0(3/2-)	15.5 ± 1.5
	$\longrightarrow \Sigma\pi$	42 ± 1		
Σ^* (1385)	$\longrightarrow \Lambda\pi$	88 ± 2	1(3/2+)	$\sim$ 35
	$\longrightarrow \Sigma\pi$	12 ± 2		

Table 4-5 : Excited strange particle states.

Fig. 4-13 shows the two effective mass distributions of interest in the case of $K^0\,\Lambda(\pi^0)$ at 3. - 3.3 GeV/c. For the total missing mass MM^2(tot), we required $|MM^2(\text{tot}) - m^2_{\pi^0}| < .014$ GeV , where $m^2_{\pi^0} = .018$ GeV^2. Though the number of events is rather limited, one can distinguish a contribution from $K^{0*}(892)$ in the $M^2_{eff}(K^0\,\pi^0)$ distribution and Σ^{*0} (1385) in the $M^2_{eff}(\Lambda\pi^0)$ distribution.

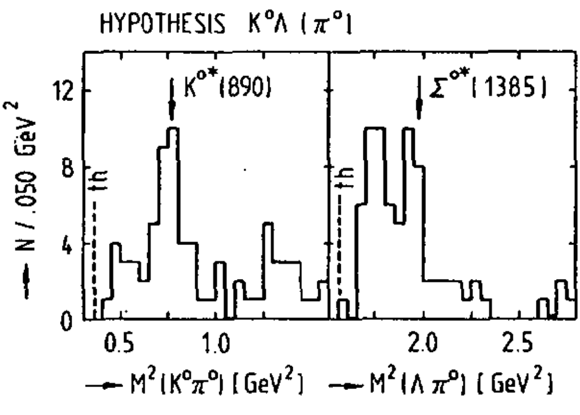

Fig. 4-13 : Effective mass distributions in the $K^0\Lambda(\pi^0)$ sample at 3 GeV/c for (a) K^0 and π^0 particles and (b) Λ and π^0 particles. 'th' marks the threshold in both cases.

MISSING NEUTRON HYPOTHESIS

Possible reaction channels are indicated under hypotheses 8 - 10 in table 4-2. At p_{lab} = 3. - 3.3 GeV/c, no significant signal appeared at the mass of the $\Lambda^*(1520)$ particle for the reaction $\bar{p}p \rightarrow \bar{\Lambda}\Lambda^*$ + c.c. (hypotheses 8 and 9). The missing masa distribution w.r.t. the two detected V0's for the $K^0K^0(n)$ hypothesis is given in fig. 4-14 (a), which shows a clear neutron signal. We applied a probability cut at $P(\chi^2)$ = .01 in order to reduce the background.

In a recent analysis at 3.95 GeV/c, Loverre et al. looked for resonance production in the K^0K^0 system [LOV80]. They found contributions mainly from the f(1270) meson with $J^P = 2^+$ and from $\epsilon(1300)$ with $J^P = 0^+$, I = 0.

In fig. 4-14 (b), we have plotted the affective mass spectrum between the two K^0's. One is tempted to identify a signal at the mass of the f'(1515) meson, which can decay into $\pi^0\pi^0$ and K^0K^0, but our limited statistics does not allow any further precisions.

From the WA13 trigger setup, some of the events with missing neutron n (or $\bar{n}$) should have been suppressed by the $\bar{n}$-veto counter. We shall come back to this question when calculating the acceptance in chapter 5.

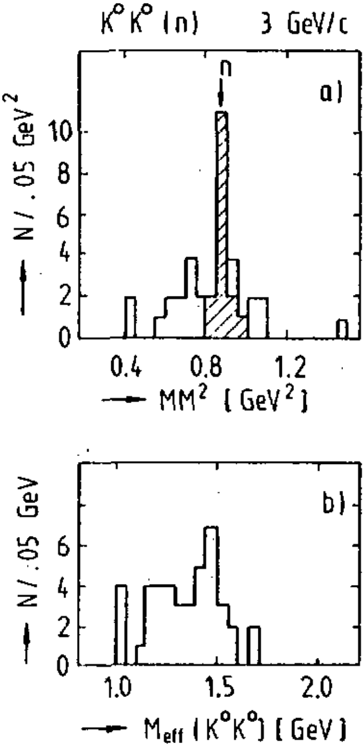

Fig. 4-14 : $K^oK^o(n)$ *final states at* p_{lab} *around 3 GeV/c.*

(a) total missing mass distribution with respect to 2V0,

(b) effective mass distribution between the two K^o*'s after 1-C fit .*

4.4 Raw Angular Distributions

Applying the separation criteria described above, we obtained a certain estimate N of the number of events and the statistical error ΔN for each reaction channel.

The separation became more and more difficult when considering the results at higher beam momenta, since the missing mass distributions w.r.t. one V0 became larger and ambiguities occured more frequently, especially between the 2-V0 + (γ) and 2-V0 + (π^0) hypotheses.

The following table 4-6 gives a summary of the event numbers retained after the analysis of WA13. The errors given correspond to uncertainties in separation of ambiguous assignments.

reaction channel	event numbers for different p_{lab} [GeV/c]			
	3. - 3.3	4.95	7.8	11.7
$\bar{p}p \longrightarrow \bar{\Lambda}\Lambda + \bar{\Lambda}\Sigma^0 + c.c$	50	1	30	9
1V0 + 2V0	92	1	--	--
$\bar{\Lambda}\Lambda$ only	26 ± 1	1	--	--
$\bar{\Lambda}\Sigma^0$ only	24 ± 4	0	--	--
$\pi^- p \longrightarrow K^0\Lambda + K^0\Sigma^0$	237	24	13	3
1V0 + 2V0	455	53	--	--
$K^0\Lambda$ only	138 ± 2	13 ± 2	--	--
$K^0\Sigma^0$ only	99 ± 13	11 ± 4	--	--
$\bar{p}p \longrightarrow \bar{\Lambda}\Lambda(\pi^0)$	10 ± 3	0	--	--
$\pi^- p \longrightarrow K^0\Lambda(\pi^0)$	43 ± 11	6 ± 2	--	--
$\pi^- p \longrightarrow K^0K^0(n)$	16	6	--	--

Table 4-6 : Event number in final sample.

The corresponding unnormalized angular distributions are given for p_{lab} = 3. - 3.3 GeV/c in fig. 4-15, for 4.95 GeV/c in fig. 4-16 (a), (b), for 7.8 GeV/c and 11.7 GeV/c in fig. 4-16 (c), (d) and (e), (f), respectively. During data taking at 4.95 GeV/c, unfortunately the $\bar{p}$ were suppressed in the beam, so only one event was found, for $\bar{\Lambda}\Lambda$ final state, at $\cos\theta^*$ = .5 .

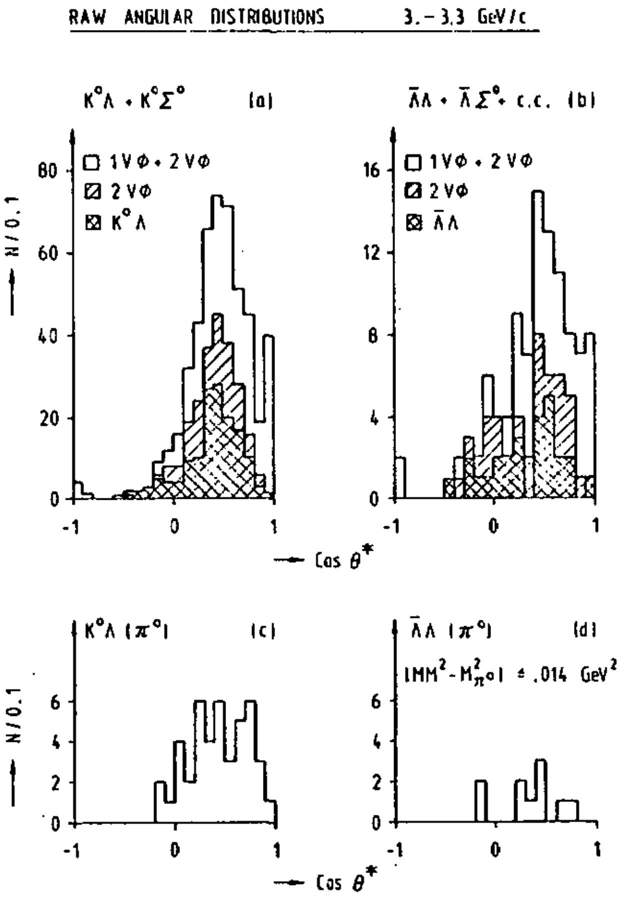

Fig. 4-15 : *Raw angular distributions of the final event sample at p_{lab} around 3 GeV/c.*

(a) $\pi^-p \rightarrow K^0\Lambda + K^0\Sigma^0$, *(c)* $\pi^-p \rightarrow K^0\Lambda(\pi^0)$, *and*

(b) $\bar{p}p \rightarrow \bar{\Lambda}\Lambda + \bar{\Lambda}\Sigma^0 + c.c.$, *(d)* $\bar{p}p \rightarrow \bar{\Lambda}\Lambda(\pi^0)$.

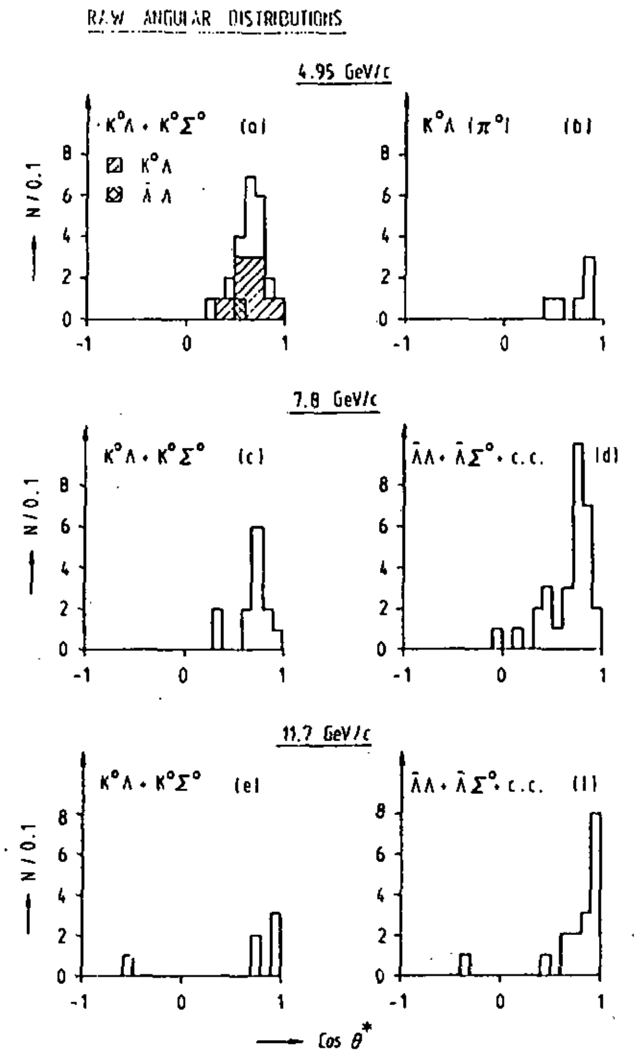

Fig. 4-16 : *Raw angular distributions of the final event sample at different WA13 beam momenta :*

(a + b) 4.95 GeV/c,

(c + d) 7.8 GeV/c, and

(e + f) 11.7 GeV/c.

5. GEOMETRICAL ACCEPTANCE AND NORMALIZATION

5. GEOMETRICAL ACCEPTANCE AND NORMALIZATION

It was one of the main features of the WA13 electronics trigger layout to suppress scattering in forward and backward direction. The acceptance of the spectrometer was maximum in the 90^0 cms region.

Apart from discussing the Monte Carlo program used for the acceptance calculation and comparing physical results with those from simulated events, we shall discuss in this chapter what kind of hardware and software inefficiencies had to be considered and how the raw angular distributions were normalized.

5.1 Acceptance from Monte Carlo Simulation

Since it would be too complicated to calculate analytically the final probability distribution for accepting an interaction by use of the so-called direct method, that is by using the initial random distributions with respect to random variables like dip angle, azimuth angle, lifetime, apex position, etc., we employed the standard method for high energy physics experiments which consists in running relatively straightforward but time consuming Monte Carlo simulations. Supposing all input distributions were known analytically, the direct method would provide an "exact" final probability distributions, whereas the Monte Carlo method is bound to exhaustively consume any computer time allocation in the physicist's desperate attempt to reproduce all peculiarities of his apparatus and to reduce the statistical errors to as low a level as to suggest exact results.

5.1.1 Method

The principle of the Monte Carlo method consists of choosing randomly an initial event configuration for a given c.m.s. scattering angle θ^*, then to test whether the simulated triggar arrangement accepts this event, and finally to repeat the procedure a certain number of times to obtain the acceptence $\alpha(z)$, where $z = \cos\theta^*$ and $\alpha(z)$ is the ratio between the number of accepted events and the number of generated events.

So first starting values have to be chosen for a number of random variables that define the initial event configurstion (see table 5-1). The probability distributions may represent idealizations of the real behaviour of a given variable.

	random variabls x	distribution parameters x, σ_x
beam	p_{lab} momentum	normal distribution : $\bar{x} = p_{nom}$; $\sigma_p \hat{=} 1.5\,\%$
	λ dip angls	"
	ϕ azimuth	"
apex	x-coordinate	exponential distribution : X_0 = absorption length in H_2
	y-coordinate	normal distribution : $\sigma_y = 1$ cm
	z-coordinate	"
interaction	$\cos\theta^*$ scatt. angle	isotropic distribution
	ϕ_{yz}	"
		→ $\vec{p}_{cms}$ of outgoing particles
V0 decay	τ lifetime	exponential distribution : τ_0 = mean life
		→ vertex coordinates
	$\cos\theta_{V0}$ decay	isotropic distribution (no polarization !)
	ϕ_{V0} angles	"
		→ $\vec{p}$ of charged tracks

Table 5-1 : Input variables for Monte Carlo.

The set of chosen values is called a simulated event. It consists of a beam track, a main vertex (apex), two VO vertices, and 4 charged tracks from the neutral particle decays.

The next step is to send this event through the simulated apparatus. The impact of charged tracks on various detector devices can be calculated by assuming a helix track parametrization and using the RKUTAS routine for extrapolation, as described during event reconstruction. Thus the creation of veto signals from the end cap EC or the cylindrical scintillator CYL and the trigger chamber response from the coplanarity chamber CC and from the scintillator S6 can be simulated. As soon as a veto signal is built up the event is dropped and a new initial configuration is chosen randomly. Events that produced a positive trigger signal are saved on magnetic tape for further use. Fig. 5-1 summarizes the simulation procedure.

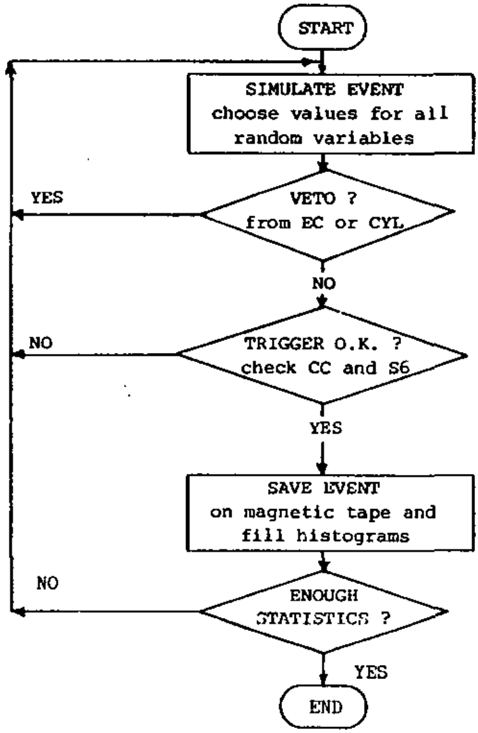

Fig. 5-1 : Flowchart with principle steps in the Monte Carlo program.

Some surprises turned up during data taking of WA13 and even during off-line analysis concerning the performance of special parts of the detector. For example, only after event reconstruction did we realize by inspection of the main vertex coordinates inside the target that the liquid hydrogen level had not reached its maximum value. This had to be introduced into the Monte Carlo program in order to check whether varying the liquid hydrogen level changed the shape of the angular distribution of accepted events. (Apart from that the normalization constants had to be changed accordingly.)

This explains the shape of the apex z-coordinate distribution in fig. 5-2 which is shown together with the distributions for the x- and y-coordinates as they were used as input for the Monte Carlo simulation.

In addition, the efficiency of each part of the detector had to be taken into account. As far as the spark chambers and their optical detection system are concerned, we will discuss them in the next section, together with the event reconstruction losses. Inefficiencies of scintillators (like EC, CYL, and S6) and of the coplanarity chamber CC were determined by comparing the number of actually detected hits with the number of predicted hits.

Thus the efficiencies found for the 6 plastic scintillator slabs S6 were :

A	B	C	D	E	F	
100	98.2	91.4	89.8	93.8	100	[%]

The low values in the central region were due to relatively high counting rates.

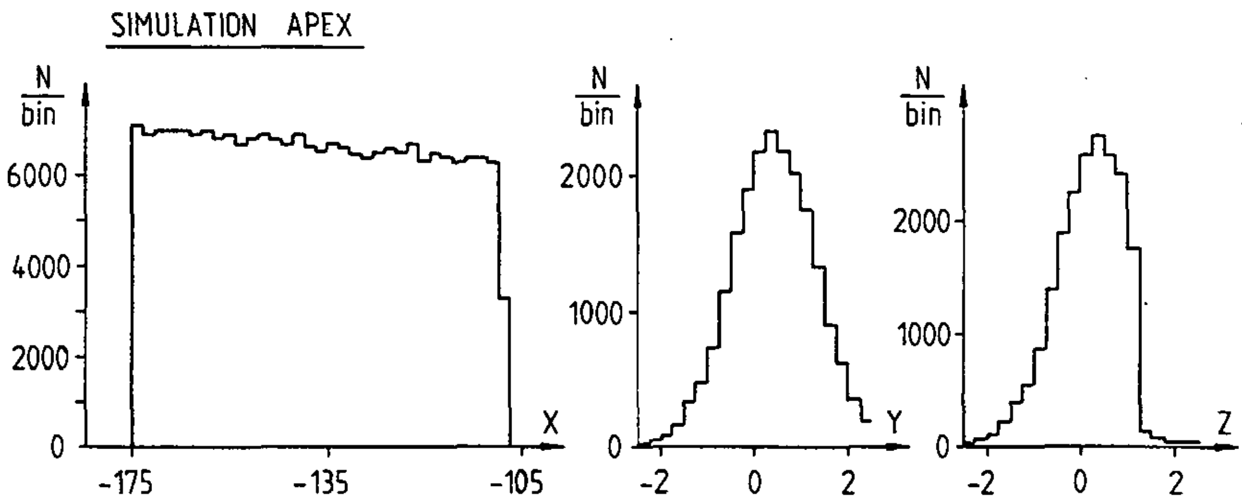

<u>Fig. 5-2</u> : Input random distributions of apex-coordinates for the Monte Carlo simulation.

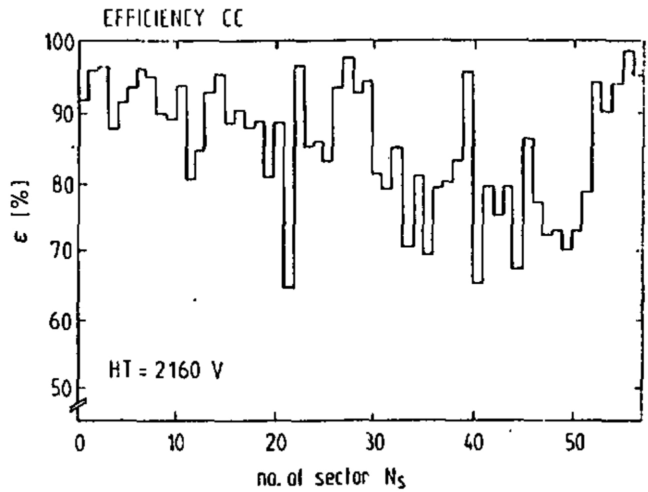

Fig. 5-3 : Efficiencies of sectors of the coplanarity chamber CC.

Fig. 5-3 shows the efficiency of each of the 57 sectors of the coplanarity chamber. The high voltage HT was such that an optimum was obtained between low crosstalk and little spurious signals on the one hand and high efficiency on the other hand.

To show how many of the simulated events survived at different levels of the Monte Carlo program, we give the figures for the reaction $\pi^- p \to K^0 \Lambda$ at 3.1 GeV/c :

200 393	100.0 %	simulated events at input
30 118	15.0 %	events after veto (EC and CYL)
8 356	4.2 %	events after trigger chamber CC
5 000	2.5 %	accepted events after S6

A sample of finally accepted events is shown in the 2-dimensional plot of fig. 5-4, where the two axes are $\cos\theta^*$ (scattering angle θ^*) and ϕ_{yz} (angle of the projected momentum of the scattered meson on to the yz-plane). In the 1-dimensional ϕ_{yz} projection, one can distinguish an enhancement each time the K^0 flies towards one of the corners of the coplanarity chamber. The second projection demonstrates that events with a scattering angle in forward or backward direction have been dropped. This distribution, if normalized with respect to the initial $\cos\theta^*$ distribution, represents the geometrical acceptance of the trigger electronics.

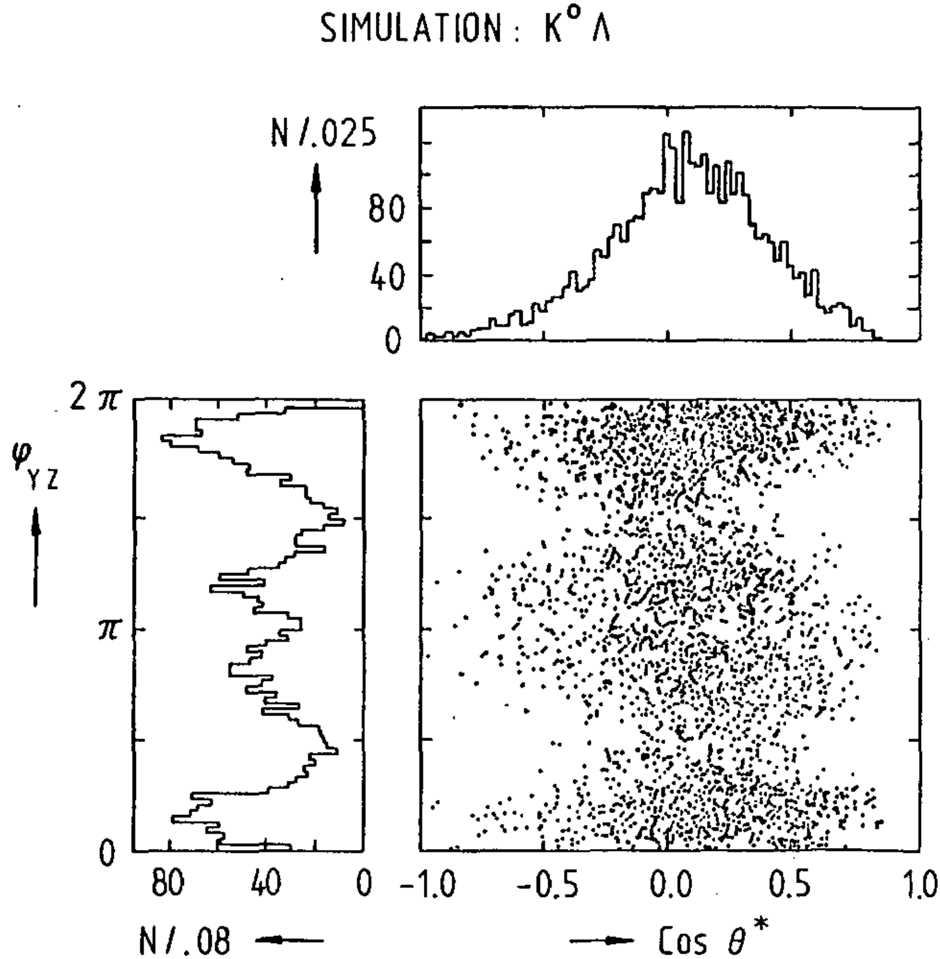

Fig. 5-4 : *Scatter plot of azimuth angle ϕ_{YZ} versus scattering angle $\cos\theta^*$ for accepted $K^0\Lambda$ events.*

Up to now, events were simulated by assuming an isotropic distribution in the variable $\cos\theta^*$. Thus a first approximation of the shape of the differential cross section distribution could be calculated using the results from the kinematical analysis. This gave a more realistic input for the second Monte Carlo run. It changed appreciably the ϕ_{yz} distribution and gave more realistic results for the decay length distribution of V0's. The acceptance itself, however, changed very little.

5.1.2 Results

For each of the reaction hypotheses listed in table 4-2 of the preceding chapter, we had to calculate the acceptance at each value of the WA13 beam momentum. One simplification, however, was introduced at low energies : results at 3.1 GeV/c were used to linearly extrapolate to 3.0, 3.2 and 3.3 GeV/c. Possible errors due to this procedure should be smaller than 0.5%.

The results for the geometrical acceptance for the reaction $\pi^- p \rightarrow K^0\Lambda$ at different beam momenta and $\bar{p}p \rightarrow \bar{\Lambda}\Lambda$ at 7.8 GeV/c are given in fig. 5-5 (a) and fig. 5-5 (b) respectively. For comparison, we show the acceptance for the corresponding elastic channel $\pi^- p \rightarrow \pi^- p$ at 4.95 GeV/c (dotted line).

At the same time, we have plotted in fig. 5-5 (b) the acceptance for the K^0 K^0 and $K^0\Lambda\bar{n}$ final state, and for the reaction $\pi^- p \rightarrow K^0 K^0 n$, all at p_{lab} = 7.8 GeV/c.

Up to now, branching ratios were disregarded, we will introduce them during normalization.

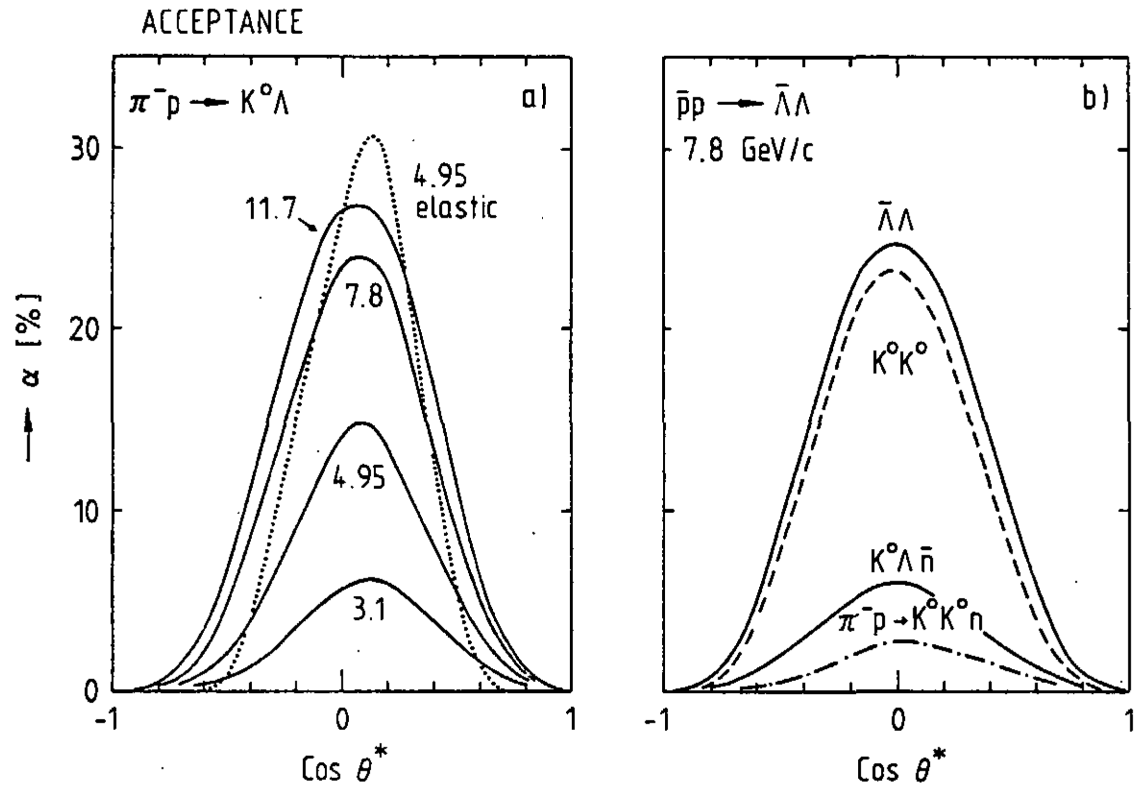

<u>Fig. 5-5</u> : (a) *Geometrical acceptance for the reaction $\pi^- p \rightarrow K^0\Lambda$ at different beam momenta (values given are in GeV/c).*

(b) *Acceptance for different $\bar{p}$ induced reactions at p_{lab} = 7.8 GeV/c and for the reaction $\pi^- p \rightarrow K^0K^0$ (n).*

ACCEPTANCE FOR EVENTS WITH MISSING γ

The acceptance for the reaction channels $\pi^- p \to K^0\Sigma^0$ and $\bar{p}\, p \to \bar{\Lambda}\, \Sigma^0$ + c.c. are slightly smaller than the corresponding channels where Σ^0 is replaced by Λ. On an average, we found :

$$\alpha(\Sigma^0) = .97\ \alpha(\Lambda)$$

ACCEPTANCE FOR TOPOLOGY T1 EVENTS

For 50 000 simulated 1-V0 events for the reaction $\pi^- p \to K^0\Lambda$, where the second V0 was supposed to disintegrate outside the detector volume or to decay into a non-visible mode, we have found only 8 (4) events where the K^0 (Λ respectively) alone had given a positive trigger signal. Hence, if α_{1V} and α_{2V} denote the acceptance for events with one or two V^0, respectively, which disintegrate inside the detector volume, we have

$$\alpha_{1v} = \frac{1}{110}\,\alpha_{2v}\ .$$

This means that for virtually all events recorded on tape, the electronics trigger had seen both V0's. In topology T1 events, i.e. 1-V0 + missing mass, the second V0 usually must have been lost due to reconstruction inefficiencies and not because of undetectible decay modes of neutral particles.

5.2 Corrections for Reconstruction Inefficiencies

The geometrical acceptance function $a_{geom}(\cos\theta^*)$ calculated by the Monte Carlo program did not cover the determination of inefficiencies in the spark chamber modules and the optical detection system, which may have caused track losses or even event losses. Inefficiencies were probably different for Geometry I and Geometry II chambers.

Furthermore, losses could occur during the off-line analysis, for example in ROMEO, or during the different fitting procedures. They depend on different parameters : x-coordinate of interaction vertex inside the target, scattering angle, decay lengths, staggering, number of detected sparks for a track, or number of parasitic sparks in the near neighbourhood of tracks. Some tracks, and hence V0's, could be lost if their momentum was very small or if they passed in between spark chamber modules.

We have tried to account for all different sources of inefficiencies at the same time by an indirect method which compares the properly reconstructed events of Topology T1 with those of Topology T2.

The question is whether one global correction factor ε_{2V0} will be sufficient or whether we have to introduce an efficiency $\varepsilon(x)$ as a function of an appropriately chosen variable x.

Fig. 5-6 suggests an answer to this question. For a given interval in $\cos\theta^*$, we have determined the number of events, N_1 where at least one V0 was fitted to the K^0 or Λ hypothesis with a good χ^2 probability and where the missing mass with respect to this V0 indicated the second neutral particle in the reaction $\pi^- p \to K^0\Lambda$. Then we looked for 2-V0 candidates in the same sample which fitted this reaction.

Thus we obtained the event number N_2. The ratio $\frac{N_1}{N_1 + N_2}$ as a function of $\cos\theta^*$ is shown in fig. 5-6.

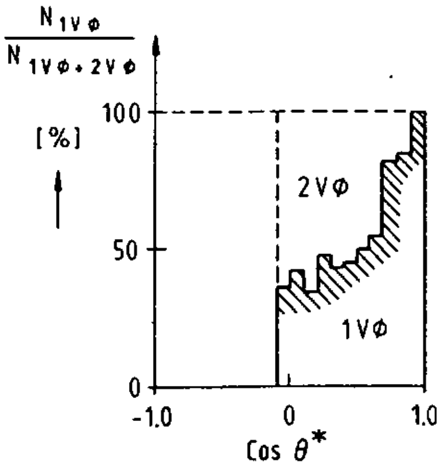

Fig. 5-6 : *Ratio between the number of 1V0 events and the sum of 1V0 + 2V0 events (in percent) in the $K^0\Lambda$ sample at 3 GeV/c.*

This shows clearly that the 2-V0 reconstruction inefficiency is strongly angle dependent. So we need an additional acceptance function $\alpha_{rec}(\cos\theta^*)$.

The above ratio cannot, however, answer the two following questions :

1. Are detection and reconstruction inefficiencies the same for different kinds of V0's, i.e. for K^0, Λ, and $\bar{\Lambda}$?

2. Which variable do these inefficiencies depend on mainly ?

The answer to the first question will supply global correction coefficients whereas the second answer should give the reason for the angular dependence of α_{rec}.

Let us tackle the first part. The total number of interactions $\pi^- p \to K^0\Lambda$ that occurred inside the spectrometer, N_{tot}, can be written as a sum of the number of reconstructed 2-V0 events, $N_{K^0\Lambda}$, the number of 1-V0 events, $N_{K^0(\Lambda)}$ and $N_{\Lambda(K^0)}$, where the missing Λ and missing K^0 respectively are indicated by the missing mass with respect to the V0 found, and the number of lost events, N_{lost}.

$$N_{tot} = N_{K^0\Lambda} + N_{K^0(\Lambda)} + N_{\Lambda(K^0)} + N_{lost} \qquad (5\text{-}1)$$

Using a sample at p_{lab} = 3. - 3.3 GeV/c and 4.95 GeV/c, we found the following figures :

$N_{K^0\Lambda}$	$N_{K^0(\Lambda)}$	$N_{\Lambda(K^0)}$
111	90	16

Hence the single V0 efficiencies are :

$$\varepsilon_{K^0} = \frac{N_{K^0\Lambda}}{N_{K^0\Lambda} + N_{\Lambda(K^0)}} = .87 \pm .12 \qquad (5\text{-}2)$$

$$\varepsilon_{\Lambda} = \frac{N_{K^0\Lambda}}{N_{K^0\Lambda} + N_{K^0(\Lambda)}} = .55 \pm .07$$

This corresponds to an overall detection and reconstruction efficiency for $K^0\Lambda$ events of

$$\boxed{\varepsilon_{K^0\Lambda} = .48 \pm .09}$$

The value for the $\bar{\Lambda}$ particle was determined with a smaller event sample. We found :

$$\varepsilon_{\bar{\Lambda}} = .74 \pm .19$$

which yields for all final atates :

$$\boxed{\varepsilon_{\bar{\Lambda}\Lambda} = .41 \pm .12}$$

As far as the second question is concerned, we have already listed a number of possible variables at the beginning of this section. From the fact that the Λ particle in a $\bar{p}\,p \to \bar{\Lambda}\Lambda$ or $\pi^- p \to K^0\Lambda$ reaction takes away a relatively small amount of momentum, one can understand that the decay meson with its still smaller momentum, say p_{min}, can easily get lost, for example, during the track finding part of ROMEO. In addition, these vertices will often be situated in the Geometry II detector region.

So we hypothesized that *a correct determination of the reconstruction* efficiency as a function of the smallest momentum of the outgoing tracks, $\varepsilon(p_{min})$, could explain the angular dependence of the acceptance function $\alpha_{rec}(\cos\theta^*)$.

The function $\varepsilon(p_{min})$ was obtained by comparing the p_{min} distribution in the reconstructed 2-V0 event sample with the same distribution in the simulated event sample after the second Monte Carlo run. The shape of $\varepsilon(p_{min})$ was approximated by a function as is shown in fig. 5-7 (a).

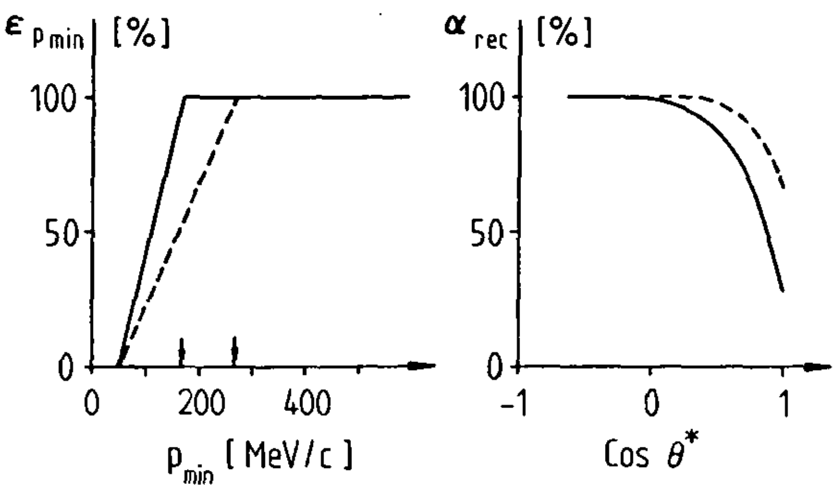

<u>Fig. 5-7</u> : (a) *Reconstruction efficiency as a function of the smallest momentum, p_{min}, of the decay products. (Full line at 3 GeV/c, dotted line at higher momenta.)*

(b) *Variation of geometrical acceptance due to low momentum losses.*

No V0's were reconstructed with p_{min} < 50 MeV/c. We supposed the function $\varepsilon(p_{min})$ to be flat for p_{min} > 170 MeV/c at p_{lab} around 3 GeV/c and 270 MeV/c at higher beam momenta.

Applying this efficiency function to the simulated events changed their angular distribution (as a function of $\cos\theta^*$) as is indicated in fig. 5-7 (b). $\alpha_{rec}(\cos\theta^*)$ is calculated as the ratio between the number of simulated events after and before randomly rejecting events according to $\varepsilon(p_{min})$. With increasing beam momentum the values of p_{min} also are increasing and the losses are smaller at 8 and 12 GeV/c.

Altogether we have obtained two resulta. First we have determined a global correction factor ε_{2V0} for the reconstruction of 2-V0 events and the corresponding single V0 reconstruction efficiencies ε_{K^0}, ε_{Λ}, and $\varepsilon_{\bar{\Lambda}}$, and secondly the correct angular dependence is given by the (normalized) distribution $\alpha_{rec}(\cos\theta^*)$.

5.3 Decay Angle Distributions

It will be important for the determination of the hyperon polarization to verify that results are not biased by acceptance effects due to the experimental setup.

We first have to define the conventions used for the coordinate system in the rest frame of a hyperon. As is shown in fig. 5-8 (b), the y-axis is chosen parallel to the normal $\hat{n}$ to the production plane (fig. 5-8 (a)), the z-axis follows the hyperon momentum, and the x-axis completes a right-handed orthogonal coordinate system. Then the polarization P of the Λ particle is defined as :

$$P = \frac{3}{\alpha_{\Lambda}} \langle\cos\theta_{pol}\rangle \qquad (5\text{-}3)$$

where α_{Λ} = .642 is the decay asymmetry parameter, $\theta_{pol} = \theta_y$ is the angle between the decay proton and the y-axis.

The angle θ_z in fig. 5-8 is the decay angle in the hyperon rest frame.

During Monte Carlo simulation, we assumed all neutral particles to be unpolarized. This was assured by choosing initial isotropic probability distributions for the decay angle θ_z and for the corresponding azimuth angle in the xy-projection of the positively charged decay particle.

The resulting distributions after the Monte Carlo run are given in fig. 5-9. For $\sim$ 870 accepted events for the reaction $\pi^- p \rightarrow K^0 \Lambda$, we plotted for both neutral particles the decay angle distributions ($\cos\theta_z$) in fig. 5-9 (a), the polarization angle distributions ($\cos\theta_y$) in fig. 5-9 (b), and finally the resulting polarization values as defined in eq. (5-3) as a function of the c.m.s. scattering angle $\cos\theta^*$ in fig. 5-9 (c), including statistical errors.

What are the conclusions to be drawn from these results ? All distributions concerning the K^0 particle are compatible with uniform distributions indicated by dashed lines. So the geometrical acceptance has not affected them. For the Λ particle, however, the decay angle distribution is heavily distorted. This may be explained by the fact that, if the proton from Λ decay has a large momentum component in the direction of the Λ momentum in the laboratory frame, then the π^- particle may not be able to reach the coplanarity chamber since its Lorentz boost is too small. Thus, these event configurations are bound to be lost.

On the other hand, the polarization angle distribution for Λ is compatible with a uniform distribution. The polarization itself vanishes.

Hence, for both K^0 and Λ particles, the geometrical acceptance did not introduce any bias for the polarization measurement, as is proven by fig. 5-9 (c).

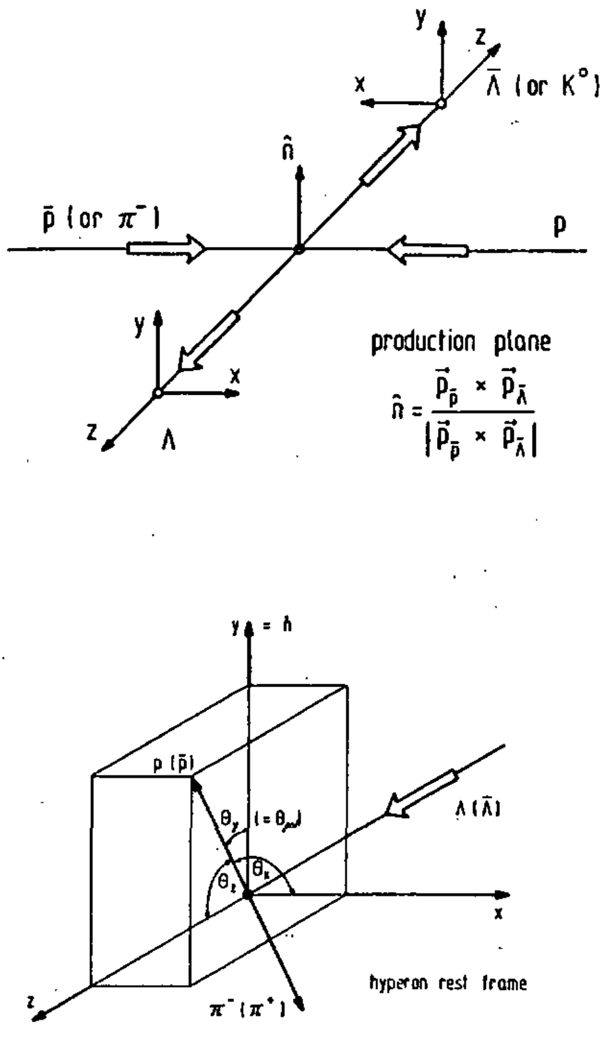

<u>*Fig. 5-8*</u> : *(a) Definition of coordinate system in the c.m.s. of the reaction.*

(b) Hyperon decay angles in its rest frame.

SIMULATED EVENTS

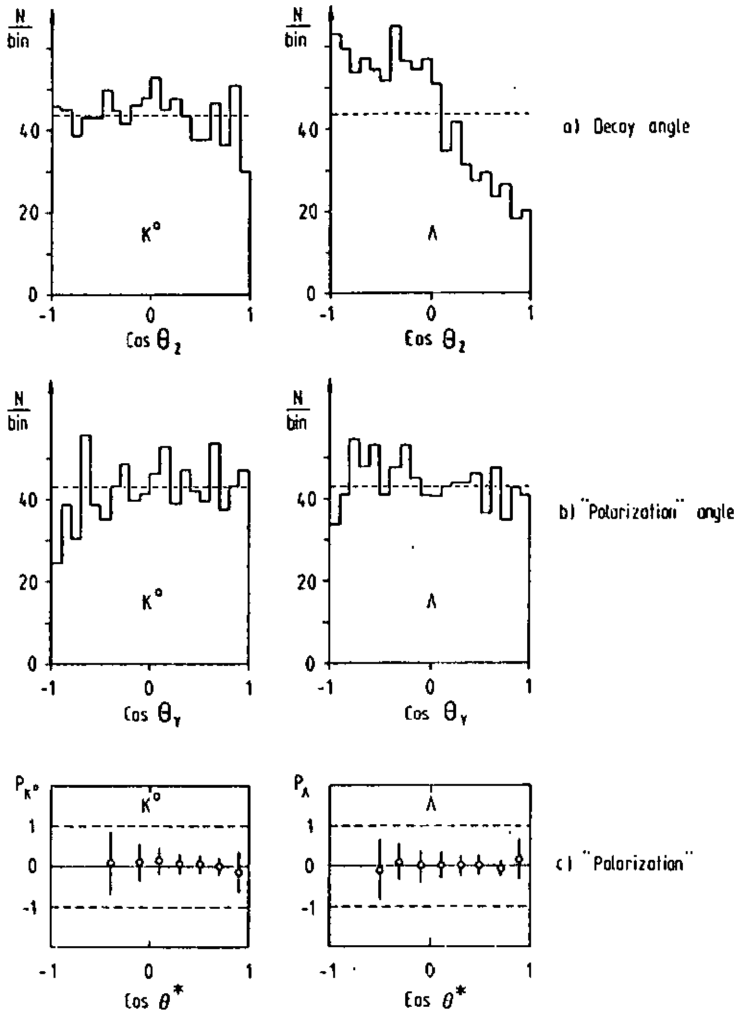

Fig. 5-9 : *Decay angle θ_z distribution (a), polarization angle θ_y distribution (b), and "polarization" (c) of K^0 and Λ particle in simulated events $\pi^- p \to K^0 \Lambda$.*

5.4 Comparison with Physical Results

One can test whether the Monte Carlo program is a realistic approximation of the behaviour of the spectrometer by comparing distributions from simulated events with those from physical results.

In fig. 5-10 (a), for example, we plotted the x-distribution of the main vertex for $\pi^- p \rightarrow K^0\Lambda$ and $K^0\Sigma^0$ events (full line) together with the distribution one would expect from the simulated event sample (dotted line). Obviously interactions occurring at the end of the target are most probably detected. The distribution as a function of ϕ_{yz} the azimuth angle of the scattering process in the yz-plane, is shown in fig. 5-10 (b) together with the Monte Carlo prediction. In both figures, the two curves coincide within statistical errors.

A test for the validity of the separation of V0 ambiguities is given in fig. 5-10 (c). Supposing the rest frame decay angle θ_z (see fig. 5-8 (b)) to be uniformly distributed in the neutral particle decay, then the transverse momentum distribution, in the rest frame or laboratory frame of the neutral particle, is given analytically by the following formula :

$$\frac{dN}{dp_{trans}} = \text{const}\cdot\frac{p_{trans}}{\sqrt{p_{cms}^2 - p_{trans}^2}} \qquad (5\text{-}4)$$

The momentum p_{cms} of the decay products in the strange particle's rest frame is well-known from the masses of the particles involved.

For a K^0 p_{cms} equals 206 MeV/c, while for a Λ or $\bar{\Lambda}$ it is 100 MeV/c.

The distribution is sharply peaked at the kinematic maximum, p_{cms}, and goes to zero at $p_{trans} = 0$. The transverse momentum distribution for the "decay tracks" from gammas, however, peaks at zero and drops off sharply. This is due to the fact that the photon has zero mass and requires a recoil proton in order to convert to an electron pair.

Hence, contamination from gammas should give an additional peak at $p_{trans} = 0$ in the Λ transverse momentum distribution.

The dotted line in fig. 5-10 (c) was not obtained directly from eq. (5-4), but from the simulated event sample. From this figure, we are confident that the p_{trans} distributions behave as expected and that no ambiguities between Λ's and gammas have distorted the final $\pi^- p \to K^0\Lambda\,/\Sigma^0$ sample.

MEAN LIFE OF NEUTRAL PARTICLES

From simulated events, we can determine the efficiency of V0 reconstruction, ε_τ, as a function of the lifetime τ of a neutral particle.

The veto counters around the target will cancel all V0's which disintegrate within the first few cm's from the interaction point.

V0's with a larger decay length d_{lab} will more probably be detected.

The resulting detection efficiency ε_τ is plotted in fig. 5-11 (b) and fig. 5-12 (b) for the K^0 and Λ particle respectively at $p_{lab} = 3$ GeV/c. The lifetime τ in the neutral particle's rest frame is obtained by first calculating the decay time τ in the laboratory frame from the decay length d_{lab} and the neutral particle momentum, and secondly by transforming τ into the rest frame with :

$$\tau = \gamma \cdot t \qquad (5-5)$$

where γ is the Lorentz factor.

The distribution of the number of neutral particles as a function of was then normalized with the ε_τ distribution. The resulting normalized lifetime distribution dn/dt of K^0 and Λ particles is given, on a logarithmic scale, in fig. 5-11 (a) and fig. 5-12 (a), respectively.

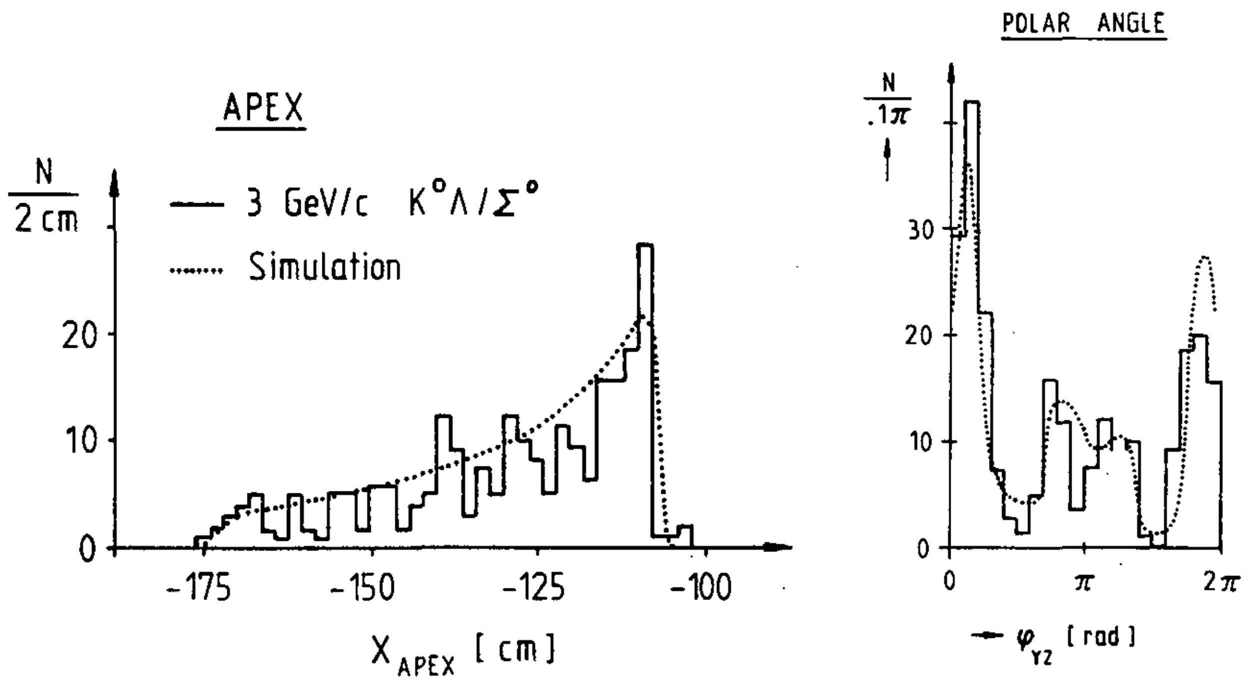

Fig. 5-10 : (a) X-coordinate distribution of apex in $\pi^- p \to K^0\Lambda/\Sigma^0$ events at 3 GeV/c (dotted line from simulated events).

(b) ϕ_{YZ}-distribution for the $K^0\Lambda/\Sigma^0$ final state at 3 GeV/c (dotted line from Monte Carlo simulation).

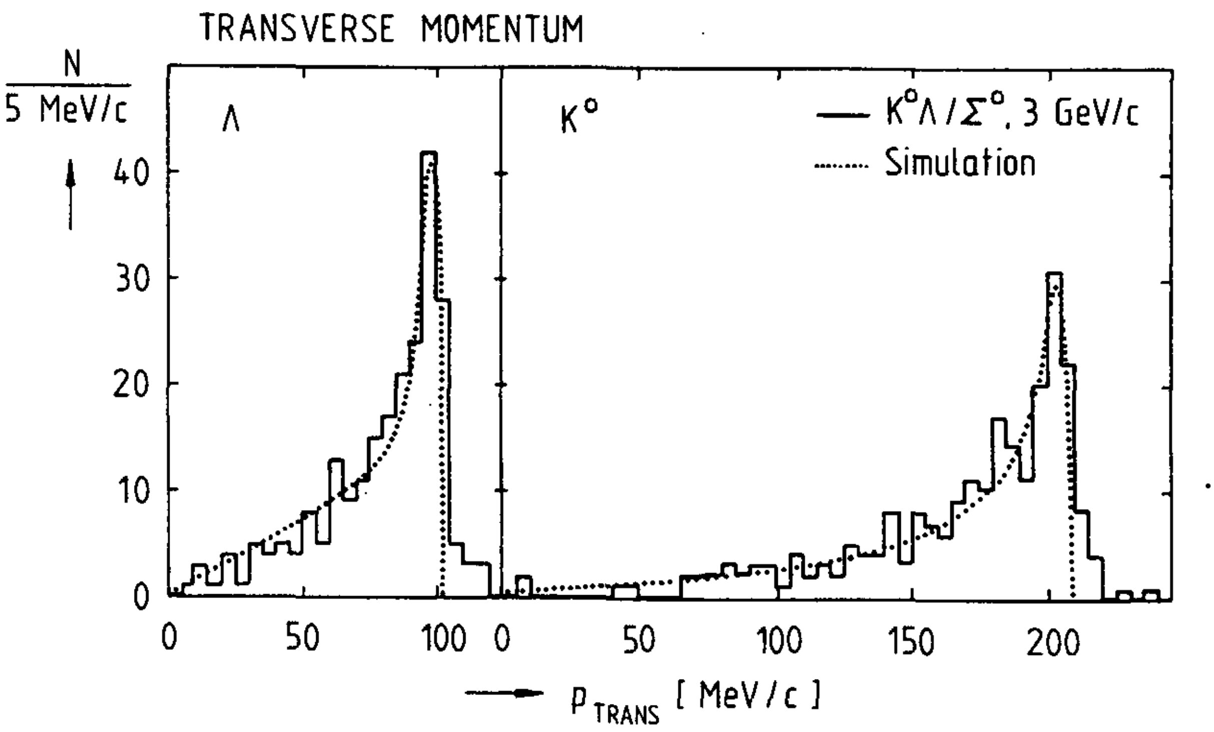

Fig. 5-10 (cont.) : (c) Transverse momentum distribution for Λ and K^0 decays in $\pi^- p \to K^0\Lambda/\Sigma^0$ at 3 GeV/c (dotted line from simulated events).

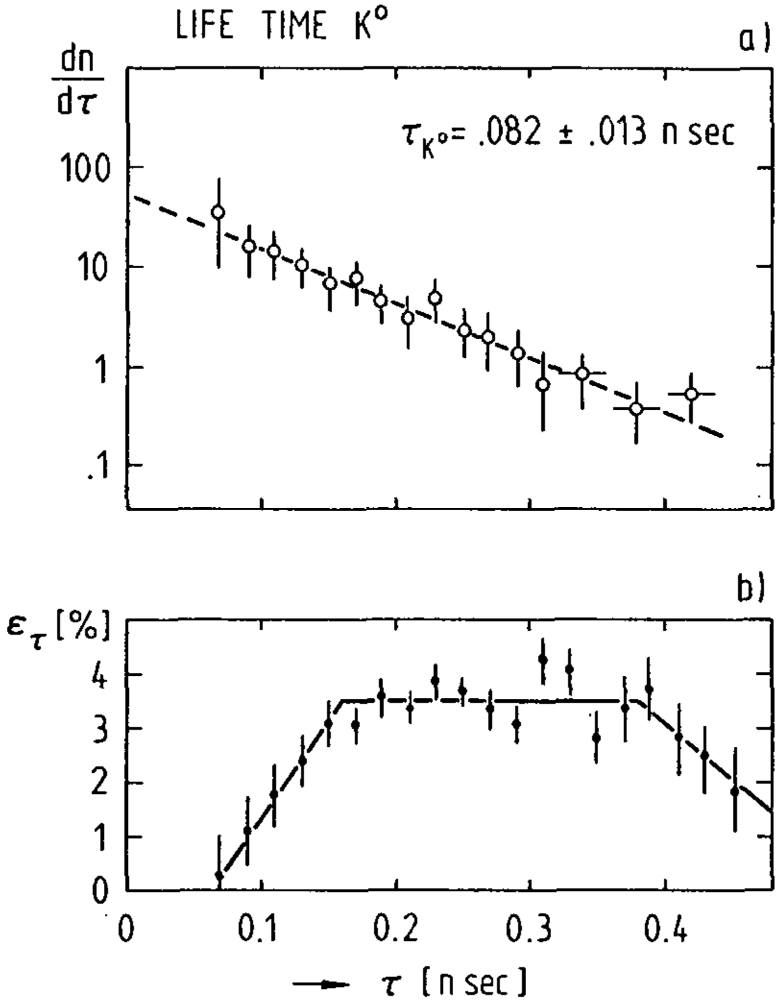

Fig. 5-11 : *Weighted K^0 life time distribution (a) in $\pi^- p \rightarrow K^0 \Lambda/\Sigma^0$ events using the efficiency ϵ_τ (b).*

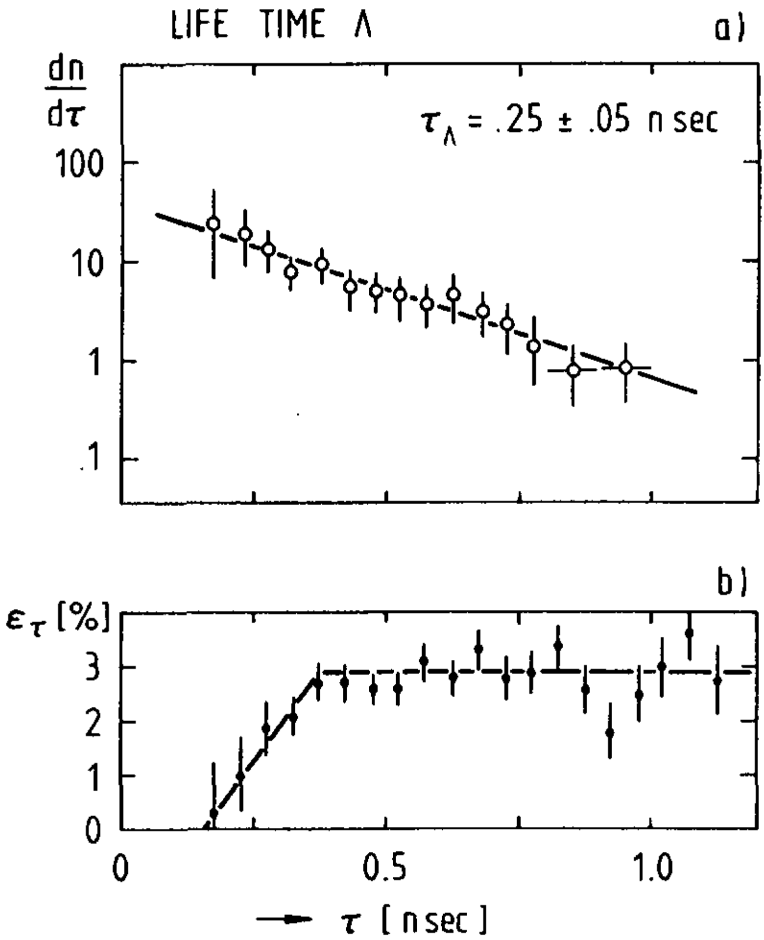

Fig. 5-12 : *Weighted Λ life time distribution (a) for $K^0\Lambda/\Sigma^0$ final states at 3 GeV/c, using the efficiency ϵ_τ (b).*

From the slope we deduced the experimental mean lifetimes :

$$\tau_{K^0} = (.82 \pm .13) * 10^{-10} \text{ sec}$$
$$\tau_{\Lambda} = (2.5 \pm 0.5) * 10^{-10} \text{ sec},$$

which is in good agreement with tabulated values from [REV80], namely

$$\tau_{K^0} = (.89 \pm .002) * 10^{-10} \text{ sec} \quad \text{and} \quad \tau_{\Lambda} = (2.63 \pm .02) * 10^{-10} \text{ sec}.$$

Our errors are quite large, though, due to limited statistics in the final event sample and in the deteroination of ε_{τ} from the Monte Carlo simulation.

5.5 Normalization Factors

The acceptance curves, together with some normalization factors which account for different inefficiencies and the visibility in neutral particle decays, will enable the calculation of the differential cross section $d\sigma/dt$ from the raw angular distributions presented at the end of chapter 4.

We defined $d\sigma/dt$ as follows :

$$\frac{d\sigma}{dt} = \frac{\Delta N}{\Delta t \cdot L \cdot \frac{A}{M} \cdot \rho_{H_2} \cdot N_{inc}} \cdot \frac{1}{\alpha(t)} \cdot f \qquad (5\text{-}6)$$

ΔN is the number of events found in the 4-momentum transfer interval Δt, L the target length (65 cm), A Avogadro's number, M = 2 for hydrogen molecules, ρ_{H_2} the liquid hydrogen density (.0708 g/cm^3), N_{inc} the total number of incident particles, $\alpha(t)$ tha total acceptance and f the product of various correction factors.

The c.m.s. scattering angle θ^* is related to the Mandelstam variable t by the relation :

$$t = (P_1 - P_3)^2 = 2p_1^* p_3^* \cos\theta^* + m_1^2 + m_3^2 - 2E_1^* E_3^* \qquad (5\text{-}7)$$

t is the 4-momentum transfer between particle 1 and 3 with 4-momentum P_1 and P_3 respectively, if we consider the reaction $1 + 2 \rightarrow 3 + 4$. $\vec{P}_1^*$, $\vec{P}_3^*$ and E_1^*, E_3^* are c.m.s. 3-momenta and energies, m_1, m_3 the masses of particles 1 and 3.

As we have seen in section 5.2, the acceptance for 2V0 events as a function of $\cos\theta^*$ contains one part, α_{geom}, determined by the Monte Carlo program and a second term, α_{rec}, which accounts for reconstruction inefficiencies of ROMEO. So, in eq. (5-6) we used :

$$\alpha(t) = \alpha_{geom}(t) * \alpha_{rec}(t). \qquad (5\text{-}8)$$

During the analysis of elastic reactions, a normalization factor $f_{el}\ (p_{lab}) = f1 \cdot f2 \cdot f3$ was determined at each beam momentum value. It accounts for [BIL82] :

. losses due to the varying liquid hydrogen level (f1),

. normalization runs at 3. - 3.3 GeV/c (f2),

. losses due to wrong beam particle identification (f3).

The resulting factor and its errors is listed in table 5-2 below.

Furthermore, visibility factors f_{vis} had to be introduced which account for neutral particle decay modes that could not be detected during this experiment. So the branching ratios of decays into charged particle final states are (64.2 + .05)% for $\Lambda \rightarrow p\pi^-$ and (68.61 + .24)% for $K^o \rightarrow \pi^+\pi^-$. In addition, 50% of the K^o's belong to the long-lived K_L^o which has a much longer mean life, $\tau_{K_L^o} = 580\ \tau_{K_S^o}$.

Another correction is due to losses when outgoing neutral particles undergo secondary interactions in the material inside or around the target (barrel counter, BC or cylindrical scintillator CYL). This contribution is also dependent on the scattering angle. In analogy to 2-prong correction factors, we used a factor $f_{int} = 1.20 \pm .12$.

Finally, a factor f_{rec} assured the correction for the reconstruction efficiency $\epsilon_{K^0\Lambda}$ and $\epsilon_{\bar{\Lambda}\Lambda}$ as was discussed in section 5.2. So, altogether, the factor f_{rec} in eq. (5-6) is the product :

$$f = f_{el} \cdot f_{vis} \cdot f_{int} \cdot f_{rec} \qquad (5\text{-}9)$$

A summary of the factors involved in the normalization of the raw angular distributions is given in tables 5-2 and 5-3 for incident π^- and $\bar{p}$-beam, respectively. (At 3. - 3.3 GeV/c beam momentum N_{inc} contains the number of incident particles of "normalization runs" only.)

p_{lab} (GeV/c)	N_{inc} ($*10^6$)	f_{el}	f_{vis}	f_{rec}
3.0	9.23	.118 ± .014	4.54 ± .02	2.08 ± .39
3.1	20.46	.063 ± .007		
3.2	41.86	.127 ± .013		
3.3	50.05	.374 ± .039	↓	↓
4.95	821.15	2.403 ± .137		
7.8	3955.	1.035 ± .159		
11.7	10209.	2.092 ± 1.453		

Table 5-2 : Normalization factors for π^- beam.

p_{lab} (GeV/c)	N_{inc} ($*10^6$)	f_{el}	f_{vis}	f_{rec}
3.0	2.19	.097 ± .015	2.426 ± .004	2.43 ± .71
3.1	3.60	.095 ± .014		
3.2	5.86	.129 ± .017		
3.3	5.40	.177 ± .026	↓	↓
4.95	∿ 18.25	2.403 ± .137		
7.8	3122.	1.015 ± .107		
11.7	11730.	2.561 ± .753		

Table 5-3 : Normalization factors for $\bar{p}$-beam.

Apart from statistical errors on the number of events in the raw angular distribution, it is the errors of the normalization factors which determine the precision of the final results. They are $\sim$ 20% for the $K^0\Lambda$ event sample and $\sim$ 29% for the $\bar{\Lambda}\Lambda$ final state.

Errors from the acceptance term in eq. (5-6) are usually much smaller, $\sim$ 4% in the large angle region. So these are small with respect to the statistical errors alone.

6. DIFFERENTIAL CROSS SECTION AND POLARIZATION

6. DIFFERENTIAL CROSS SECTION AND POLARIZATION

From the knowledge of the spectrometer acceptance and the normalization factors we can calculate the differential cross sections from the raw angular distributions of 2-V0 events. Including topology T1 events (1-V0) increases considerably the statistics, but normalization is only possible relative to the 2-V0 sample.

When extracting the polarization of hyperons, we have to consider the precession of the particle spin in a strong magnetic field.

6.1 Normalized Angular Distributions

6.1.1 $K^0\Lambda$ and $K^0\Sigma^0$ Final Stats

In this section, we shall combine the two channels

$$\pi^- p \longrightarrow K^0\Lambda^0 \tag{1a}$$

and

$$\pi^- p \longrightarrow K^0\Sigma^0 \tag{1b}$$

in order to reduce statistical errors. For the raw angular distributions of fig. 4-15, we have already indicated each contribution separately. It will become clear when discussing theoretical models that the shapes of the two resulting differential cross saction distributions are very similar. This is due to the similarities of Λ and Σ^0 particle properties. Both have strangeness $S = -1$, electric charge 0, spin $\frac{1}{2}$, and their mass difference is small. The Λ exists only as a neutral particle with isospin $I = 0$. The Σ^0, however, is a member of the isospin triplet Σ^-, Σ^0, Σ^+ with $I = 1$.

In the decay $\Sigma^0 \rightarrow \Lambda + \gamma$, the momentum of the decay products in the Σ^0's rest frame is only 74 MeV/c. So the influence of the missing γ in the total missing mass distribution (see definition in eq. (4-4)) with respect to the two detected V0's is only a broadening of the peak centered at zero. The result for the sum of 2-V0 candidates for reaction (1a) and (1b) is given in fig. 6-1.

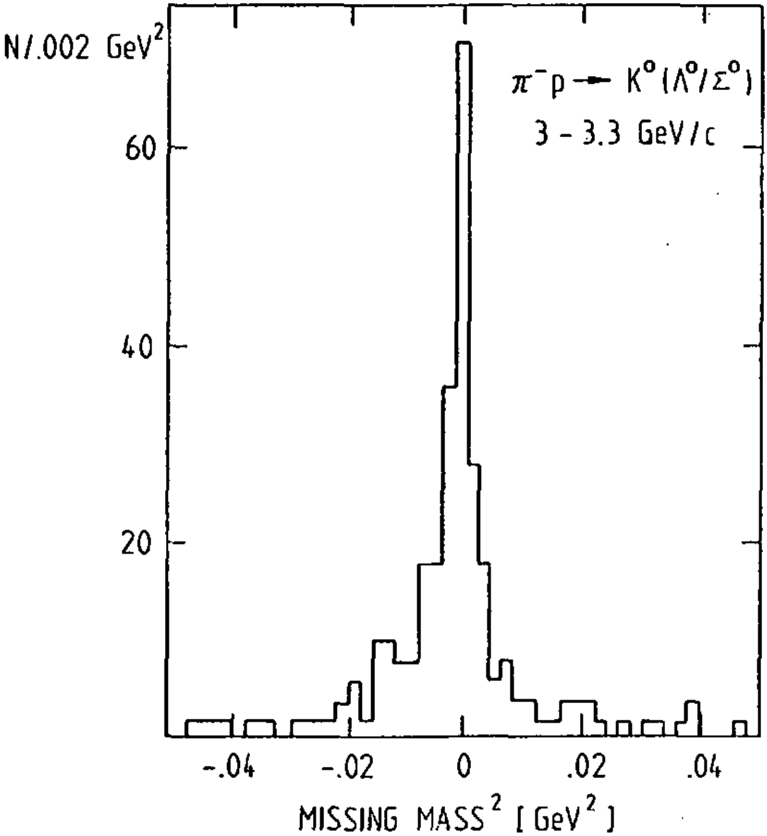

Fig. 6-1 : Total missing mass distribution for the $K^0\Lambda/\Sigma^0$ sample at 3 GeV/c.

If compared to the $K^0\Lambda$ final state, the momentum taken away by the γ in the $K^0\Sigma^0$ final state will introduce a broadening also for the missing momentum distributions. In addition, for the x-component (beam direction) an asymmetry appears at small positive values. The distributions for all three components for the final $K^0\Lambda/\Sigma^0$ sample is given in fig. 6-2.

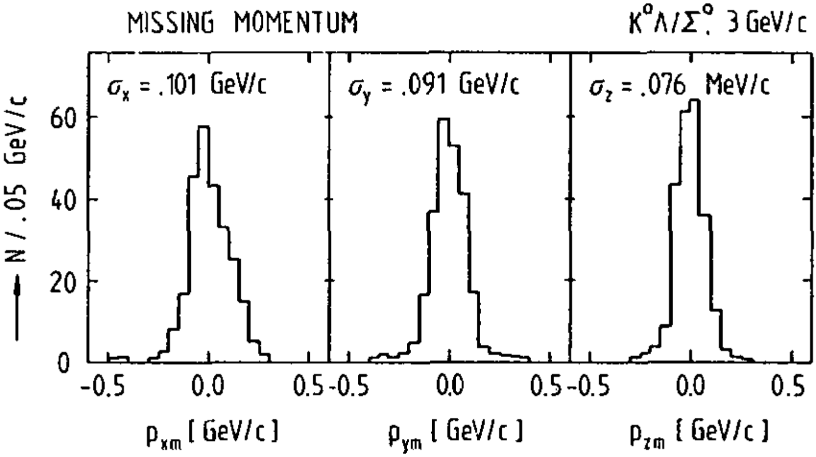

Fig. 6-2 : Distributions for the three components of the missing momentum in $\pi^- p \rightarrow K^0\Lambda/\Sigma^0$ at 3 GeV/c.

The differential cross section $d\sigma/dt$ for the sum of the reaction channels $\pi^- p \rightarrow K^0\Lambda$ and $\pi^- p \rightarrow K^0\Sigma^0$ is given in fig. 6-3 as a function of the c.m.s. scattering angle θ^*, summarizing all WA13 2-V0 data for these channels.

Errors are relatively large for $\cos\theta^* > .8$ where the acceptance becomes very small. At large angles and at high beam momenta, we have regrouped bins with low contents. Altogether, the values of $d\sigma/dt$ cover a range of about 4 orders of magnitude.

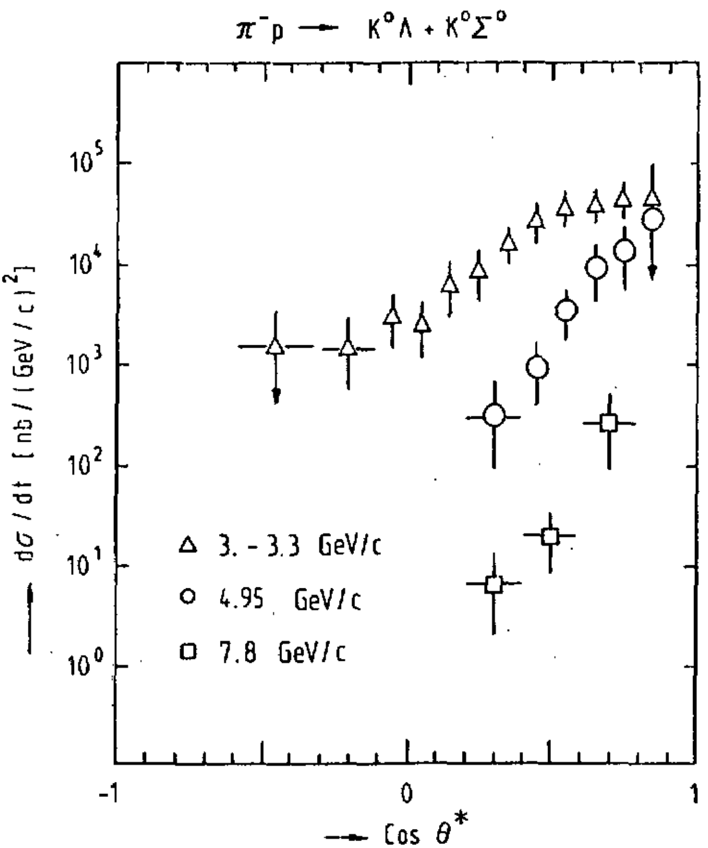

Fig. 6-3 : *WA13 results for the differential cross section in $\pi^- p \rightarrow K^0\Lambda/\Sigma^0$. Only 2V0 event topology is considered.*

6.1.2 $\bar{\Lambda}\Lambda$ and $\bar{\Lambda}\Sigma^0$ + c.c. Final States

We analyze simultaneously the auto-conjugate reaction

$$\bar{p}p \longrightarrow \bar{\Lambda}\Lambda \tag{2a}$$

and the conjugate reactions

$$\bar{p}p \longrightarrow \bar{\Lambda}\Sigma^0 + \bar{\Sigma}^0\Lambda \tag{2b}$$

As an example, the total missing mass distributions at 7.8 GeV/c for <u>all 2-V0 candidates</u> for these reactions is given in fig. 6-4 (b), whereas fig. 6-4 (a) contains candidates for reaction (1a) and (1b) discussed in the previous subsection.

Compared to data at lower beam momenta, the widths of these distributions have increased. This reflects the fact that at higher energies, reaction ambiguities occurred more frequently and the uncertainties during separation increased accordingly.

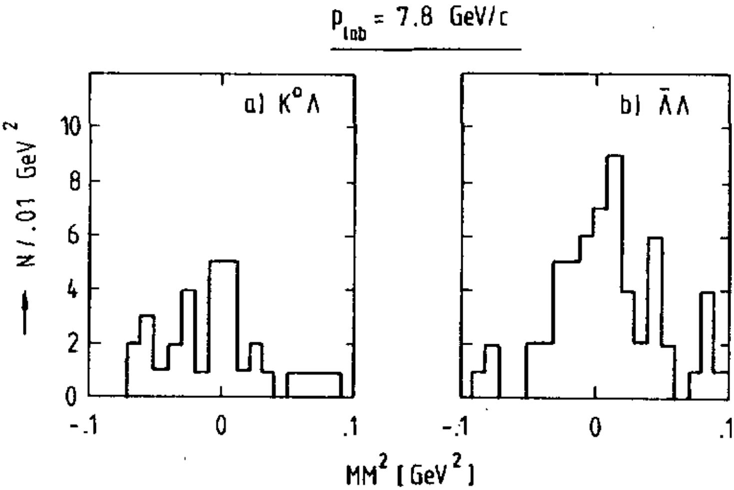

Fig. 6-4 : Total missing mass distributions from candidates to (a) the $K^0\Lambda$ and (b) the $\bar{\Lambda}\Lambda$ final state at 7.8 GeV/c.

In fig. 6-5 (a), we summarize the differential cross sections for $\bar{\Lambda}\Lambda$, $\bar{\Lambda}\Sigma^0$ and $\bar{\Sigma}^0\Lambda$ final states at incident beam momenta around 3 GeV/c, 7.8 GeV/c and 11.7 GeV/c. In order to illustrate the $|t|$-range that was covered at these energies, we plotted the same data in fig. 6-5 (b) as a function of $-t' = -(t - t_{min})$, where t_{min} is the lower kinematical limit of the 4-momentum transfer.

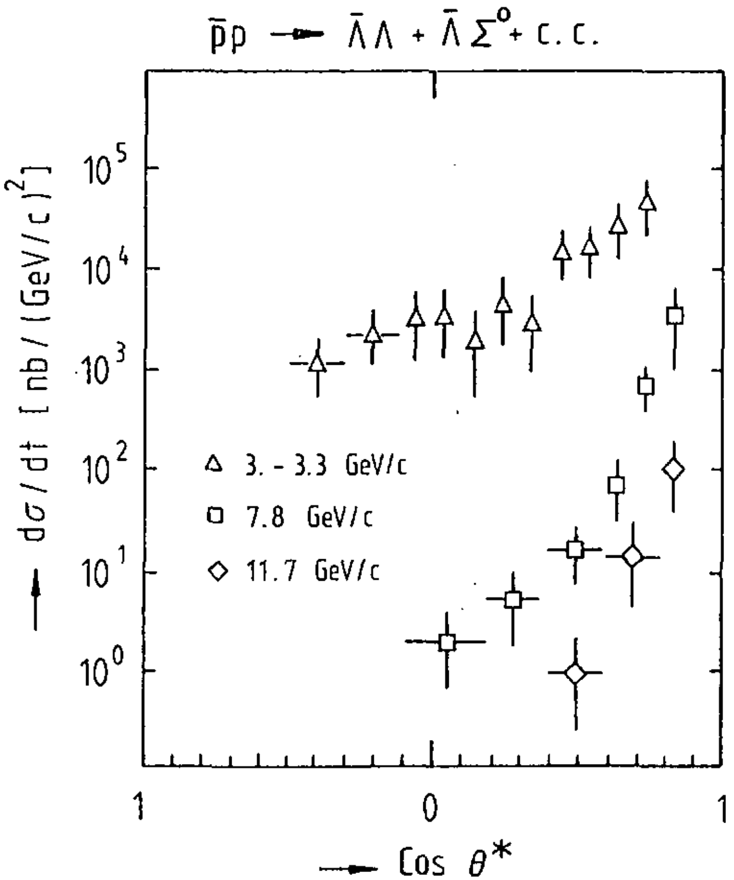

Fig. 6-5 : (a) *Differential cross section distributions at different WA13 beam momenta for the 2V0 event sample of the $\bar{p}p \rightarrow \bar{\Lambda}\Lambda + \bar{\Lambda}\Sigma^0$ + c.c. reaction channel.*

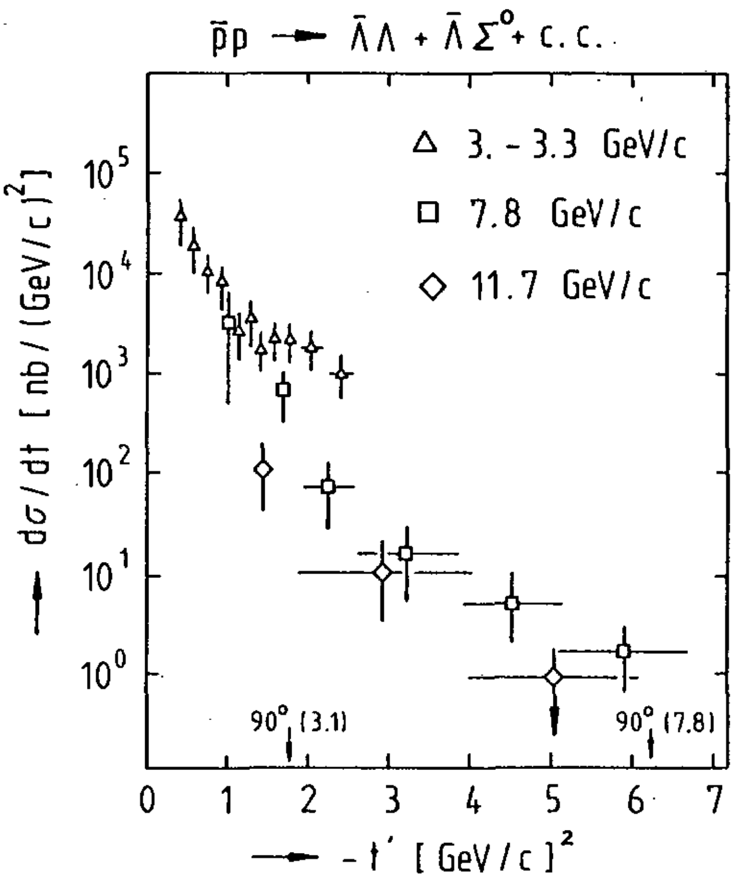

<u>*Fig. 6-5*</u> *(cont.) : (b) Differential cross sections as a function of momentum transfer $-t'$ for $\bar{p}p \rightarrow \bar{\Lambda}\Lambda + \bar{\Lambda}\Sigma^{0}$ + c.c.*

6.1.3 Reactions with Missing π^0

Though it was not the aim of this experiment to study final states that include neutral pions, we normalized a small sample of this category that we obtained after separation of ambiguities between a missing γ or a missing π^0 particle.

As was pointed out in chapter 4, the reaction $\pi^- p \rightarrow K^0 \Lambda (\pi^0)$ has important resonances, such as $K^{*0}(892)$ and $\Sigma^{*0}(1385)$. At $p_{lab} = 3$ GeV/c, for example, the total cross sections for the final states $K^{*0}\Lambda$ and $K^0\Sigma^{*0}$ are (63 ± 6) mb and (29 ± 7) mb respectively, according to [BER79].

From the effective mass plots $M^2_{eff}(K^0\pi^0)$ and $M^2_{eff}(\Lambda\pi^0)$ in fig. 4-13, we estimate contributions from approximately 16 ± 5 $K^{*0}(892)$ and 10 ± 3 Σ^{*0} (1385) within the originally reconstructed 92 candidates for the $K^0\Lambda(\pi^0)$ hypothesis (see table 4-3). Some of these candidates were attributed to the K^0 Σ^0 sample. In order to reduce the background signal, we introduced a cut in the total missing mass $|MM^2(K^0\Lambda) - .018| < .014$ GeV^2 and obtained finally 43 events. The normalization procedure resulted in the differential cross section distribution of fig. 6-6.

Compared to the $\pi^- p \rightarrow K^0 \Lambda$ reaction, the acceptance for $K^0 \Lambda$ (π^0) final states is much smaller. The differential cross sections, however, are of the same order of magnitude around 90^0 c.m.s.

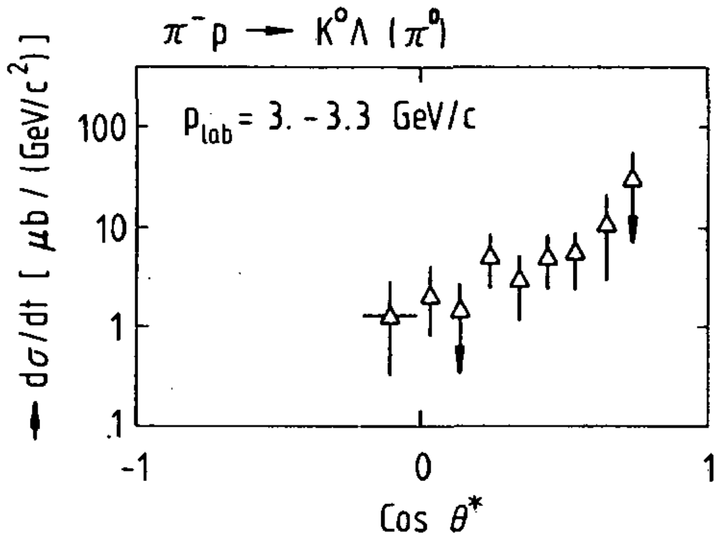

Fig. 6-6 : Differential cross section of $K^0\Lambda$ final state with missing neutral pion at 3 GeV/c.

6.2 Differential Cross Sections at Large Angles

From a theoretical point of view, it would be convenient to have results at the largest possible p_T values at each energy, that is at 90^0 c.m.s. scattering angle. For the K^0 Λ/Σ^0 final states, though, data points from 2-V0 events exist only down to $\cos\theta^* = .3$ ($\theta^* = 73^0$), as was shown in fig. 6-3. An extrapolation to 90^0 would require an assumption on the shape of the angular distributions. This will be possible once we have looked into some theoretical models. At this stage of the analysis, we only want to exploit experimental data.

So in fig. 6-7 we plotted the values of the differential cross section at $\theta^* = 73^0$ for the channel $\pi^- p \rightarrow K^0 \Lambda/\Sigma^0$ and $\bar{p}\ p \rightarrow \bar{\Lambda}\Lambda + \bar{\Lambda}\ \Sigma^0$ + c.c. One should note that one of the two references, [JAY77], does not include final states where Σ^0 or $\bar{\Sigma}^0$ particles are present. In addition, in this case the beam momentum already approaches the threshold region where the total cross section drops off sharply.

The straight line in fig. 6-7 not only guides the eye, but follows the suggestion made in the introduction that the differential cross section at fixed angle follows a power law s^{-n}. We shall discuss theoretical predictions for n in the next chapter.

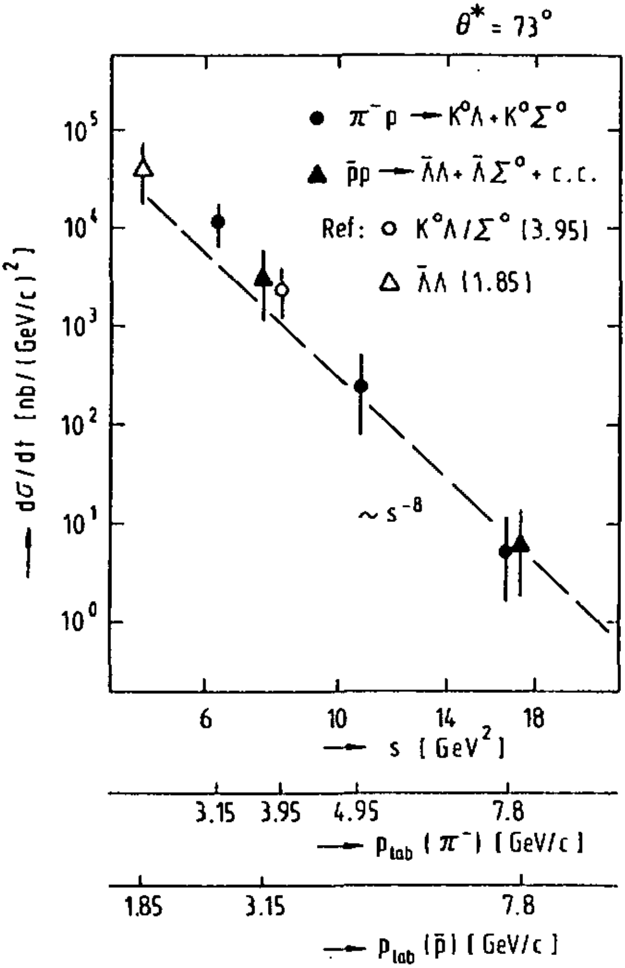

<u>*Fig. 6-7*</u> : *Large angle differential cross section at θ* = 73° from WA13 data at 3 GeV/c, 4.95 GeV/c and 7.8 GeV/c, and from ref. [LOV80] at 3.95 GeV/c and [JAY77] at 1.85 GeV/c. The dashed line indicates the quark counting law prediction.*

6.3 Polarization Data

At some beam momenta, the number of events is sufficiently high to take advantage of the analyzing power of the weak Λ and $\bar{\Lambda}$ decay for the determination of hyperon polarization.

In the following sections we use the term "inclusive" for events where at least one hyperon was reconstructed. "Exclusive", as usual, concerns events for which both final state neutral particles are known.

6.3.1 Definitions

In the hyperon rest frame, the 3 components of the polarization vector $\vec{P} = (P_x, P_y, P_z)$ are defined by

$$P_i = \frac{1}{s} \langle m_i \rangle \; , \qquad i = x,y,z \tag{6-1}$$

where s is the hyperon spin and m_i denotes the spin component with respect to the axis i. The definition of the coordinate system associated to the hyperon rest frame was shown in fig. 5-8.

In the case of two particles with spin s, one defines the spin correlations

$$C_{ij} = \frac{1}{s^2} \langle m_{1,i} \cdot m_{2,j} \rangle \tag{6-2}$$

When measuring experimentally the polarization of the Λ particle, say, one has to analyze the decay distribution in the hyperon rest frame given by (see also section 7.1.3) :

$$\frac{d\sigma}{d\Omega_\Lambda} \sim \frac{1}{4\pi} \left(1 + \alpha_\Lambda \, \vec{P}_\Lambda \cdot \hat{p}\right) \tag{6-3}$$

where $\hat{p}$ is the unit vector parallel to the momentum of the decay proton. α_Λ is the asymmetry parameter in the weak decay process. Employing the moment method, one obtains the polarization components

$$\boxed{P_{\Lambda,i} = \frac{3}{\alpha_\Lambda} \langle\cos\theta_i\rangle} \tag{6-4a}$$

An estimate of the error is given by

$$\sigma(P_{\Lambda,i}) = \frac{3}{\alpha_\Lambda} \sqrt{\langle\cos^2\theta_i\rangle - \langle\cos\theta_i\rangle^2} \tag{6-4b}$$

$$\approx \frac{1}{\alpha_\Lambda} \sqrt{\frac{3}{N_\Lambda}}$$

The $\bar{\Lambda}$ polarization is obtained correspondingly.

If acceptance effects cause anisotropy in the detection probability as a function of $\cos\theta_i$, weights $w_i(\cos\theta_i)$ have to ba introduced accordingly :

$$P_{\Lambda,i} = \frac{3}{\alpha_\Lambda} \frac{\int_{-1}^{1} w_i(\cos\theta_i)\ \cos\theta_i\ d\cos\theta_i}{\int_{-1}^{1} w_i(\cos\theta_i)\ d\cos\theta_i} \tag{6-5}$$

For a $\bar{\Lambda}\Lambda$ final state we have to consider the joint decay distribution :

$$\frac{d^3\sigma}{d\Omega\, d\Omega_\Lambda d\Omega_{\bar{\Lambda}}} = \frac{1}{(4\pi)^2}\, I_o\ (\theta^*)\ \Big(1 + \alpha_\Lambda\, \vec{P}_\Lambda \cdot \hat{p}_p + \alpha_{\bar{\Lambda}}\, \vec{P}_{\bar{\Lambda}} \cdot \hat{p}_{\bar{p}} \tag{6-6}$$

$$+ \alpha_\Lambda\, \alpha_{\bar{\Lambda}} \sum_{i,j} C_{ij} \cos\theta_{\Lambda,i} \cdot \cos\theta_{\bar{\Lambda},j}\Big)$$

where $I_0(\theta^*)$ is the measured differential cross section, $d\Omega_\Lambda$ and $d\Omega_{\bar{\Lambda}}$ are the solid angles in the decay $\Lambda \to \pi^- p$ and $\bar{\Lambda} \to \bar{p}\pi^+$ respectively. From CP invariance, one obtains [REV80]

$$\alpha_\Lambda = -\alpha_{\bar{\Lambda}} = .642 \pm .013$$

Again by integration we get the spin correlations from eq. (6-6)

$$\boxed{C_{ij} = \frac{9}{\alpha_\Lambda \alpha_{\bar{\Lambda}}} \langle \cos\theta_{\Lambda,i} \cdot \cos\theta_{\bar{\Lambda},j} \rangle} \tag{6-7a}$$

The error estimates are :

$$\sigma(C_{ij}) = \frac{3}{\alpha_\Lambda^2} \quad \frac{1}{N_{\bar{\Lambda}\Lambda}} \tag{6-7b}$$

Low statistics are a severe handicap as far as spin correlations are concerned. Based on our final $\bar{\Lambda}\Lambda$ sample, $\sigma(C_{ij}) \approx 1.1$.

PRECESSION

If a particle carries a magnetic moment associated to its spin, it will undergo some precession during its lifetime in the magnetic field. We have calculated the corresponding correction in spin orientation (see Appendix A.2). The angle $\Delta\varepsilon$ between the spin direction before and after precession in the hyperon rest frame is essentially determined by

$$\Delta\varepsilon \sim g \ \mu_N \ H^* \tag{6-8}$$

where the Landé factor $g = -0.67$ for the Λ particle, μ_N is the nuclear magneton, H^* is the detector magnet field transformed into the hyperon rest frame.

As is shown in fig. 6-8 at $p_{lab} = 3.-3.3$ GeV/c, the correction due to precession which we had to apply prior to the calculation of polarization angles varies between 0^0 and 4^0 with a mean value of about 0.7^0. Even at $p_{lab} = 7.8$ GeV/c the corrections were relatively small ($\overline{\Delta\varepsilon} \approx 1.1$).

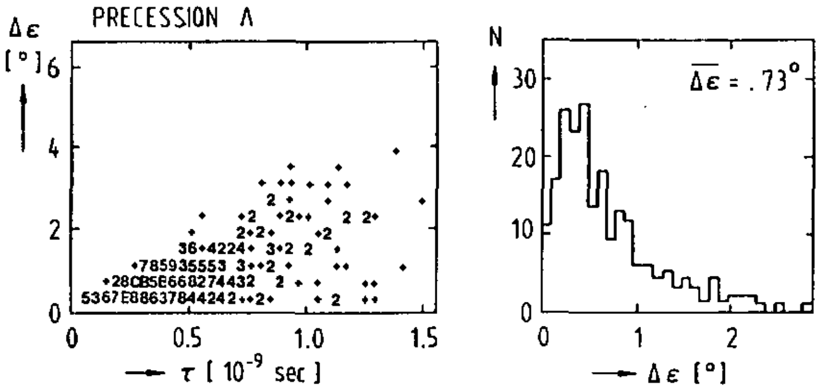

<u>*Fig. 6-8*</u> : *Precession of* Λ *particle at* p_{lab} *around 3 GeV/c.*

(a) Change of spin direction Δε *versus life time* τ.
(b) Δε *distribution.*

6.3.2 Results

A striking result is the strong negative Λ polarization found in the reaction $\pi^- p \rightarrow K^0 \Lambda/\Sigma^0$ (cf. BEL81). The angular distribution in $\cos\theta_{\Lambda,y}$, where $\theta_{\Lambda,y}$ is the angle of the momentum of the decay proton and the normal to the production plane (see fig. 5-8) is shown in fig. 6-9 for p_{lab} around 3 GeV/c.

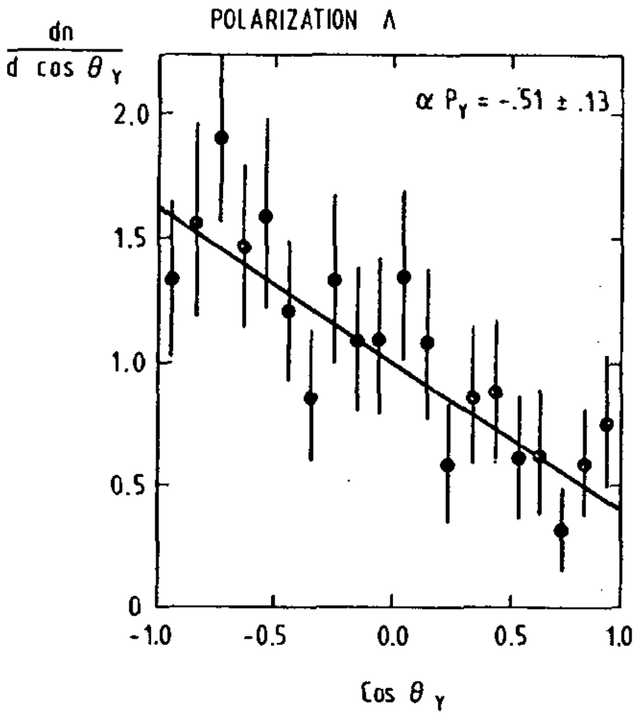

Fig. 6-9 : Polarization angle distribution for the Λ particle in the $K^0\Lambda/\Sigma^0$ event sample at 3 GeV/c. The straight line results from a least square fit of the parameter αP.

The straight line fitted to the data has a slope of $\alpha_\Lambda P = -.51 \pm .13$, with a reduced χ^2 value of 0.84, hence the average polarization is

$$\boxed{\bar{P}_{\Lambda,y} = -.79 \pm .17}$$

For the $K^0\Lambda$ final atate events alone we found :

$$\boxed{\bar{P}_{\Lambda,y} = -1.03 \pm .23}$$

A number of collaborations have measured the Λ polarization in the reaction $\pi^- p \to K^0\Lambda$. We plot published data from some experiments (ABR71 at 3.9 GeV/c, BEU70 at 4.0 GeV/c, BEU75 and AST75 at 5.0 GeV/c) in fig. 6-10 (a) between 3 and 4 GeV/c and in fig. 6-10 (b) around 5 GeV/c. Our data points include the $K^0\Lambda$ and $K^0\Sigma^0$ sample.

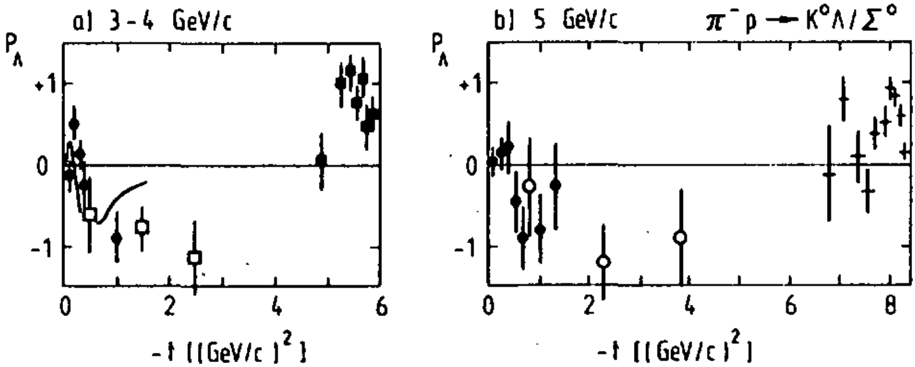

Fig. 6-10 : Λ polarization data from WA13 (a) at 3 GeV/c (ref. [ABR71] at 3.9 GeV/c and ref. [BEU70] at 4 GeV/c) and (b) at 4.95 GeV/c (ref. [BEU75] and ref. [AST75] both at 5 GeV/c). The full line in (a) indicates a Regge model prediction [NAV76].

Both plots are characterized by a Λ polarization which starts around 0 in the forward direction, going to negative values at increasing $|t|$ values. Our data completes published small-angle data. In the backward direction (that is, when Λ's are produced in the forward direction) the polarization becomes strongly positive before coming back to zero at the kinematical limit.

As a test of the analyzing program, we have determined the K^0 "polarization". It is, in fact, vanishing as is shown in fig. 6-11 (b). This figure and all other parts of fig. 6-11 show "inclusive" polarization data, i.e. all events are considered where at least the particle considered was properly reconstructed.

Fig. 6-12 gives a summary of inclusive Λ polarization at all beam momenta as a function of squared momentum transfer t.

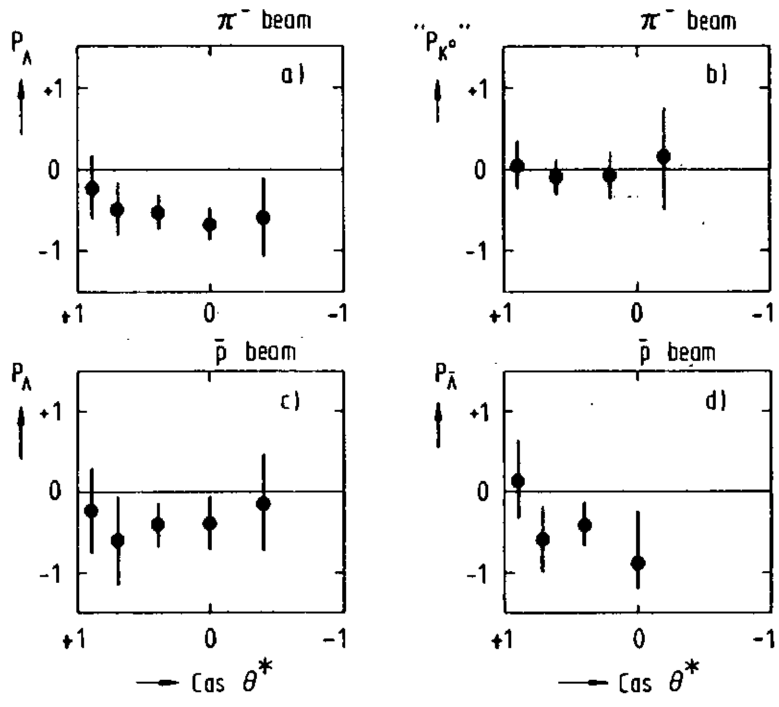

Fig. 6-11 : *Λ polarization at p_{lab} around 3 GeV/c in the π^- beam (a) and $\bar{p}$ beam (c). The "K^0 polarization" is checked in (b). The $\bar{\Lambda}$ polarization is shown in (d).*

In order to show the p_T-range covered in our data we have plotted in fig. 6-13(a) the inclusive Λ polarization in the π^--beam and in fig. 6-13(b) the inclusive Λ and $\bar{\Lambda}$ polarization in the $\bar{p}$-beam. Compared to exclusive data the inclusive hyperon polarization is smaller but still negative for p_T-values above 0.4 GeV/c.

Finally, in the exclusive process $\bar{p}p \to \bar{\Lambda}\Lambda/\Sigma^0$ at 3. - 3.3 GeV/c the combined Λ and $\bar{\Lambda}$ mean polarization around $-t = 1.25\ (\mathrm{GeV/c})^2$ was

$$\boxed{\bar{P}_{\bar{\Lambda}\Lambda,y} = -.60 \pm .38}$$

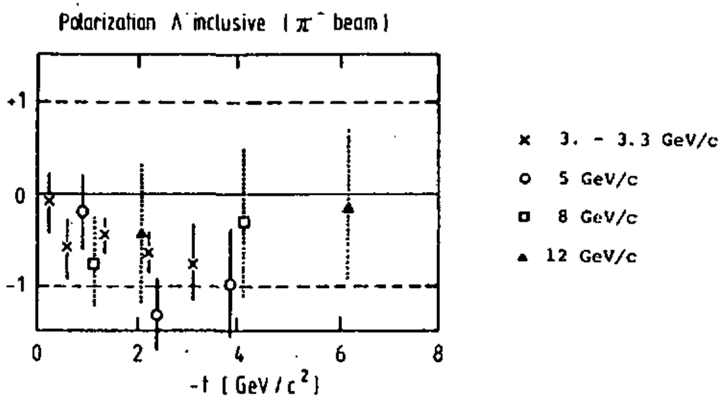

Fig. 6-12 : *"Inclusive" Λ polarization as a function of $-t$ for different WA13 beam momenta.*

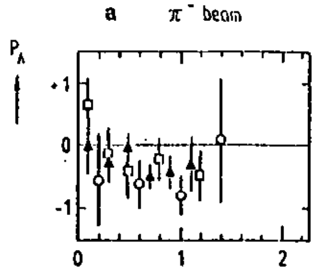

p_{inc} [GeV/c]		π^- beam nb. of Λ	$\bar{p}$ beam nb. of Λ	$\bar{\Lambda}$
▲	3	736	201	187
○	5	121	-	-
□	6	232	272	667
◆	12	-	409	634

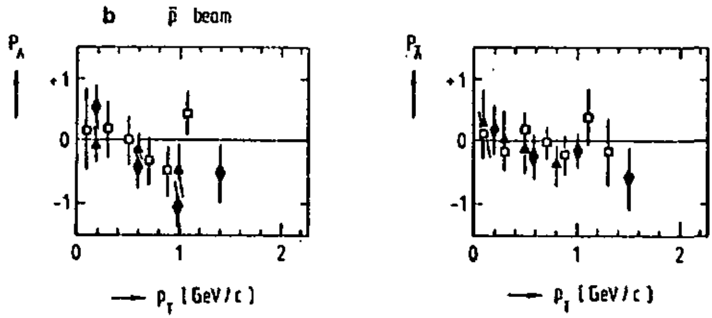

<u>*Fig. 6-13*</u> : *"Inclusive" Λ and $\bar{\Lambda}$ polarization as a function of transverse momentum in*

(a) $\pi^- p \to \Lambda$ + neutrals,

(b) $\bar{p}p \to \Lambda$ + neutrals and $\bar{p}p \to \bar{\Lambda}$ + neutrals,

at beam momenta between 3 and 12 GeV/c.

7. THEORETICAL MODELS

7. THEORETICAL MODELS

In this chapter, we first want to supply a general framework for the description of the experimental results. Then, we shall briefly describe the essential features of specific models and compare, as far as possible, their predictions with our results. In addition, data from other experiments will be considered in some reactions.

Since we deal with processes involving half integer spin particles, the helicity amplitude formalism represents a convenient way to describe the differential cross section and the polarization data. Helicity amplitudes were originally introduced by Jacob and Wick [JAC59]. The closely related concept of spin density matrices is based on a paper by Durand and Sandweiss [DUR64]. A general introduction into the field of polarization and an extensive review of the experimental situation can be found in a recent report by Bourrely et al. [BOU80].

In general, the interpretation of experimental results can be done in a model independent or in a model dependent way. In the first case one could, for example, test simple parametrizations of the amplitude, as was done in ref. [ATH74] for $\bar{p}p \rightarrow \bar{\Lambda}\Lambda$. The decomposition into partial wave amplitudes would be a second example.

To do this, we need to have an idea about the magnitude and the ahepe of the forward peak of the angular distribution. This region, however, was suppressed by the trigger lay-out of the WA13 experiment. So for the discussion of models which typically account for the behaviour at low energies and small transverse momentum values, we have to take into account results from other experiments, mostly bubble chamber data.

Usually, low energy models deal with the "macroscopic" picture of elementary particles. For example, the analysis of a diffraction pattern can give information about the size of particles. In the case of Regge models, which we shall discuss later on, one makes the assumption that the interaction proceeds via exchange of particles associated to Regge "trajectories". Only quantum numbers which characterize the interacting particles as a whole are crucial in the choice of the exchanged trajectory.

Models making assumptions about the internal "microscopic" structure of particles will be more appropriate to investigate the large angle domain. Some models try to avoid to specify too closely the nature of the internal constituents or partons of elementary particles. A prediction for the energy dependence of the differential cross section at large angles that depends only on the number of constituents inside the reacting particles was derived by Matveev et al. [MAT73] and is known as the dimensional counting rule.

Another candidate, the constituent interchange model (CIM) assumes baryons to contain a constituent-core pair [GUN73]. In other words, the baryon is described by a quark that takes part in the interaction and a spectator diquark core. It is suggested that no QCD-like hard scattering subprocess between constituents occurs. So all contributions to the amplitude are easily determined from the quark quantum numbers that can be exchanged.

The massive quark model (MQM) introduced by Preparata [PRE73] assumes a subprocess between quarks which is Regge behaved. The nature of the interacting quarks determines all possible exchanges of meson and baryon trajectories in the subprocess.

In a first step, all models have to define how to choose the interacting constituents. For example, the CIM model exploits the electromagnetic form factor of mesons and baryons as measured in e-p interactions. In a second step, one has to define the interaction mechanism between constituents. It is here that the most important differences between models show up.

7.1 Helicity Amplitude Formalism

Helicity amplitudes supply a model independent expression for the differential cross section in reactions where spin is involved. Initial and final states are defined by their spin density matrices which can be expressed in terms of polarization and spin correlation. Symmetry considerations considerably restrict the number of helicity amplitudes and impose conditions on the observables that should be satisfied in every experiment.

7.1.1 Model Independent Cross Section

In general, the differential cross section (denoted by d.c.s. hereafter) and the scattering amplitude $f(E,\theta)$ as a function of energy $E = \sqrt{s}$ and c.m.s. scattering angle θ, for the process

$$a + b \longrightarrow c + d$$

are related by

$$\frac{d\sigma}{d\Omega} = \frac{p_c}{p_a} \left| f(E,\theta) \right|^2 \tag{7-1}$$

where p_a and p_c are initial and final state c.m.s. momenta.

Commonly, the Lorentz invariant amplitude

$$F(s,t) = 8\pi \sqrt{s}\, f(E,\theta)$$

is used. So we get for the d.c.s.

$$\frac{d\sigma}{d\Omega} = \frac{p_c}{64\pi^2 s\, p_a} \left| F(s,t) \right|^2 \tag{7-2}$$

We use the invariant Mandelstam variables defined by

$$s = (P_a + P_b)^2 \tag{7-3}$$
$$t = (P_a - P_c)^2$$
$$u = (P_a - P_d)^2$$

where P_i, $i = a,b,c,d$ are the four-vectors of the interacting particles. Expressing the d.c.s. with respect to the variable t, we get

$$\boxed{\frac{d\sigma}{dt} = \frac{1}{64\pi s\, p_a^2}\,|F(s,t)|^2} \tag{7-4}$$

At high energies ($s \gg m$), one obtains approximately $s \doteq 4\,p_a^2$, thus

$$\frac{d\sigma}{dt} = \frac{1}{16\pi s^2}\,|F(s,t)|^2 \tag{7-5}$$

As far as spin is concerned, the two types of reaction we are interested in are

$$0 \; + \; 1/2 \; \longrightarrow \; 0 \; + \; 1/2 \tag{7-6}$$

and

$$1/2 \; + \; 1/2 \; \longrightarrow \; 1/2 \; + \; 1/2 \tag{7-7}$$

In this chapter, we shall mainly deal with the more complex second case, where each spin state gives a contribution to the d.c.s., according to eq. (7-4). So, a priori, we have to determine 16 independent scattering amplitudes.

HELICITY

A useful definition of spin states is given by the helicity λ of a particle with spin s. The helicity is defined as the projection of the spin vector $\vec{s}$ on to the particle momentum $\vec{p}$

$$\lambda = \frac{\vec{s} \cdot \vec{p}}{|\vec{p}|} \qquad (7\text{-}8)$$

This definition has the following characteristics :

a) For mass $m \neq 0$, there are $2s+1$ helicity states $\lambda = s, s-1, \ldots, -s$. If $m = 0$, like for the photon with $s = 1$, there are only two values $\lambda = \pm s$.

b) Rotations in space (x,y,z) change the direction of $\vec{p}$, but λ remaining unchanged. Under space reflection λ changes sign.

c) When a Lorentz transformation in the direction of $\vec{p}$ is applied, one obtains a state with the same (or opposite) direction but a different magnitude of $\vec{p}$. If $\vec{p}$ is not reversed, again λ remains unchanged.

In order to illustrate the definition of helicity, we list the four possible initial and final spin configurations in reaction (7-7) with obvious ket notations :

initial state

$|++\rangle$
$|+-\rangle$
$|-+\rangle$
$|--\rangle$

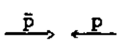

final state

$|++\rangle$
$|+-\rangle$
$|-+\rangle$
$|--\rangle$

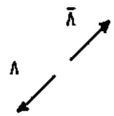

Following [JAC59], the probability of the transition from an initial helicity state $\lambda_a\lambda_b$ to a final state $\lambda_c\lambda_d$ is measured by the helicity amplitude defined as

$$f_{\lambda_c\lambda_d;\,\lambda_a\lambda_b}(\theta,\phi) = \frac{1}{p_a} \sum_J (J + \tfrac{1}{2}) \langle\lambda_c\lambda_d\,|\hat{T}^J(E)|\lambda_a\lambda_b\rangle \qquad (7\text{-}9)$$

$$\cdot\ e^{i(\lambda-\mu)\phi}\, d^J_{\lambda\mu}(\theta).$$

where $\lambda = \lambda_a - \lambda_b$, $\mu = \lambda_c - \lambda_d$, J = total angular momentum, and $\hat{S} = 1 + i\hat{T}$. The functions $d^J_{\lambda\mu}(\theta)$ define rotations and can be found, for example, in ref. [JAC59].

Thus, we are able to express the d.c.s. in terms of helicity amplitudes :

$$\frac{d\sigma}{dt} \sim \sum_{\text{all } \lambda} \left| f_{\lambda_c\lambda_d;\ \lambda_a\lambda_b} \right|^2 \qquad (7\text{-}10)$$

7.1.2 Symmetry Considerations

Strong interactions are supposed to be invariant under the parity operation P and charge conjugation C. We shall see what sort of conditions this imposes upon the helicity amplitudes.

PARITY

The parity operator will change the direction of the momentum, but not the spin, and thus the sign of the helicities will be changed. The result from parity operation on a two particle state is

$$P|\lambda_a\lambda_b\rangle = \eta_a\eta_b(-1)^{J - s_a - s_b}|-\lambda_a, -\lambda_b\rangle$$

where η_a, η_b are intrinsic parities. In the case of baryon-antibaryon $\eta_a \cdot \eta_b = -1$.

Considering the properties of the functions $d_{\lambda\mu}(\theta)$ in eq. (7-9), we obtain the following condition on the helicity amplitudes :

$$f_{-\lambda_c-\lambda_d;-\lambda_a-\lambda_b}(\theta,\pi-\phi) = \eta_t * (-1)^{\lambda-\mu} * f_{\lambda_c\lambda_d;\lambda_a\lambda_b}(\theta,\phi)$$

where η_t depends on the intrinsic parities, and equals + 1 for reactions of type (7-7). Hence, if parity is conserved, the helicity amplitudes do not change under inversion of all helicities. So for the reaction (Y stands for hyperon) :

$$\bar{p}p \longrightarrow \bar{Y}Y$$

instead of initially 16 only 8 amplitudes are independent.

CHARGE CONJUGATION

This operation transforms a particle a into its antiparticle $\bar{a}$, whereas helicities are not changed. If the transition matrix T is invariant with respect to charge conjugation, one obtains from eq. (7-9) :

$$f_{\lambda_{\bar{d}}\,\lambda_c;\ \lambda_{\bar{b}}\lambda_a} = f_{\lambda_{\bar{c}}\,\lambda_d;\ \lambda_{\bar{a}}\lambda_b}$$

This means for auto-conjugate reactions like $\bar{p}p \rightarrow \bar{\Lambda}\Lambda$ and $\bar{p}p \rightarrow \bar{\Sigma}^o\Sigma^o$ that, apart from a sign, exchanging particles a and b does not change the corresponding amplitudes.

For the conjugate reactions $\bar{p}p \rightarrow \bar{\Lambda}\Sigma^o$ and $\bar{p}p \rightarrow \bar{\Sigma}^o\Lambda$, this implies that the amplitudes of the first reaction entirely determine the second one. Therefore, it is justified to add, as we have done, both classes of events for the d.c.s. calculation :

$$\frac{d\sigma}{d\Omega}\,(\bar{\Lambda}\Sigma^o) = \frac{d\sigma}{d\Omega}\,(\bar{\Sigma}^o\Lambda)$$

CP INVARIANCE

If we finally suppose that invariance under both parity operation and charge conjugation holds, there remain only 6 independent helicity amplitudes for $\bar{p}p \to \bar{\Lambda}\Lambda$ (and $\bar{\Sigma}^0\Sigma^0$) and only 8 amplitudes for $\bar{p}p \to \bar{\Lambda}\Sigma^0$ (and $\bar{\Sigma}^0\Lambda$).

$\bar{p}p \to \bar{\Lambda}\Lambda$

Using the notation of Plaut [PLA71] for this reaction, we are left with the following non-flip (index 0), single-flip (index 1) and double-flip amplitudes (index 2) :

$$f_0 = f_{++;\,++}$$

$$f_0' = f_{+-;\,+-}$$

$$f_1 = f_{++;\,+-} = f_{++;\,-+}$$

$$f_1' = f_{+-;\,++} = -f_{+-;\,--}$$

$$f_2 = f_{+-;\,-+}$$

$$f_2' = f_{++;\,--}$$

And for the d.c.s., we obtain :

$$\boxed{\frac{d\sigma}{dt} \sim N = |f_0|^2 + |f_0'|^2 + 2\left(|f_1|^2 + |f_1'|^2\right) + |f_2|^2 + |f_2'|^2} \qquad (7\text{-}12)$$

Using the concept of density matrices, as will be described in the following subsection, the polarization is given by :

$$\boxed{P = \frac{2}{N}\,\mathrm{Im}\left((f_0 - f_2')^*\, f_1' - (f_0' + f_2)^*\, f_1\right)} \qquad (7\text{-}13)$$

$\pi^- p \rightarrow K^o \Lambda$

The corresponding result for this reaction is much simpler. We only have to consider a non-flip amplitude A_N and a spin-flip amplitude A_F. So the d.c.s. in terms of these amplitudes reads :

$$\boxed{\frac{d\sigma}{dt} = |A_N|^2 + |A_F|^2} \tag{7-14}$$

For the polarization of the Λ particle, we use :

$$\boxed{P \frac{d\sigma}{dt} = 2 \ \mathrm{Im}(A_N A_F^*)} \tag{7-15}$$

7.1.3 Spin Density Matrix

A natural way to define polarization vectors and spin correlations is the introduction of the spin density matrix. In any reaction, one starts with a knowledge of the density matrix of the initial state, ρ_i, and one attempts to measure the density matrix ρ_f of the final state. Then ρ_f will contain all relevant dynamical information about the reaction.

So, if T denotes the transition matrix, ρ_f is defined by :

$$\rho_f = \frac{R_f}{\mathrm{Tr}(R_f)} \quad \text{with} \quad R_f = T_{\rho_i} T^+ = k \ \mathbb{F} \rho_i \mathbb{F}^+ \tag{7-16}$$

where $\mathbb{F}$ is the matrix containing the helicity amplitudes f_λ, k is a kinematical factor. In order to point out the relation to the d.c.s., using eq. (7-10), we can write :

$$\boxed{\frac{d\sigma}{d\Omega} \sim \mathrm{Tr}(R_f) = k \ \mathrm{Tr}(\mathbb{F} \rho_i \mathbb{F}^+)} \tag{7-17}$$

In the case of the reaction $\bar{p}p \to \bar{\Lambda}\Lambda$, the density matrix is of the form 4×4. Since in our experiment beam and target particles are unpolarized, the initial state density matrix is simply :

$$\rho_i = 1/4\ \mathbb{1}$$

The final state density matrix ρ_f, in general, will have 16 complex elements, representing 32 real parameters. They are reduced, due to the following properties of the density matrix :

1. $\rho_{ij} = \rho^*_{ji}$ (hermicity)
2. $\rho_{ii} \geq 0$ (positive real diagonal elements)
3. $\mathrm{Tr}(\rho) = 1$ (normalization)

Consequently, 15 parameters have to be determined only, in general. The hyperon and anti-hyperon polarization (2×3 components) and the 9 spin correlation terms, for example, can provide sufficient information to determine ρ_f. From eq. (7-16), which relates the density matrix to helicity amplitudes, and from symmetry considerations discussed in the preceding subsection, we already know that under parity conservation, only 8 parameters will remain independent.

A complete orthonormal base for the representation of any 4×4 matrix is supplied by the 16 matrices $\sigma_{ij} = \sigma_i \times \sigma_j$, where $\sigma_0 = 1$, and σ_1, σ_2, and σ_3 are the usual Pauli matrices. So we can express ρ_f in the following form [DUR64] :

$$\boxed{\rho_f = \frac{1}{4}\left(\mathbb{1} + \sum_i P_{\Lambda,i}\sigma_i \times \mathbb{1} + \sum_j P_{\bar{\Lambda},j}\ \mathbb{1} \times \sigma_j + \sum_{i,j} C_{ij}\ \sigma_i \times \sigma_j\right)} \quad (7\text{-}18)$$

$P_{\Lambda,i}$ and $P_{\bar{\Lambda},j}$ are the polarization components and C_{ij} the spin correlations between hyperon and anti-hyperon.

How can the observables defined in eq. (7-18) be measured ? First, we notice that the whole reaction process can be separated into the scattering of initial particles described by a transition matrix M and the subsequent hyperon decays governed by the matricea :

$$M_k = A_s \mathbb{1} + A_p \vec{\sigma} \cdot \hat{p} \qquad k = \Lambda, \bar{\Lambda} \tag{7-19}$$

where A_s and A_p are the s-wave and p-wave amplitudes in the weak hyperon decay process normalized to $|A_s|^2 + |A_p|^2 = (4\pi)^{-1}$, $\vec{\sigma} = (\sigma_1, \sigma_2, \sigma_3)$, and $\vec{p}$ is the momentum of the decay nucleon. Eq. (7-19) determines the decay distribution in the hyperon rest frame ($\hat{p} = \vec{p} / |\vec{p}|$) :

$$\frac{d\sigma}{d\Omega_k} \sim \mathrm{Tr}\ (M_k^+ M_k \rho_{f,k})$$

$$\text{where } M_k^+ M_k = \frac{1}{4\pi} (\mathbb{1} + \alpha_k \vec{\sigma} \cdot \hat{p}) \tag{7-20}$$

$$\text{and } \rho_{f,k} = \frac{1}{2} (\mathbb{1} + \vec{P}_k \cdot \vec{\sigma})$$

where $d\Omega_k$ is the solid angle in the hyperon rest frame and α_k is the asymmetry parameter in the weak decay :

$$\alpha_k = \frac{2\mathrm{Re}\ A_s^* A_p}{|A_s|^2 + |A_p|^2} \tag{7-21}$$

So for the whole process we have $T = M_\Lambda M_{\bar{\Lambda}} M$ and we can write the differential cross section in the case of $\rho_i = \frac{1}{4} \mathbb{1}$ [DUR64] :

$$\frac{d^3\sigma}{d\Omega\, d\Omega_\Lambda\, d\Omega_{\bar{\Lambda}}} = \mathrm{Tr}\,(M_\Lambda^+ M_\Lambda M_{\bar{\Lambda}}^+ M_{\bar{\Lambda}} \cdot \frac{1}{4} M^+ M) \tag{7-22}$$

$$= I_0(\theta) \frac{1}{(4\pi)^2} (1 + \alpha_\Lambda \vec{P}_\Lambda \cdot \hat{p}_p + \alpha_{\bar{\Lambda}} \vec{P}_{\bar{\Lambda}} \cdot \hat{p}_{\bar{p}}$$

$$+ \alpha_\Lambda \alpha_{\bar{\Lambda}} \sum_{i,j} C_{ij}\, \hat{p}_{p,i} \cdot \hat{p}_{\bar{p},j})$$

In order to extract the polarization and the spin correlations, one can employ the moment method [PIL67] and one obtains the results that were already introduced in section 6.3 while presenting the polarization data.

Since ρ_f and $\mathbb{F}$ are related by $\rho_f = \frac{k}{4} \mathbb{F}\ \mathbb{F}^+ / \mathrm{Tr}(R_f)$ (7-16) , the conditions imposed on the helicity amplitudes by invariance arguments will yield certain characteristics for the parameters used in the representation for ρ_f .

AUTO CONJUGATE REACTIONS

For the reactions $\bar{p}p \to \bar{\Lambda}\Lambda$ and $\bar{p}p \to \bar{\Sigma}^0\Sigma^0$ parity conservation P yields 8 conditions :

$$\boxed{\begin{aligned} &P_{\Lambda,x} = P_{\Lambda,z} = 0 \\ &P_{\bar{\Lambda},x} = P_{\bar{\Lambda},z} = 0 \\ &C_{xy} = C_{yx} = C_{yz} = C_{zy} = 0 \end{aligned}} \tag{7-23a}$$

This well-known result implies that under parity conservation, the polarization is normal to the production plane.

Charge conjugation C introduces in addition :

$$\boxed{\begin{aligned} &P_{\Lambda,y} = P_{\bar{\Lambda},y} = P_y \\ &C_{xz} = C_{zx} \end{aligned}} \tag{7-23b}$$

The correlations C_{ii}, $i = x,y,z$ may be non-vanishing. In addition, CP invariance yields : $\alpha_\Lambda = -\alpha_{\bar{\Lambda}}$.

CONJUGATE REACTIONS

For the reaction $\bar{p}p \to \bar{\Lambda}\Sigma^0$ and $\bar{\Sigma}^0\Lambda$ we have, apart from eq. (7-23a), the conditions :

$$\begin{aligned} &P_{\bar{\Lambda},y} = P_{\Lambda,y} \quad \text{and} \quad P_{\bar{\Sigma}^0,y} = P_{\Sigma^0,y} \\ &C_{xz}(\bar{\Lambda}\Sigma^0) = C_{zx}(\bar{\Sigma}^0\Lambda) \quad \text{and} \quad C_{zx}(\bar{\Lambda}\Sigma^0) = C_{xz}(\bar{\Sigma}^0\Lambda) \\ &C_{ii}(\bar{\Lambda}\Sigma^0) = C_{ii}(\bar{\Sigma}^0\Lambda), \quad i = x,y,z \end{aligned} \tag{7-24}$$

Finally, during Σ^0 decay into $\Lambda\gamma$, one finds [DUR64] :

$$\alpha_{\Sigma^0} = -1/3\ \alpha_{\Lambda} \tag{7-25}$$

7.1.4 Comparison with Polarization Data

After the general introduction given in the preceding sections, we can compare the consequence of CP invariance as expressed in eq. (7-23) with the results concerning hyperon polarizations.

$\pi^- p \to K^0\Lambda/\Sigma^0$

As in the case of hyperon - anti-hyperon production parity conservation should suppress the x- and z-components of the Λ polarization. At $p_{lab} = 3. - 3.3$ GeV/c, we measured the following mean values over the total angular range covered (cf. fig. 6-9) :

$$\boxed{\begin{aligned} P_{\Lambda,x} &= .02 \pm .17 \\ P_{\Lambda,y} &= -.79 \pm .17 \\ P_{\Lambda,z} &= -.06 \pm .24 \end{aligned}}$$

Within statistical errors, the theoretical predictions (see eq. (7-23a)) are well satisfied.

$\bar{p}p \to \bar{\Lambda}\Lambda$

Still at p_{lab} around 3 GeV/c we obtained the following mean values of the $\bar{\Lambda}$ and Λ polarizations :

$$\boxed{P_{\bar{\Lambda}\Lambda,y} = -.60 \pm .38}$$

The combination of $\bar{\Lambda}$ and Λ data is justified by eq. (7-24).

Results from a wire-chamber experiment [BEC78] performed at the CERN PS at 6 GeV/c show an $\bar{\Lambda}$ polarization of zero at $t' = 0$ which is constantly decreasing with $|t'|$ until $P_{\bar{\Lambda}} = -.78 \pm .40$ at $-t' = 0.9$ $(\mathrm{GeV/c})^2$. We find the same tendency in our experiment.

<u>$\pi^- p \to K^0 \Sigma^0$</u>

The mean polarization was $P_{\Lambda,y} = -.37 \pm .20$ around an average t value of -1.25 $(\mathrm{GeV/c})^2$. So with $\alpha_{\Sigma^0} = -1/3\ \alpha_{\Lambda}$ from eq. (7-25) this corresponds to :

$$\boxed{P_{\Sigma^0,y} = 1.11 \pm .60}$$

The error in this case is quite important. But this and all other results are compatible with the general condition on polarization $|P| \leq 1$.

As a comparison, we note the Σ^0 polarization found at $p_{lab} = 3.95$ GeV/c by Loverre et al. [LOV80] at $-t = 1.6$ $(\mathrm{GeV/c})^2$: $P_{\Sigma^0} = .80 \pm .50$.

As was pointed out in section 6.3, the limited statistics in our experiment did not permit to establish the spin correlation coefficients with sufficiently small errors. On the other hand, the polarization data in the strong interaction precesses which we studied are compatible with CP invariance.

7.2 Regge Models

At low beam energy and small momentum transfer, many experimental results are discussed in the framework of Regge models. Angular distributions up to $|t| \sim 1.5$ GeV/c are well explained. A paper by Navelet et al. [NAV76], for example, covers the range in p_{lab} between 3 and 15 GeV/c for the reaction $\pi^- p \to K^0 \Lambda$. Recently, a study of the reaction $\bar{p}p \to \bar{\Lambda}\Lambda$ was published by Saleem et al. [SAL81], who tried to reduce the number of parameters in the Regge approach while fitting data at $p_{lab} = 6$ GeV/c measured by Becker et al. [BEC78]. In a review article by Collins [COL71], a general introduction into the widespread domain of Regge models can be found. We want to see to what extend Regge amplitudes provide a useful description in the case of our experiment.

In Regge models, the interaction process is characterized by the exchange of Regge trajectories which are associated to particles that can be exchanged. A forward peak or backward peak in the angular distribution is expected if t-channel or u-channel exchange is possible, respectively. The particle exchanged is determined by the quantum numbers of the interacting particles. In table 7-1, we list important quantum numbers of particles involved in reactions which we studied.

	π^-	K^0	p	Λ	Σ^0
spin s	0	0	1/2	1/2	1/2
isospin I	1	1/2	1/2	0	1
I_3	- 1	-1/2	1/2	0	0

Table 7-1 : Quantum numbers involved in Regge models.

Fig. 7-1 illustrates the t-channel exchange of (a) $\pi^- p \to K^0\Lambda$ and (b) $\bar{p}p \to \bar{\Lambda}\Lambda$.

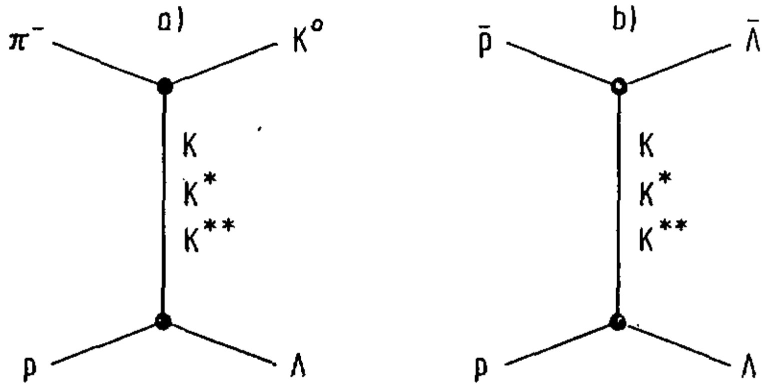

Fig. 7-1 : Regge exchange in the t-channel for (a) $\pi^- p \to K^0 \Lambda$ and (b) $\bar{p}p \to \bar{\Lambda}\Lambda$.

In both reactions, the exchanged object must have the following quantum numbers :

$$B = 0$$
$$Q = 1$$
$$S = 1$$
$$I = 1/2$$

These requirements are all satisfied by the strange meson K and its excited states K^* (892), K^{**} (1430), etc. Thus in both reactions one expects a forward peak in the d.c.s. distribution. Contributions from the K exchange are believed to be small (cf. e.g. [PLA71] and [SAL81]).

In table 7-2 we list Regge predictions concerning the existence of forward and backward peaks for some reactions we are interested in [COL71].

process	trajectories predicting	
	forward peak	backward peak
$\pi^-p \to K^0\Lambda$	$K^* + K^{**}$	$\Sigma_\alpha + \Sigma_\beta + \Sigma_\gamma + \Sigma_\delta$
$\pi^-p \to K^0\Sigma^0$	$K^* + K^{**}$	$\Sigma_\alpha + \Sigma_\beta + \Sigma_\gamma + \Sigma_\delta$
K^-p elastic	$P + f + \rho + A_2$	exotic
$\bar{p}p$ elastic	$P + f + \rho + A_2$	exotic
$\bar{p}p \to \bar{\Lambda}\Lambda$	$K + K^* + K^{**}$	exotic
$\bar{p}p \to \bar{\Sigma}^0\Sigma$	$K + K^* + K^{**}$	exotic

Table 7-2 : Regge trajectories.

7.2.1 Meson-Baryon Interaction

Using the parametrization of Regge amplitudes according to Navelet et al. [NAV76], we shall try to describe our data for $\pi^-p \to K^0\Lambda$ and $\pi^-p \to K^0\Sigma^0$.

Their analysis is based on Regge poles which account for K^* (892) (vector V) and K^{**} (1430) (tensor T) exchange and an additional effective cut for the non-spin-flip amplitude.

DIFFERENTIAL CROSS SECTION

As was pointed out in section 7.1, a non-flip amplitude, A_{++}, and a spin flip amplitude, A_{+-}, are necessary for the calculation of the d.c.s. (cf. eq. (7-14)).

$$\frac{d\sigma}{dt} = |A_{++}|^2 + |A_{+-}|^2$$

Each amplitude is the sum of vector and tensor contributions :

$$A_i = \sqrt{2}\ (H_i(K^*) \ + \ H_i(K^{**}))$$

with i = ++, +- for non-flip and flip amplitude respectively. Navelet et al. used the following parametrization for the helicity amplitudes H_i :

$$H_{++}^{\Lambda,\Sigma} = k\ \gamma_{++}^{\Lambda,\Sigma}\ (\tau + e^{-i\pi\alpha(t)})\ S^{\alpha(t)}\ e^{a_{++}t} \qquad (7\text{-}26)$$

$$H_{+-}^{\Lambda,\Sigma} = k\ \sqrt{-t'}\ \gamma_{+-}^{\Lambda,\Sigma}(\tau + e^{-i\pi\alpha(t)})\ S^{\alpha(t)}\ e^{a_{+-}t}$$

where k is a kinematical factor, γ's denote the residuals, τ the signature (- 1 for vector, + 1 for tensor), $\alpha(t)$ defines the Regge trajectory, and the a's determine the exponential fall-off at small $|t|$ values.

In analogy to ρ and A_2 exchange in elastic scattering, Navelet et al. added an effective cut term to the non-flip amplitude :

$$H_{++,c}^{\Lambda,\Sigma} \begin{Bmatrix} K^* \\ K^{**} \end{Bmatrix} = K\ \gamma_{++}^{\Lambda,\Sigma}\ \gamma^c \begin{Bmatrix} 1 \\ -1 \end{Bmatrix} (e^{-i\frac{\pi}{2}}\ S)^{\alpha_c(t)}\ e^{a_c t} \qquad (7\text{-}27)$$

These amplitudes require a total of 17 parameters (!) to describe the reaction with a $K^0\Lambda$ final state and 4 additional parameters for the $K^0\Sigma^0$ final state. With the parameters [NAV76] listed in table 7-3, we obtained the differential cross section distributions shown in fig. 7-2 for different WA13 beam moments.
Navelet et al. fitted the parameters using published data with $-t < 1.5\ (GeV/c)^2$.

So, except in fig. 7-2 (a), we have extrapolated the curves toward larger scattering angles.

The $K^0\Sigma^0$ distributions exhibit a marked dip around $-t \sim 0.6\ (GeV/c)^2$. Apart from that, there is overall agreement between $K^0\Lambda$ and $K^0\Sigma^0$ final state d.c.s.

Parameter	vector K^*	tensor K^{**}
$\alpha(t)$	0.375 + 0.678 t	0.322 + 0.678 t
γ^{Λ}_{++}	10.34	11.15
γ^{Σ}_{++}	12.46	12.83
γ^{Λ}_{+-}	- 9.862	- 7.114
γ^{Σ}_{+-}	13.53	11.63
a_{++}	2.414	1.331
a_{+-}	1.895	1.895
$\alpha_c(t)$	0.099 + 0.532 t	0.127 + 0.532 t
γ^c	1.01	1.44
a^c	1.134	0.091

Table 7-3 : Regge amplitude parameters for $\pi^- p \to K^0\Lambda/\Sigma^0$.

What is, in general, the ratio between the d.c.s. $d\sigma/dt$ (for the $K^0\Lambda$ final state) and $d\sigma/dt$ ($K^0\Sigma^0$ final atate) ?

Since we have separated these two reactions at low energies, we can compare them to predictions based on the SU(3) isoscalar factors.

If Yukawa type coupling (that is, exchange of an octet) is assumed in meson-baryon interaction, only a symmetric coupling, called D, and an antisymmetric coupling, F, are possible within exact SU(3) limits. From the coupling constants $g_{N\Lambda K}$ and $g_{N\Sigma K}$ as a function of F and D one obtains [SWA63] the ratio R :

$$R = \frac{d\sigma(\Sigma)}{d\sigma(\Lambda)} \sim \frac{g^2_{N\Sigma K}}{g^2_{N\Lambda K}} = \left(\sqrt{3}\,\frac{(F/D - 1)}{(3\,F/D + 1)} \right)^2 \qquad (7\text{-}28)$$

In the forward direction this ratio was found to be ~ 0.8 at $p_{lab} = 3$ GeV/c [BOU80]. Loverre et al. pointed out that, in contrast to general belief, R is not constant in - t [LOV80].

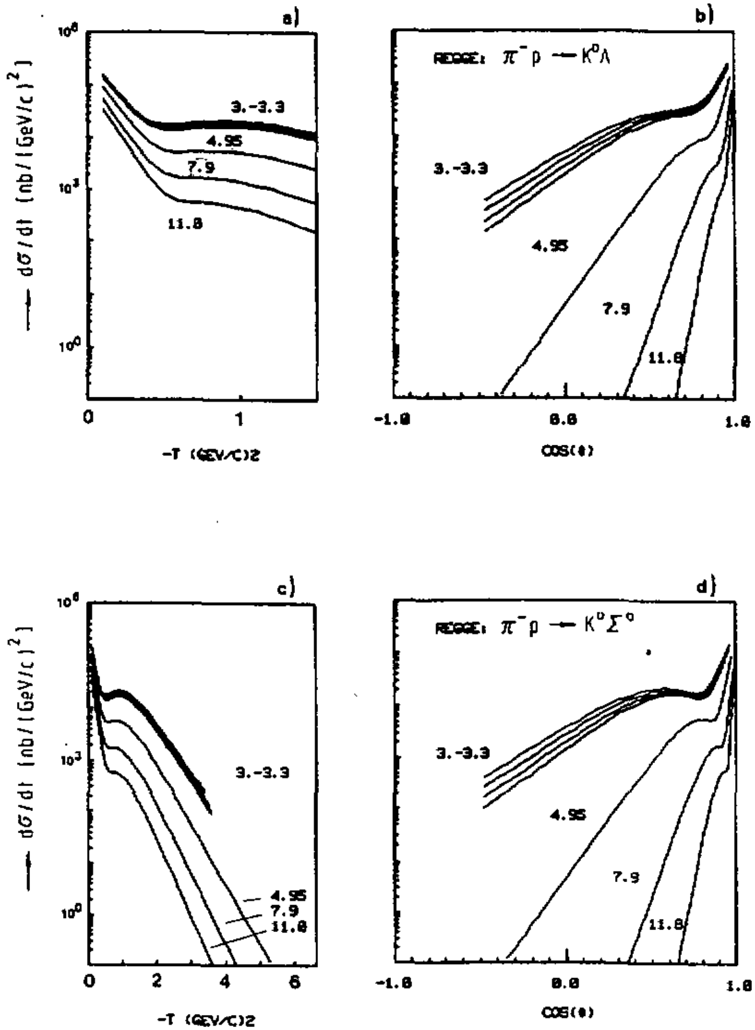

Fig. 7-2 : *Regge model of ref. [NAV76] for the differential cross section of $\pi^-p \to K^0\Lambda$ (a) and (b) and of $\pi^-p \to K^0\Sigma^0$ (c) and (d) as a function of $-t$ and $\cos\theta^*$ respectively.*

If we compare the ratio of the numbers of events with $K^0\Lambda$ final states and $K^0\Sigma^0$ final states at 3. - 3.3 GeV/c and 4.95 GeV/c in the interval $-.5 < \cos\theta^* < .9$, we obtain, after correction for slightly different acceptance values, an average value for R :

$$R\ (3.-3.3\ \text{GeV/c}) \approx .75 \pm .11$$

$$R\ (4.95\ \text{GeV/c}) \approx .90 \pm .25$$

As far as the shape of the d.c.s. is concerned, we plotted the Regge predictions together with predictions from other models in fig. 7-6, and fig. 7-7 for different beam momenta. As can be seen from those figures, our data departs from the Regge behaviour for $|t| > 2.-3\ (\text{GeV/c})^2$. This is due to the exponential term in the Regge amplitudes.

The data points we included in the forward direction from other experiments are well described by this approach.

In the parametrization presented above, one could include an additional contribution which accounts for the backward peak (Σ^0 exchange in the u-channel) that is roughly 2 orders of magnitude smaller than the forward peak [AST75].

The values that are reached by extrapolaring this contribution to $\cos\theta^* = 0$ would not, however, be able to account for the large angle data.

Apart from the $K^0\Lambda$ final state, a backward peak was also found for the $K^{0*}(892)\Lambda$ channel at 9 and 12 GeV/c [FER81].

POLARIZATION

Based on the definition of eq. (7-15) Navelet et al. find the polarization as a function of momentum transfer as is plotted in fig. 6-10. Since the polarization is proportional to product terms between the real (imaginary) part of the non-flip amplitude and the imaginary (real) part of the spin flip amplitude, it vanishes at t = 0 and tends to return to zero again at large $|t|$ values.

A final remark has to be added. Twenty-one parameters are involved in the fit of Regge amplitudes in the approach of Navelet et al. It is therefore not very appropriate to call it a "theoretical prediction".

7.2.2 Baryon-Baryon Interaction

Saleem at al. recently published an interpratation of the d.c.s. and polarization found in $\bar{p}p \to \bar{\Lambda}\Lambda$ at 6 GeV/c [BEC78] by assuming the reaction to be dominated by K^* and K^{**} exchange. They use a simple Regge pole model with phenomenological residue functions assuming that each of the two trajectories is coupled only to one of the two non-vanishing independent helicity amplitudes.

From the original 6 amplitudes (see the definition of the d.c.s. in eq. (7-12)), only those with $\Delta\lambda = 0$ and $\Delta\lambda = 1$ are retained. The combination of amplitudes with the same helicity flip $\Delta\lambda$ further reduces the number of parameters. So the following parametrization is used :

$$f_0 = \gamma_0(t)\ \xi_0(t)\ s^{\alpha_{K^*}(t)} \qquad (7\text{-}29a)$$

$$f_1 = \sqrt{-t'}\ \gamma_1(t)\ \xi_1(t)\ s^{\alpha_{K^{**}}(t)}$$

Here $\xi_0(t)$ and $\xi_1(t)$ denote the signature factors, $\alpha_{K^*}(t)$ and $\alpha_{K^{**}}(t)$ stand for the Regge trajectories K^* and K^{**}, respectively. The residue functions contain the exponential t-behaviour. The trajectories they employed are :

$$\begin{aligned} \alpha_{K^*}(t) &= 0.485 + 0.6\ t \\ \alpha_{K^{**}}(t) &= 0.375 + 0.678\ t \end{aligned} \qquad (7\text{-}29b)$$

With this parametrization, Saleem et al. fitted the data until $-t \sim 1.75\ (\mathrm{GeV/c})^2$. We have used their results to plot in fig. 7-3 the d.c.s. and the polarization at beam energies of our experiment.

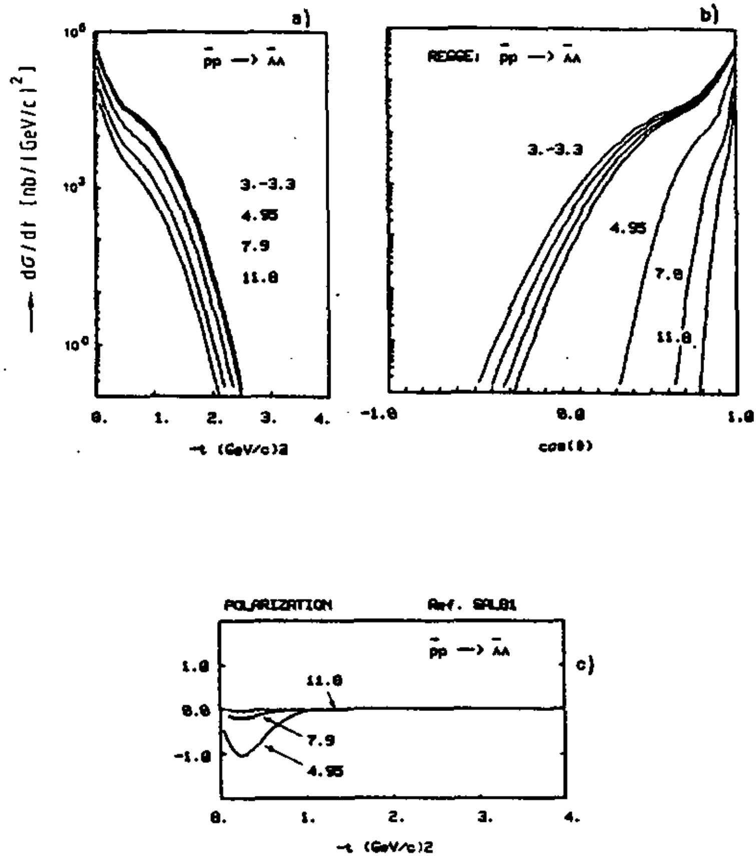

Fig. 7-3 : *Regge model parametrization for the differential cross section of $\bar{p}p \to \bar{\Lambda}\Lambda$ as a function of (a) $-t$ and of (b) $\cos\theta^*$. The predicted Λ polarization is also shown at different beam momenta [SAL81].*

The prediction for the d.c.s. are compared to WA13 in fig. 7-11. As in the case of meson-baryon scattering, the Regge curve falls off rapidly beyond $-t \sim 2$ $(GeV/c)^2$. An important difference, however, can be noted for the backward direction. Since the u-channel in $\bar{p}p \rightarrow \bar{\Lambda}\Lambda$ is exotic, no backward peak should exist.

We cannot confirm this prediction from the WA13 results alone. But experimental data at 3 GeV/c from Jacobs et al. [JAC78] shows no increase in the shape of the angular distribution around $\cos\theta^* = -1$.

At higher energies, no data in the backward direction is available at present.

As far as the prediction for the polarization of Λ and $\bar{\Lambda}$ is concerned, fig. 7-3 (c) shows that from Regge amplitudes one expects a polarization that tends to zero with increasing energy and/or increasing 4-momentum transfer. The prediction of Saleem et al. agrees only at low energies with the negative polarization value which we obtained around 3 GeV/c.

CROSS SECTION RATIOS

From SU(3) invariance, as expressed in eq. (7-28), one can derive the ratio between the cross sections of the reactions (a) $\bar{p}p \rightarrow \bar{p}p$, (b) $\rightarrow \bar{\Lambda}\Lambda$, (c) $\rightarrow \bar{\Lambda}\Sigma^0$ + c.c. and (d) $\rightarrow \bar{\Sigma}\Sigma^0$. Two cases are important according to whether the F or the D amplitudes are dominant [TAN64].

The predictions normalized to 9 (and 1 respectively) are listed in table 7-4 together with experimental results for total cross section ratios at various beam momenta ([BAD67] at 2.5 GeV/c, [BAL65] at 3.7 GeV/c and [CHI66] at 7 GeV/c).

reaction	ratios predicted by SU(3)		ratios of σ_{tot} (references)			ratios of $d\sigma/dt$ (WA13)	
	dominance		BAD67	BAL65	CHI66	$-.5 < z < .9$	$z \sim 0.$
$\bar{p}p \to$	F	D	2.5	3.7 [GeV/c]	7	3. -3.3 [GeV/c]	7.8
a) $\bar{p}p$	16	16	-	2260 ± 98	-	-	30 ± 6
b) $\bar{\Lambda}\Lambda$	9	1	9 ± .6	9 ± .9	9 ± 1.7	9 ± 1.3	9 ± 3.
c) $\bar{\Lambda}\Sigma^0$ + c.c.	6	6	4.6 ± .7	10.6 ± 3.	8.8 ± 1.6	8.6 ± 1.7	-
d) $\bar{\Sigma}^0\Sigma^0$ *)	1	9	< 1.	< 4.	< 2.	-	

*) Experimental limits are derived from $\bar{\Sigma}^-\Sigma^+$ + c.c. final states.

Table 7-4 : Cross section ratios.

The conclusion that can be drawn from table 7-4 is that both the total cross section ratios from the references and the d.c.s. ratio at large angles are in favour of F amplitude dominance.

Taking the elastic scattering (a) into account, another interesting result is obtained. From F amplitude dominance, it follows for the total cross section ratio :

$$R_{el} = \frac{\sigma_{el}}{\sigma(\bar{\Lambda}\Lambda)} = 1.78$$

Experimentally one finds $R_{el} \simeq 251$ at 3.7 GeV/c ([HER79] and [BAL65]). On the other hand, at higher energy and large angle at 7.8 GeV/c, we measured the differential cross section ratio

$$\frac{d\sigma_{el}}{d\sigma(\bar{\Lambda}\Lambda)} \sim 3.5 \pm 1.5$$

which is much nearer to the F dominance hypothesis.

7.3 Dimensional Quark Counting Rule

As a first theoretical approach to the description of large angle cross section, we want to present the quark counting rule derived in 1973 by Natveev et al. [MAT73] on the grounds of dimensional arguments.

Based on the assumption that the particles a and b involved in an elastic scattering process $a + b \to a + b$ contain n_a and n_b constituents (which can ba identified as quarks) the d.c.a. is of the form :

$$\frac{d\sigma}{dt} = \frac{1}{s^2} \left|\langle a\, b|T|a\, b\rangle\right|^2 = \frac{1}{s^2} \left|F_a\; F_b \langle n_a n_b|T|n_a\; n_b\rangle\right|^2 \qquad (7\text{-}30)$$

$$= F_a^2\, F_b^2 C\ (s,t)$$

where F_a, F_b are the form factors of particles a and b respectively; $|n_a\, n_b\rangle$ denotes the two particla state constituted by n_a and n_b quarks.

From the normalization of a ona particle state $([|i\rangle] = m^{-1})$, we obtain the dimension of the function $C(s,t)$:

$$[C(s,t)] = m^{-4(n_a + n_b - 1)}$$

Next Matveev et al. formulated the hypothesis of scale invariance ("automodelity hypothesis") : At large s,t,u ($\gg m^2$) and for fixed t/s all essential dimensional constants are contained in the form factors F_a, F_b. Then $C(s,t)$ only depends on the kinematical variables s and t, and under change of scale ($p \to \lambda p$, $s \to \lambda^2 s$, $t \to \lambda^2 t$) $C(s,t)$ transforms like a homogeneous function. Thus

$$C(s,t) \to C(\lambda^2 s,\lambda^2 t) = \lambda^{-4(n_a + n_b - 1)}\; C(s,t)$$

This equation is satisfied by the ansatz

$$C(s,t) = s^{-2(n_a + n_b - 1)}\; \phi(t/s)$$

So from eq. (7-30) one gets

$$\boxed{\frac{d\sigma}{dt} = s^{-(N-2)} f(t/s)} \qquad (7\text{-}31)$$

where $N = 2(n_a + n_b)$ is twica the number of quarka of the incident particles a and b.

Assuming $n_a = 2$ and $n_b = 3$ for the quark content in mesons and baryons respectively, the following predictions at fixed (large) angle for the strange particle processes which we analyzed are obtained :

$$\boxed{\begin{aligned} &\frac{d\sigma}{dt}(\pi^- p \to K^0\Lambda) \sim s^{-8} \\ \\ &\frac{d\sigma}{dt}(\bar{p}p \to \bar{\Lambda}\Lambda) \sim s^{-10} \end{aligned}} \qquad t/s \text{ fixed, } s \gg m^2 \qquad (7\text{-}32)$$

Though in the WA13 experiment the condition $s \gg m^2$ was not entirely satisfied, we can use the data at $\theta^* = 73^0$ presented in fig. 6-7 to draw a straight line through the data points at 4.95 GeV/c and 7.8 GeV/c for the reaction $\pi^- p \to K^0\Lambda/\Sigma^0$. From the slopa, we gat ($n = N - 2$):

$$\boxed{n_{\theta^*=73^0} = 8.5 \pm .9}$$

In fig. 6-7 the theoretical result S^{-8} is indicated by the dotted line.

After having discussed predictions for the shape of tha d.c.s. ($f(t/s)$ in eq. (7-31)), we will try to extrapolate our data to $\theta^* = 90^0$.

As far as the reaction $\bar{p}p \to \bar{\Lambda}\Lambda/\Sigma^0$ is concerned, due to missing data at 4.95 GeV/c, no comparison can be made with the counting rule based on

WA13 data alone. On the other hand, no results are available from other experiments at sufficiently high energies and large angles so far (1982).

7.4 Constituent Interchange Model

In 1973, Gunion, Brodsky and Blankenbecler proposed a model [GUN73] for the description of hadronic scattering in the large angle, large momentum transfer region which was based on the central assumption that only an interaction of an exchange of a single constituent is possible during the short interaction time. Amongst the two basic types of interactions between hadrons,

a) gluon exchange and

b) constituent interchange,

they discarded the direct elementary interaction (a) between individual constituents, which, if dominant, would lead to contradiction to experimental observations, like the lack of large corrections to Bjorken scaling and the striking difference in the angular distribitions of $\bar{p}p$ and pp scattering. In addition, their model supplies a smooth transition from fixed angle behaviour (power law at large angles) to conventional Regge behaviour (exponential fall-off of the forward peak).

7.4.1 Power Law

The scattering amplitude M that Gunion et al. obtained in their calculations for the general process a + b → c + d depends on the asymptotic behaviour of form factors F :

$$M = s \cdot F(s) \cdot F(t) \cdot F(u) \cdot I(z) \qquad (7\text{-}33)$$

where $z = \cos\theta^*$ and I(z) depends on the wave function of particle b and is usually slowly varying in z.

The form factors in eq. (7-33) are calculated by describing a composite particle state in the framework of perturbation theory in the infinite momentum frame. The results which are obtained for pions and nucleons are

$$F\ (q^2) \sim (-q^2)^{-1} \qquad \text{(monopole)} \qquad (7\text{-}34)$$

$$F\ (q^2) \sim (-q^2)^{-2} \ln\left(\frac{-q^2}{2}\right) \qquad \text{(dipole)}$$

Hence asymptotically for $s >> m^2$ from the last two equations one obtains a power law behaviour of the d.c.s. at 90^0 :

$$\frac{d\sigma}{dt}\ (90^0) \sim \frac{1}{s^2}\ |M|^2 = s^{-2(A+C+D)}\ I(0) \qquad (7\text{-}35)$$

The exponents A, C, and D correspond to the power fall-off of the form factors of particles a, c, and d respectively. So, for pp elastic scattering $(A = C = D = 2)$ Gunion et al. predict :

$$\frac{d\sigma}{dt}\ (pp) \sim s^{-12} \qquad (7\text{-}36a)$$

where the nucleon is considered as a quark - core system.

This result is in disagreement with the quark counting rule predictions of eq. (7-32). In a later paper, Blankenbecler pointed out [BLA74] that considering the nucleon as a 3 quark state would lead to a s^{-10} behaviour also in the CIM model.

For $\pi^- p$ interaction (7-35) yields $(A = C = 1,\ D = 2)$:

$$\frac{d\sigma}{dt}\ (\pi^- p) \sim s^{-8} \qquad (7\text{-}36b)$$

7.4.2 Angular Distributions

Depending on the type of particles involved in the interaction, different diagrams contribute to the scattering amplitude.

In the (ut) topology constituents are interchanged between the incoming meson (baryon) and the outgoing baryon (meson). If anti-quarks are present, graphs of the (st) and (su) topology, where a constituent is exchanged between the two incoming particles, must also be included.

Since quark flavours are crucial in the diagrams to be considered, we list some important quark quantum numbers and the quark content of several hadrons in table 7-5.

Name	Q	B	S	I	I_3
u	2/3	1/3	0	1/2	1/2
d	- 1/3	1/3	0	1/2	- 1/2
s	- 1/3	1/3	- 1	0	0

particle	π^-	K^0	K^-	p	Λ	Σ^0
content	$d\bar{u}$	$d\bar{s}$	$s\bar{u}$	uud	uds	uds

Table 7-5 : Quark quantum numbers and quark content of some hadrons.

Gunion et al. gave explicit formulae [GUN73] for the angular distributions of pion and proton induced elastic processes. In the case of kaons, they assumed the K-meson form factor to scale with the pion form factor.

Based on the valence quark content of strange particles, we can extrapolate their approach to the reactions $\pi^- p \to K^0\Lambda$ and $\bar{p}p \to \bar{\Lambda}\Lambda$. The only possible exchange diagrams are the (st) topologies depicted in fig. 7-4.

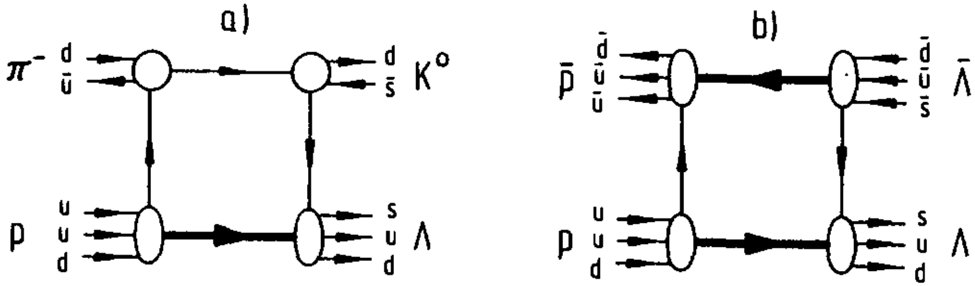

Fig. 7-4 : *(s,t) topologies in the CIM model for the reaction (a) $\pi^- p \to K^0\Lambda$ and (b) $\bar{p}p \to \bar{\Lambda}\Lambda$.*

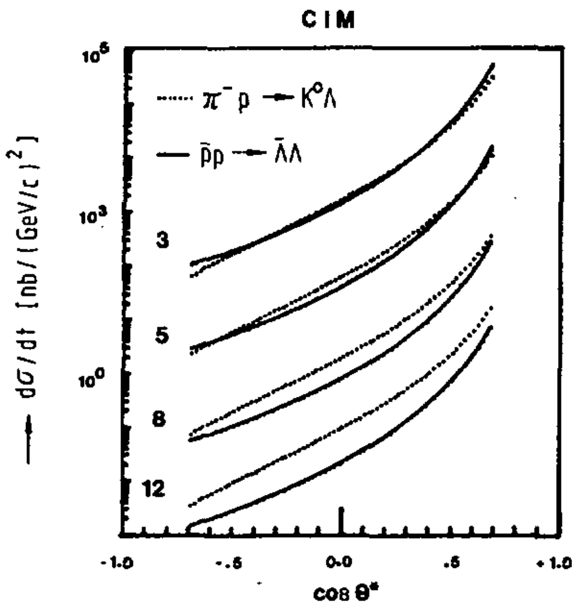

Fig. 7-5 : *CIM predictions at WA13 beam momenta. (The absolute normalisation is arbitrary.)*

The same type of CIM interchange diagrams describe the elastic progress $K^-p \to K^-p$ (similar to fig. 7-4a) and the annihilation process $\bar{p}p \to \bar{p}p$ (similar to fig. 7-4b).

The corresponding amplitudes, as calculated in [GUN73], lead to the following explicit form for the d.c.s. :

$$\boxed{\frac{d\sigma}{dt}(\pi^-p \to K^0\Lambda) = \frac{c_0}{s^8}\,\frac{1+z}{(1-z)^4}} \qquad (7\text{-}37a)$$

and

$$\boxed{\frac{d\sigma}{dt}(\bar{p}p \to \bar{\Lambda}\Lambda) = \frac{c_1}{s^{10}}\,\frac{1}{(1-z)^5}} \qquad (7\text{-}37b)$$

here $z = \cos\theta^*$. The normalization factor c_0 is related to the corresponding factor c_{el} of the elastic process by $c_{el} = 9\,c_0$.

Thus at 90 c.m.s., we have :

$$\frac{d\sigma}{dt}(\pi^-p \text{ elastic}) : \frac{d\sigma}{dt}(\pi^-p \to K^0\Lambda) = 9 : 1 \qquad (7\text{-}38)$$

The second formula in (7-37) is based on $s \leftrightarrow u$ crossing from the pp elastic scattering d.c.s.

$$\frac{d\sigma}{dt}(pp \text{ elastic}) = s^{-10}\,(1-z)^{-5}\,I(z)$$

The power in $(1-z)^{-5}$ is near to the fit $(1-z)^{-5.2}$ obtained from a fit to experimental results at 5 GeV/c (see GUN73).

In fig. 7-5 we plotted the CIM d.c.s. for different beam momenta. The normalization was chosen arbitrarily for this graph. To be complete, we included the CIM predictions also at 3 GeV/c, though the high energy condition $s \gg m^2$ is not fulfilled at this energy.

COMPARISON WITH DATA

Results from WA13 for the reaction $\pi^- p \to K^0\Lambda/\Sigma^0$ are shown, together with data points from other experiments, in fig. 7-6 around 3 GeV/c and 5 GeV/c, and in fig. 7-7 at 7.8 GeV/c. 1-V0 events were included in some cases.

Around 3 GeV/c, the data is well accounted for by the Regge model until $\cos\theta^* = 0$. At 4.95 GeV/c and at 7.8 GeV/c, the CIM model roughly follows our data points, though for $\cos\theta^* < .5$ the CIM curve seems to decrease too rapidly. Below $\cos\theta^* = 0$, the CIM prediction obviously misses the appearence of the backward peak.

We have fitted eq. (7-37a) to the data at 4.95 GeV/c and 7.8 GeV/c (2-V0 events only) in the domain $\cos\theta^* < .75$, while the power s^{-n} was not fixed. Fig. 7-8 shows the result for the d.c.s. at 90° c.m.s. For the n, we obtained :

$$\boxed{n = 8.6 \pm .9}$$

This result should be compared to the quark counting law prediction of $n = 8$ in meson-baryon scattering.

If we include data points around 3 GeV/c in the interval $|\cos\theta^*| < .2$ - though the d.c.s. is mainly Regge behaved and relatively large - the result is :

$$n = 8.7 \pm .4$$

In some diagrams, we plotted only 1/2 $d\sigma/dt$ of the sum of the $K^0\Lambda$ and $K^0\Sigma^0$ final state. We were encouraged to do so since both d.c.s. distributions are very similar in shape and magnitude (see section 7.2).

If we compare the corresponding elastic scattering data [BAC81] of WA13 at 90 c.m.s., we find the ratio :

$$\frac{d\sigma}{dt}(\pi^- p \text{ elastic}) : \frac{d\sigma}{dt}(K^0\Lambda) = 8 \pm 3$$

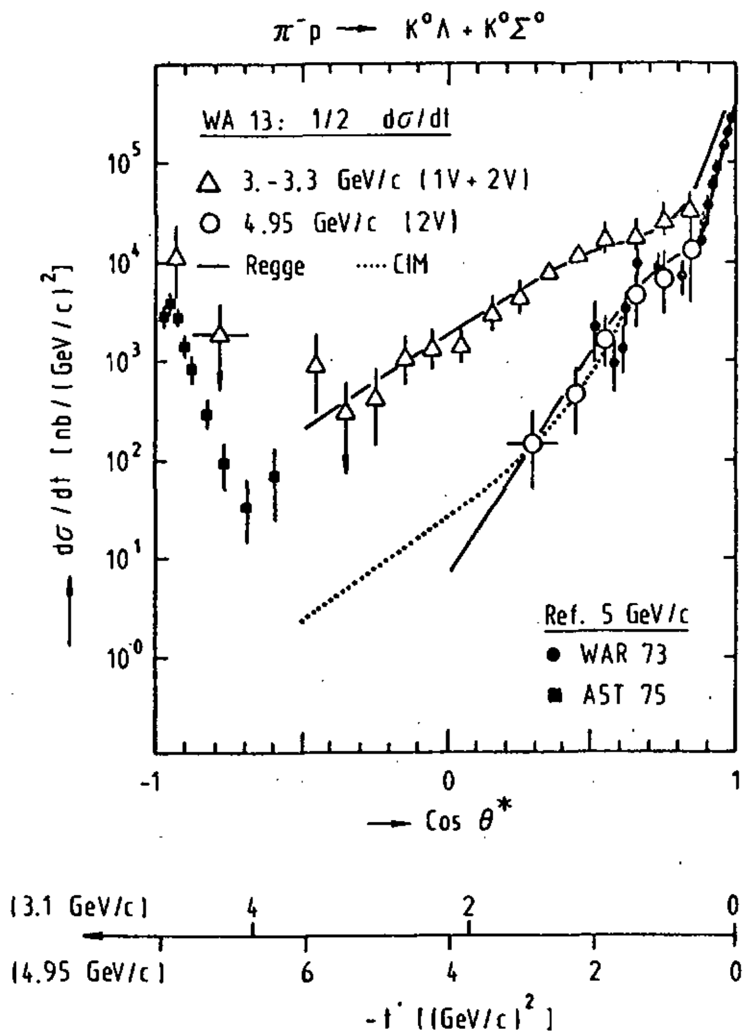

Fig. 7-6 : *WA13 results at p_{lab} around 3 GeV/c and 5 GeV/c for $\pi^- p \to K^0\Lambda/\Sigma^0$ compared to Regge model and CIM predictions. The references included at 5 GeV/c are from [WAR73] and [AST75].*

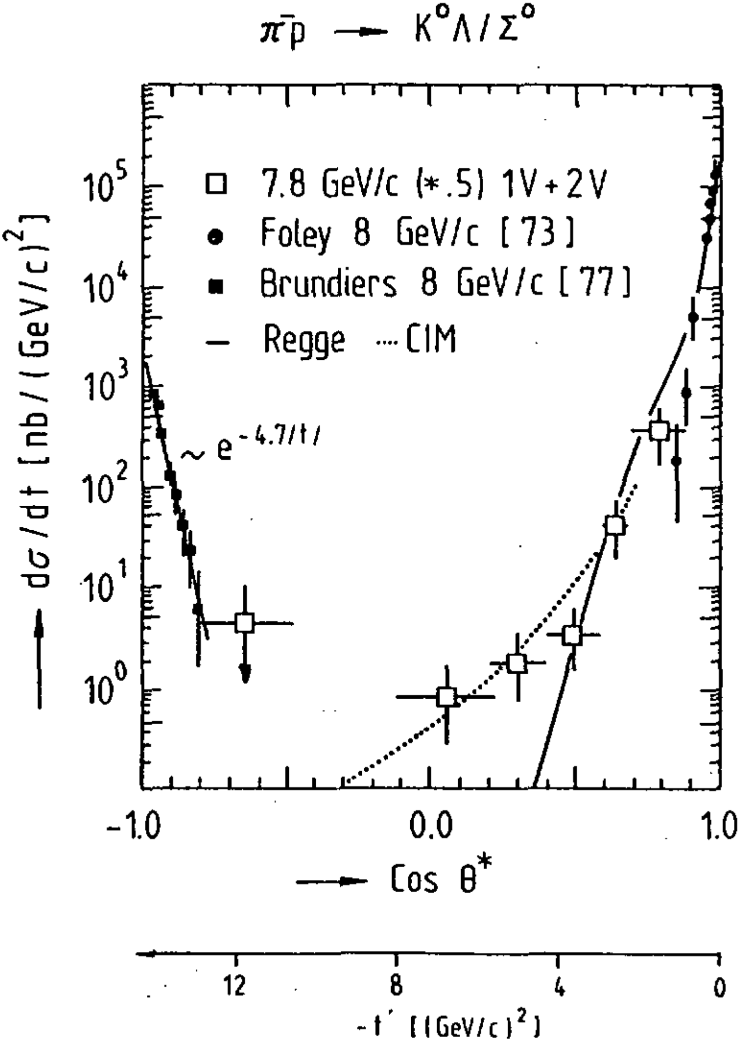

Fig. 7-7 : Differential cross section including 1V0 events at 7.8 GeV/c for $\pi^- p \rightarrow K^0 \Lambda/\Sigma^0$. Forward data from [FOL73] and backward data from [BRU77].

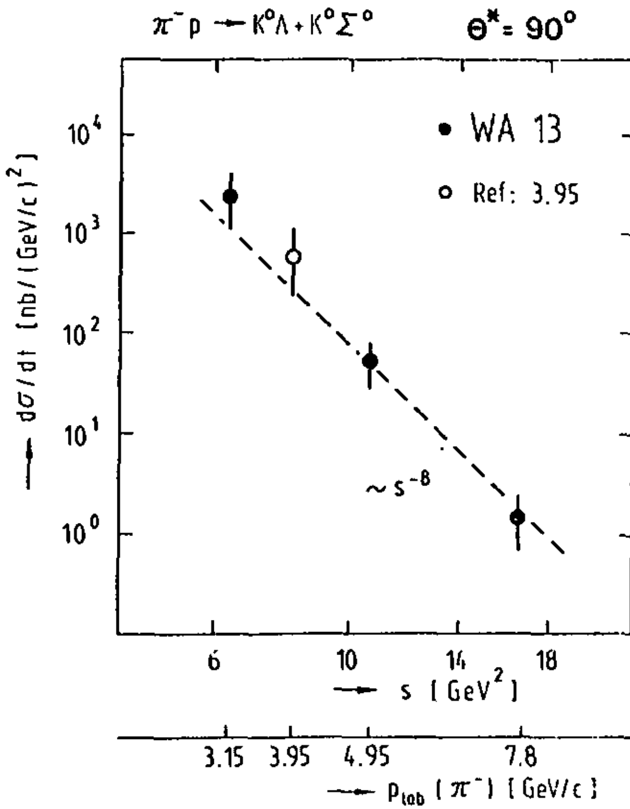

Fig. 7-8 : Diff. cross section at 90^0 c.m.s. obtained by fitting the CIM model to the 2V0 data for $\pi^- p \to K^0\Lambda/\Sigma^0$. The ref. is from [LOV80]. The quark counting law prediction is indicated by the dotted line.

This is roughly what we expected from eq. (7-38).

The CIM prediction for the reaction $\bar{p}p \to \bar{\Lambda}\Lambda/\Sigma^0$ according to eq. (7-37b) is added in fig. 7-11 as dotted line. Again we used data points with $\cos\theta^* < .75$ to fix the absolute normalization while sticking to the power law s^{-10}. At 7.8 GeV/c, the CIM d.c.s. seems to fall off too rapidly.

Very little data is available from other experiments at high energies. In particular, one would like to verify whether the absence of a backward peak in $\bar{p}p \to \bar{\Lambda}\Lambda$ (as was predicted from Regge models) can be confirmed. The data points we included for the backward domain at 3 GeV/c was taken from [JAC78], and we plotted 1/2 ds/dt of the $\Lambda\bar{\Sigma}^* + \Sigma\bar{\Lambda}$ final states. Their data smoothly completes our measurements beyond $\cos\theta^* = -.4$.

In the $\bar{p}p$ elastic channel, a small signal was found in the backward region by Eide et al. [EID73]

It will be up to future experiments to investigate this domain more thoroughly.

7.5 Massive Quark Model

In contrast to the perturbative QCD approach with its difficulties concarning normalization of amplitudes and confinement of quarks, in 1973 Preparata [PRE73] proposad the massive quark model (MQM). In a later paper on structure functions in deep inelastic processes the basic ideas of tha MQM model are summarized as follows :

(i) The quark degrees of freedom exist only in finite space-time domains (bags).

(ii) In the bag domains quarks have the same behaviour as low (effective) mass hadrons (Regge behaviour).

(iii) Quarks, like in the quark-parton model, have a point coupling to electromagnetic and weak currents.

In a recent article Preparata & Soffer applied these principles to meson-baryon elastic scattering [PRE80]. The principle of the MQM approach is first to choose a quark in each of the incoming particles, and secondly to consider the subprocesses as a Regge behaved quark-quark interaction. Contributions from various diagrams have to be considered. As is shown in fig. 7-9, thera are three meson-exchange diagrams according to the meson exchange channels s, t, and u and two baryon exchange diagrams. Summing over all possible Regge exchange diagrams yields in the limit of $s \to \infty$:

$$\frac{d\sigma}{dt} \text{ (meson-baryon)} = \frac{1}{s^9} \log^2 \left(\frac{s}{m_0^2}\right) \quad F_{MB}(\theta^*) \tag{7-39a}$$

where the parameter m_0^2 is set to 2 GeV^2. The function F_{MB} (θ^*) determines the shape of the angular distribution.

Applying the MQM model to nucleon-nucleon scattering Preparata & Soffer calculated the d.c.s. [PRE79] at the high energy limit :

$$\frac{d\sigma}{dt}\ (\text{nucleon-nucleon}) = \frac{1}{s^{11}}\ \log^2\left(\frac{s}{m_1^2}\right)\ F_{NN}\ (\theta^*) \qquad (7\text{-}39b)$$

where $m_1^2 = 4\ GeV^2$ and $F_{NN}\ (\theta^*)$ describes the angular dependence of the d.c.s.

A comparison of the model of Preparata & Soffer at $\theta^* = 90^\circ$ with the dimensional counting rule is shown in fig. 7-10.

It follows that in the domain covered by WA13 beam energies there is no significant difference between the two models as far as the power law at 90° c.m.s. is concerned.

A calculation of the d.c.s. of the reaction $\bar{p}p \to \bar{\Lambda}\Lambda$ within this model was recently performed by J. Soffer [SOF82]. The prediction for beam momenta at 12 GeV/c and 16 GeV/c are shown in fig. 7-11. This figure summarizes all WA13 data for this reaction, some references, and predications from the Regge and the CIM model. Our data points reach values that are some 3 orders of magnitudes smaller than the d.c.s. values of other experiments included in fig. 7-11. Yet we cannot decide between the MQM and other models based on our data at 7.8 GeV/c since the MQM predictions are available only above 10 GeV/c.

Compared to the CIM model at 12 GeV/c the model of Preparata & Soffer has a much flatter shape in the d.c.s. distribution.

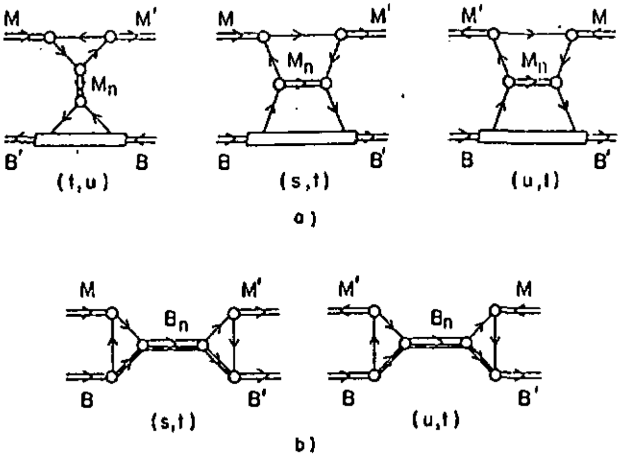

<u>Fig. 7-9</u> : *MQM diagrams for meson-baryon interaction :
(a) meson exchange and (b) baryon exchange contributions.*

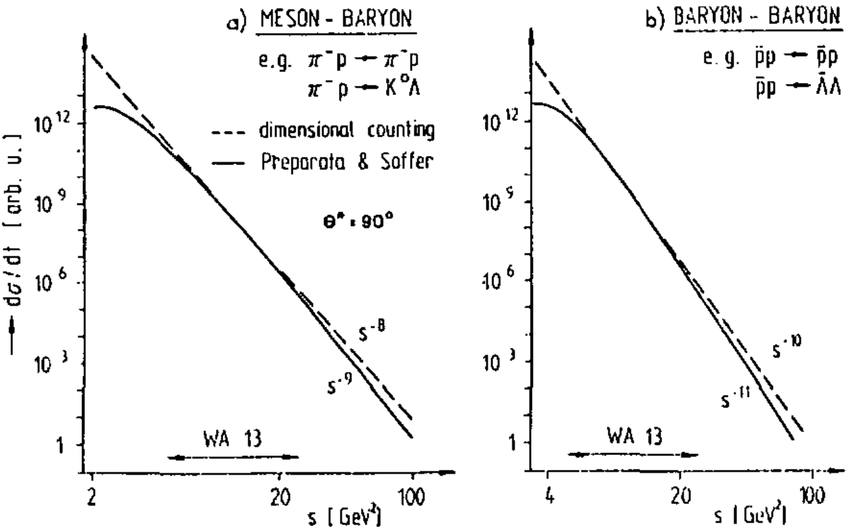

<u>Fig. 7-10</u> : *Predictions of the quark counting law and the MQM model of Preparata & Soffer for the diff. cross section at 90° c.m.s. for (a) meson-baryon and (b) baryon-baryon interactions.*

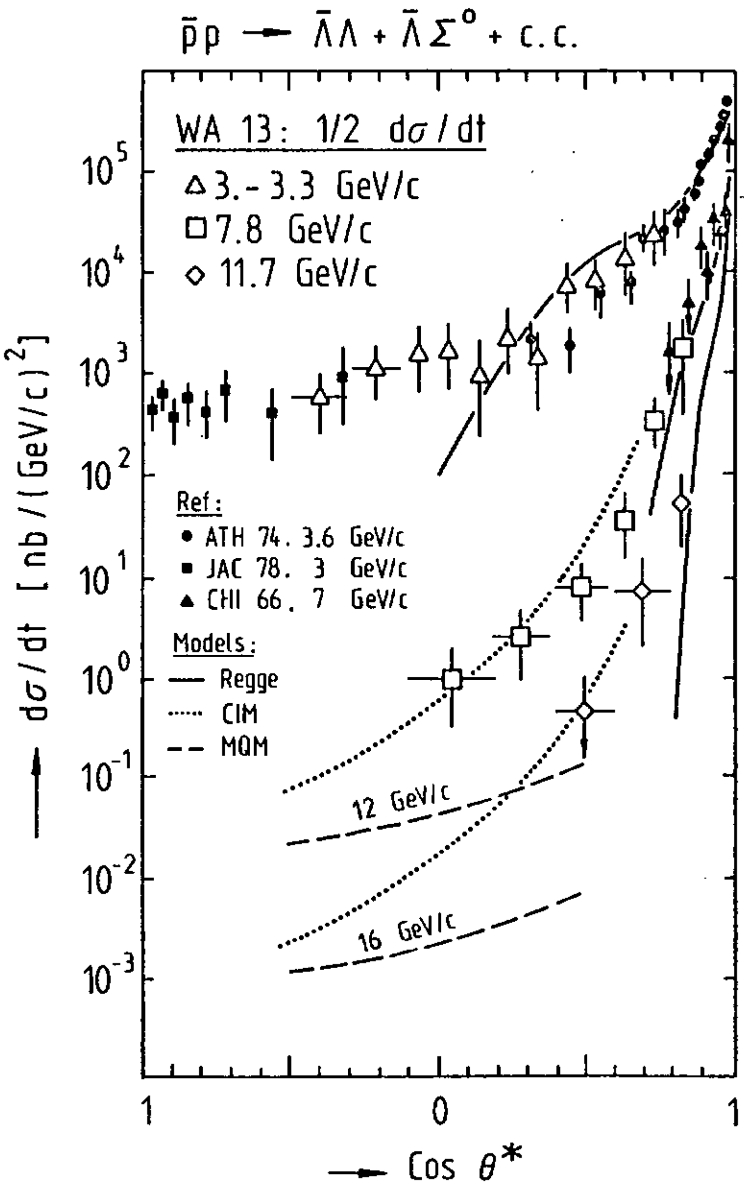

Fig. 7-11 : *Summary of WA13 data for the diff. cross section in the reaction $\bar{p}p \rightarrow \bar{\Lambda}\Lambda + \bar{\Lambda}\Sigma^o$ + c.c. References in forward direction are from [ATH74] and [CHI66]. In the backward region we included $\frac{1}{2}\frac{d\sigma}{dt}$ ($\bar{\Lambda}\Sigma^o + \bar{\Sigma}^o\Lambda$) from [JAC78]. Predictions at WA13 beam momenta from Regge and CIM models, and at 12 GeV/c, and 16 GeV/c from the model by Preparata & Soffer are also shown.*

7.6 Discussion

At the beginning of this chapter we derived general model independent formulae for the d.c.s. and polarization. This was the basis of different parametrizations of the reaction amplitudes in different models.

REGGE BEHAVIOUR

We have discussed two Regge models, which consider the interacting hadrons as a whole. They are characterized by a large number of parameters (cf. [NAV76]). For the $\bar{\Lambda}\Lambda$ final state the number of helicity amplitudes was drastically reduced in order to control proliferation of parameters [SAL81].

The resulting d.c.s. predictions give a smooth transition from the well-known Regge behaved forward peak to the large angle region. Beyond $-t \sim 2$ $(GeV/c)^2$ exponential terms in Regge amplitudes cause a rapid fall-off in the d.c.s. which, at high energies, is incompatible with our data.

LARGE ANGLE DATA

An adequate description of high energy and large momentum transfer data needs assumptions about the inner structure of hadrons. We have adapted the CIM model describing elastic reactions to the hypercharge exchange processes of WA13. Apart from data at p_{lab} around 3 GeV/c the shape of the d.c.s. is qualitatively well described by a power law behaviour. But the CIM predictions seem to fall off slightly too rapidly for $K^0\Lambda$ final states (see fig. 7-7) and $\bar{\Lambda}\Lambda$ final states (fig. 7-11) at 7.8 GeV/c.

As was discussed in section 7.2, Regge models predict a backward peak in $\pi^- p \rightarrow K^0 \Lambda/\Sigma^0$ from u-channel exchange of Σ^0 trajectories. This is clearly confirmed by experiments at various energies (see fig. 7-6 and 7-7). So the CIM model incorrectly suppresses the backward peak.

As far as the reaction $\bar{p}p \rightarrow \bar{\Lambda}\Lambda/\Sigma^0$ is concerned, no backward peak is predicted from Regge models since the u-channel is exotic (cf. table 7-2). Our own data points and results from references plotted in fig. 7-11 are qualitatively in agreement with Regge behaviour at p_{lab} = 3 GeV/c and at low momentum transfer ($|t| < 2$ $(GeV/c)^2$), and they agree with the power law behaviour of the CIM model at 7.8 GeV/c and 11.7 GeV/c.

The massive quark model of Preparata & Soffer predicts a d.c.s. distribution which is much flatter than the CIM predictions. So, especially at $\cos\theta^*$ below 0., large differences appear between the two models.

As far as polarization phenomena are concerned, Preparata and Soffer predict strong negative polarizations at large angles in different elastic scattering processes. Calculations including the Λ polarization in hypercharge exchange reactions are under way [SOF82].

QUARK COUNTING LAW

We tried to fit fixed angle d.c.s. data to the power law $d\sigma/dt \sim s^{-n}$. Using on the one hand, our data points in $\pi^- p \rightarrow K^0 \Lambda/\Sigma^0$ at $\theta^* = 73$ and, on the other hand, extrapolating the d.c.s. According to CIM predictions until $\theta^* = 90^0$, we obtained values for the exponent n which are compatible both with the quark counting rule n = 8 and with the MQM prediction n = 9.

POLARIZATION

Strongly negative Λ- and $\bar{\Lambda}$-polarization and positive Σ^0-polarization found in WA13 confirm results from a number of other experiments (see e.g. fig. 6-10). In Regge models the interference terms responsible for the polarization vanish, in general, with increasing s, t, and u. Using the basic CIM exchange diagrams Matveev further developed the quark counting rule as is described in ref. [MAT79]. Assuming γ^5 - invariance of the scattering matrix M all helicity flip amplitudes vanish. This is true for meson-baryon and for baryon-baryon processes. Hence from eq. (7-13) and eq. (7-15) it follows that the polarization is vanishing.

Several attempts have been made to explain the fact that the hyperon polarization in general increases with increasing transverse momentum p_T. This correlation was found, for example, in the polarization of inclusively produced Λ-particles in p-p collisions at 300 GeV/c [HEL78]. Anderson et al. explained the Λ-polarization by a semi-classical model where a quark-antiquark pair $\bar{s}s$ is believed to be created in the colour field of a spin zero (ud) - diquark scattered with a certain transverse momentum [AND79].

In summary, the models we discussed in the preceding sections all have certain problems in describing polarization phenomena. On the other hand, polarization measurements are a rather delicate experimental issue since precise results require high statistics experiments. In the case of $\bar{p}p$ interactions experiments at the antiproton accumulator facility (AA) at CERN could, at low energies but high $\bar{p}$-beam intensities, complete polarization data over the full angular range for reactions where the d.c.s. distributions are already well established.

8. CONCLUSION

8. CONCLUSION

Out of $\sim$ 1.1 mio events recorded during the run of the WA13 experiment at the Omega spectrometer at CERN we have analyzed some 650 events corresponding mainly to the hypercharge exchange reactions $\pi^- p \to K^0\Lambda$, $\pi^- p \to K^0\Sigma^0$ and $\bar{p}p \to \bar{\Lambda}\Lambda$, $\bar{p}p \to \bar{\Lambda}\Sigma^0$ + c.c. at beam momenta between 3 and 12 GeV/c. Especially for the hyperon-antihyperon reaction channel there was an important lack of large angle data beyond p_{lab} = 3 GeV/c. At 7.8 GeV/c and 11.7 GeV/c we have measured values of the d.c.s. of the order of nb/(GeV/c)^2 which is about 3 orders of magnitude smaller than corresponding data at 3 GeV/c.

Our results concerning the d.c.s. at $|t|$-values below 2 (GeV/c)^2 are well described by Regge models.

In the large angle domain at higher energies one starts sensing the inner structure of hadrons. So realistic models should, on the one hand, account for the parton (or quark) content and the corresponding structure functions and, on the other hand, they have to propose a clear picture for the subprocesses in parton-parton interactions. A popular candidate is found in the constituent interchange model introduced by Blankenbecler et al. which, in contrast to perturbative QCD, assumes that constituent (quark) interchange, rather than gluon exchange, is dominant in hadronic interactions. Qualitatively the CIM predictions describe our d.c.s. distributions in a satisfactory manner.

Considering fixed angle d.c.s. as a function of energy, our experimental results are in agreement with the quark counting rule s^{-8} for meson-baryon scattering. The exponent we found in $\pi^- p \to K^0\Lambda$ is $n = 8.6 \pm .9$.

A surprisingly large and negative Λ and $\bar{\Lambda}$ polarization was measured in our experiment in $\pi^- p$ and $\bar{p}p$ interactions at various energies. This represents a clear test for theoretical models.

An interesting question remains unsolved concerning the existence or absence of a backward peak in the angular distribution of $\bar{p}p$ annihilation into both the $\bar{\Lambda}\Lambda$ and the $\bar{p}p$ final state. In this region the acceptance was suppressed by the WA13 trigger lay-out. Recently an experiment was undertaken at CERN [SON82] investigating the backward region in several hadronic interactions. So an answer to the above question may soon be given.

In summary, our results on d.c.s. and polarization have contributed new large angle data for exclusive hadronic processes with neutral strange particles in the final state. The WA13 experiment, reaching p_T values of about 2 GeV/c, has covered the intermediate range between well-known Regge behaved low energy data and "very" large p_T experiments (p_T up to 16 GeV/c) at the ISR. New experiments at high energies at the CERN $\bar{p}p$ collider and at high intensities at the antiproton accumulator AA may soon provide further interesting data in the high p_T domain.

R E F E R E N C E S

ABR71 M. Abramovich et al., Nucl. Phys. B27 (1971) 477.

AGU80 M. Aguilar-Benitez et al., Z. Physik C, Particles and Fields 6 (1980) 195-215.

AND79 B. Andersson, G. Gustafson, G. Ingelman, Phys. Lett. 85B (1979) 417.

ANG78 Angelis et al., Phys. Lett. 79B (1978) 505.

AST67 P. Astbury et al., Nucl. Instr. & Meth. 46 (1967) 61.

AST75 P. Astbury et al., Nucl. Phys. B99 (1975) 30.

ATH74 H.W. Atherton, B.R. French, J.P. Moebes, E. Quercigh, Nucl. Phys. B69 (1974) 1-14.

BAC81 L. Bachman, A. de Bellefon, N. Beusch, P. Billoir, M. Bogdanski, J.M. Brunet, L. Dorsaz, J.P. Dufey, A. Ferrer, J. Gago, B. Lefièvre, D. Perrin, R. Schwarz, P. Sonderegger, G. Tristram, A. Volte, Int. Conf. on High Energy Physics, Lisbon (1981).

BAD67 J. Badier, A. Bonnet, Ph. Briandet, B. Sadoulet, Phys. Lett. 25B (1967) 152.

BAL65 C. Baltay et al., Phys. Rev. 140B (1965) 1027.

BLA74 R. Blankenbecler, Proc. SLAC Summer Study I, SLAC-179 (1974) 361.

BEC78 H. Becker et al., Nucl. Phys. B141 (1978) 48.

BSL77 A. de Bellefon, F. Bourgeois, G. Schuler, C. Aubret, P. Benoit, P. Billoir, J.M. Brunet, G. Tristram, CERN/EF 77-1 (1977).

BEL78 A. de Bellefon, F. Bourgeois, J. Gago, G. Schuler, P. Sonderegger, C. Aubret, P. Benoit, J.M. Brunet, P. Billoir, P. Rivet, G. Tristram, A. Volte, M. Bogdanski, D. Perrin, R. Schwarz, XIX Int. Conf. on High Energy Physics, Tokyo (1978).

BEL81 A. de Bellefon, P. Billoir, M. Bogdanski, J.M. Brunet, J. Gago, B. Lefièvre, D. Perrin, R. Schwarz, P. Sonderegger, G. Tristram, A. Volte, Int. Conf. on High Energy Physics, Lisbon (1981).

BER61 J.P. Berge, F.T. Solmitz, H.O. Taft, Rev. of Scient. Instr., 32 (1961) 538.

BEU70 N. Beusch et al., Nucl. Phys. B19 (1970) 546.

BEU75 W. Beusch et al., Nucl. Phys. B99 (1975) 53.

BEU81 W. Beusch, CERN Internal Report, OM/SPS/81-1 (1981).

BIL82 P. Billoir, Thèse d'Etat, Paris (1982).

BOU70 F. Bourgeois, H. Grote, J.-C. Lasalle, Int. Conf. on Data Handling Systems in High Energy Physics, CERN 70-21 (1970) 831.

BOU80 C. Bourrely, E. Leader, J. Soffer, Phys. Rep. 59 (1980) 271.

BRO73 S.J. Brodsky, G.R. Farrar, Phys. Rev. Lett. 31 (1973) 1153.

BRU77 H. Brundiers et al., Nucl. Phys. B119 (1977) 349.

CHI66 C.Y. Chien et al., Phys. Rev. 152 (1966) 1171.

COL71 P.D.B. Collins, Phys. Rep. 1C (1971) 203.

CON78 A.P. Contogouris, R. Gaskell & S. Papadopoulos, Phys. Rev. D17 (1978) 2314.

DAR80 P. Darriulat, Ann. Rev. Nucl. Part. Sci. 30 (1980) 159-210.

DUF76 J.-P. Dufey, J.D. Wilson, CERN Internal Report, OM/SPS/76-18 (1976).

DUR64 L. Durand, J. Sandweiss, Phys. Rev. 135B (1964) 540.

EID73 A. Eide, P. Lehmann, A. Lundby, C. Baglin, P. Briandet, P. Fleury, P.J. Carlson, E. Johansson, M. Davier, V. Gracco, R. Morand, D. Treille, Nucl. Phys. B60 (1973) 173.

FER81 A. Ferrer et al., Nucl. Phys. B178 (1981) 373-391.

FIE77 R.D. Field, R.P. Feynman, Phys. Rev. D15 (1977) 2590.

FOL73 K.J. Foley, W.A. Love, S. Ozaki, E.D. Platner, A.C. Saulys, E.H. Willen, S.J. Lindenbaum, Phys. Rev. D8 (1973) 27.

GAG78 J. Gago, IV European Antiproton Symposium, Strasbourg (1978).

GAR70 P.B. Garbincius, L.G. Hyman, Phys. Rev. A2 (1970) 1834.

GRI68 GRIND Program, CERN TC program library (1968).

GUN73 J.F. Gunion, S.J. Brodsky, R. Blankenbecler, Phys. Rev. D8 (1973) 287.

HAG63 R. Hagedorn, "Relativistic Kinematics", Benjamin, New York (1963) 124-143.

HEL78 K. Heller et al., Phys. Rev. Lett. 41 (1978) 607.

HER79 Compilation of Cross Sections, CERN HERA 79-01 (1979).

HYD74 HYDRA System Manual, CERN (1974).

JAC59 M. Jacob, G.C. Wick, Annals of Physics 7 (1959) 404.

JAC62 J.D. Jackson, "Classical Electrodynamics", Wiley, New York (1962).

JAC78 S.M. Jacobs et al., Phys. Rev. D17 (1978) 1187.

JAY78 B. Jayet, M. Gailloud, Ph. Rosselet, V. Vuillemin, S. Vallet, M. Bogdanski, E. Jeannet, C.J. Campbell, J. Dawber, D.N. Edwards, Nuovo Cimento (1978) 371.

LAN73 P.V. Landshoff, J.C. Polkinghorne, Phys. Lett. 44B (1973) 293.

LOV80 a) P.F. Loverre, R. Armenteros, C. Dionisi, Ph. Gavillet, M.J. Losty, M. Mazzucato, D. Pennino, L. Dobrzynski, M.R. Pennington, M. Aguilar-Benitez, M.C. Albajar, A. Ferrando, J.A. Rubio, J. Salicio, I. Sjoegren, S. Rodebaeck, S.O. Holmgren, Z. Physik C, Particles and Fields 6 (1980) 283-294.

b) P.F. Loverre et al., Z. Physik C, Particles and Fields 6 (1980) 187.

MAT73 V.A. Matveev, R.M. Muradyan, A.N. Tavkhelidze, Lett. Nuovo Cim. 7 (1973) 719.

MAT79 V.A. Matveev, Proc. of JINR-CERN School, Vol. II, Hungary (1979) 56.

MUH70 P. Muehlemann, J.D. Wilson, CERN Report 70-17 (1970).

NAV76 H. Navelet, P.R. Stevens, Nucl. Phys. B96 (1976) 307.

PIL67 H. Pilkuhn, The Interaction of Hadrons, North-Holland (1967).

PLA71 G. Plaut, Nucl. Phys. B35 (1971) 221.

PLA76 D.E. Plane, CERN Internal Report SPS/EA/76-1 (1976).

PRE73 G. Preparata, Phys. Rev. D7 (1973) 2973.

PRE79 G. Preparata, J. Soffer, Phys. Lett. 86B (1979) 304.

PRE80 G. Preparata, J. Soffer, Phys. Lett. 93B (1980) 187.

REV80 Particle Data Group, Rev. Mod. Phys. 52 (1980) 45.

ROM75 ROMEO Description Manual, CERN (1975).

ROM80 A. Romana, Thèse d'Etat, Orsay (1980).

SAL81 M. Saleem, M. Ali, Lett. al Nuovo Cim. 32 (1981) 425.

SCH79 R. Schwarz, CERN Internal Report, DM/SPS/79-4 (1979).

SIV76 D. Sivers, S.J. Brodsky, R. Blankenbecler, Phys. Rep. 23C (1976) 1.

SOF82 J. Soffer, private communication.

SON82 P. Sonderegger, CERN proposal P 173, experiment WA 74 (1982).

SWA63 J.J. de Swart, Rev. of Mod. Phys. 35 (1963) 916.

TOW76 D. Townsend, CERN Internal Report, DM/SPS/76/11 (1976).

WAR73 C.E. Ward, I. Ambats, A. Lesnik, W.T. Meyer, D.R. Rust, D.D. Yovanovitch, Phys. Lett. 31 (1973) 1149.

WIL74 J. Wilson, CERN Internal Report, NP/OM.615 (1974).

WIM74 H. Wind, Nucl. Instr. & Meth. 115 (1974) 431.

A P P E N D I X

APPENDIX

A.1 Constrained Kinematical Fit

When testing a neutral particle hypothesis for a V0 or a reaction hypothesis for a 2-V0 final state, one has to satisfy energy and momentum conservation during the fit procedure.

A description of the general fit method based on linearization of the constraint equations and on the use of Lagrange multipliers in the definition of the chisquare function can be found, for example, in ref. [BER61].

The minimization procedure is based on the definition :

$$\boxed{\chi^2 = (X - X^m)^+ V^{-1} (X - X^m) + 2\alpha f(X)} \qquad \text{(A-1)}$$

where
- X^m = vector of n_m measurements,
- X = fitted vector (to be found),
- V = covariance matrix of X^m ,
- $f(X)$ = n_c constraint equations,
- α = Lagrange multipliers.

For minimization, one requires :

$$\frac{\partial \chi^2}{\partial x_k} = 0 \qquad k = 1,\ n_m \qquad \text{(A-2)}$$

and

$$\frac{\partial \chi^2}{\partial \alpha_\lambda} = 0 \qquad \lambda = 1,\ n_c \qquad \text{(A-3)}$$

For actual calculations, the constraint functions $f(X)$ are linearized. Let X^ν be the vector found at step ν. Then :

$$f_\lambda(X) = f_\lambda(X^\nu) + \sum_{j=1}^{n_m} \left.\frac{\partial f_\lambda}{\partial x_j}\right|_{x=x^\nu} (x_j - x_j^\nu) \tag{A-4}$$

Defining a $n_c \times n_m$ matrix with elements :

$$F_{\lambda i} = \frac{\partial f_\lambda}{\partial x_i}$$

the conditions expressed in eq. (A-2) and (A-3) yield a new estimate :

$$X = X^m - V\,F^+(X^\nu)\alpha \tag{A-5}$$

Introducing the definitions :

$$b = f(X^\nu) - F(X^\nu)X^\nu \tag{A-6}$$

$$H = F(X^\nu)\;V\;F^+(X^\nu)$$

$$E = V\;F^+(X^\nu)$$

we get at each step ν the new result :

$$\boxed{\begin{aligned}\alpha &= H^{-1}(F(X^\nu)X^m + b)\\ X &= X^m - E\alpha\end{aligned}} \tag{A-7}$$

The error matrix on the estimator X is :

$$\boxed{\langle \delta x\,\delta x\rangle = V - E\,H^{-1}E^+} \tag{A-8}$$

In practice it is important to choose a reasonable starting vector X^0 for the fit procedure. Hormally, this is the measured value X^m.

As a convergence criteria, one usually calculatea the variation of the χ^2-value and/or the variation of X with respect to the previoua atep. For exemple

$$<\left(\delta\chi^2(\alpha)\right)^2> = <\left(\sum_\lambda \frac{\partial\chi^2}{\partial\alpha_\lambda}\,\delta\alpha_\lambda\right)^2>$$

$$= f^+(X)\;H^{-1}\;f(X)\;<\;10^{-3}$$

and

$$<\left(\delta\chi^2(X)\right)^2> = <\left(\sum_k \frac{\partial\chi^2}{\partial x_k}\,\delta x_k\right)^2>$$

$$= \alpha^+\left(f(X^\nu) - F(X)\right)V\left(F(X^\nu) - F(X)\right)^+$$

$$< 10^{-3}\;.$$

A.2 Λ Spin Precession

The change of spin direction of a particle with constant magnetic moment has to be considered prior to calculation of its polarization.

1. PRECESSION IN c.m. SYSTEM

The most convenient way to evaluate the change of spin is to consider it in the particle rest system, where we know the equation of motion for the spin $\vec{S}'$ in a constant magnetic field $\vec{H}'$ from classical physics :

$$\boxed{\frac{d\vec{S}'}{d\tau} = g\,\frac{\mu_N}{\hbar}\,\vec{S}' \times \vec{H}'} \qquad \text{(A-9)}$$

the solution describes a precession with the Larmor frequency $\omega' = g\,\frac{\mu_N}{\hbar}\,H'$, μ_N is the nuclear magneton. (Notation: primed and unprimed variables refer to the c.m. and the lab. system respectively, $\tau = \frac{t}{\gamma}$ is the proper time of the particle.) Choosing $\hbar = C = 1$, we get :

$$\omega' = \frac{d\phi'}{d\tau} = g\;\mu_N\;H' \qquad \text{(A-10)}$$

To give an example, we get g = - 0,67 (Landé factor) for a Λ-particle. Thus

$$\omega' = -\;3.26\;H'\;\frac{\text{MHz}}{\text{kGauss}} \qquad (H' \text{ in kGauss}).$$

The magnitude and the direction of $\vec{H}'$ (c.m.s.) for a given magnetic field $\vec{H}$ (lab) follow from the Lorentz transformation for electromagnetic fields (see e.g. [JAC62]) :

$$\boxed{\begin{aligned} H'_{/\!/} &= H_{/\!/} \\ H'_{\perp} &= \gamma(H_{\perp} - \vec{\beta} \times \vec{E}) \end{aligned}} \qquad \text{(A-11)}$$

$H_{//}$ and $H_{\perp}$ (cf. fig. A-1) denote the components parallel and transverse to the direction of motion $\vec{\beta}$ of the particle. $\left(\vec{\beta} = \frac{\vec{v}}{c}, \quad \gamma = [1 - \frac{v^2}{c^2}]^{-1/2}\right)$. In this case $\vec{E} = 0$.

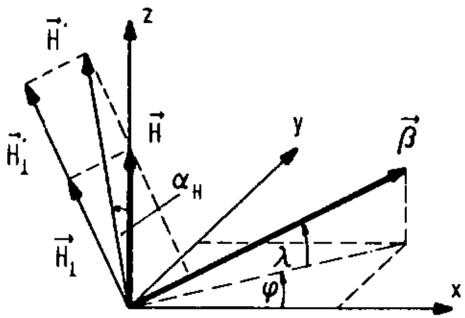

Fig. A-1 : Magnetic field and particle momentum in c.m. and lab system.

Finally, we give the transformation law for the particle spin in a more general approach to describe the Lorentz transformation of spin $\vec{S}$ and magnetic field $\vec{H}$ from the lab to the c.m. system, followed by the precession motion in the c.m.s. and, if this is wanted, the inverse transformations can be given by introducing 4-vectors for the particle velocity $V = (\gamma\vec{\beta},\gamma)$ and the particle spin $S = (\vec{S},S_4)$ and a 4-tensor for the electromagnetic field. Then, the Lorentz transform for S reads [HAG63] :

$$S = (\vec{S},S_4) = (S' + \vec{\beta}\,\frac{\gamma^2}{\gamma+1}\,\langle\vec{\beta}\cdot\vec{S}'\rangle\ ,\quad \gamma\langle\vec{\beta}\cdot\vec{S}'\rangle) \qquad \text{(A-12)}$$

$$S = (\vec{S},0) \qquad \text{in the rest frame.}$$

To get the inverse formule for eq. (A-11) and (A-12), one only has to interchange all primed and unprimed quantities and replace $\vec{\beta}$ by $-\vec{\beta}$.

Thus it follows that $\vec{S}' = \vec{S}$ for $\tau = 0$, as $\vec{S} \perp \vec{\beta}$ from parity conservation. Equation (A-12) also gives the direction of the particle spin in the lab system after considering a precession motion in the c.m.s. with the corresponding chenge of spin direction $\Delta\varepsilon$.

2. EXPLICIT CALCULATION OF THE PRECESSION MOTION

As shown in fig. A-1, we choose a magnetic field H (lab) in the z-direction of a Cartesian coordinate system. The angles ϕ and λ determine the direction of motion of the Λ-particle with momentum p_Λ. From equation (A-11), we obtain the angle α_H between $\vec{H}$ and $\vec{H}'$:

$$\alpha_H = \lambda - \arctan\left(\frac{1}{\gamma}\tan\lambda\right)$$

and

$$H' = (H^2 \sin^2\lambda + \gamma^2 H^2 \cos^2\lambda)^{1/2}$$

where

$$\gamma = \frac{E_\Lambda}{m_\Lambda}$$

spin at $\tau = 0$:

$$\vec{S}' = \vec{S}$$

Instead of using the c.m.s. coordinates (x',y',z'), we regard, for convenience, the time development of the spin $\vec{S}'$ in a coordinate system (x^*,y^*,z^*), where the z^*-axis is parallel to $\vec{H}'$ and the x^*-axis lies in the $\vec{H}'$, $\vec{\beta}$-plane.

A rotation R_1 around the z'-axis with angle ϕ and a subsequent rotation R_2 around the new y'-axis with angle α_H transforms (x',y',z')-coordinates into (x^*,y^*,z^*)-coordinates :

$$x^* = x' \cos\phi \cos\alpha_H + y' \sin\phi \cos\alpha_H + z' \sin\alpha_H \qquad \text{(A-13)}$$

$$y^* = - x' \sin\phi + y' \cos\phi$$

$$z^* = - x' \cos\phi \sin\alpha_H - y' \sin\phi \sin\alpha_H + z' \cos\alpha_H$$

(Example : $\vec{S}^* = R_2 \circ R_1 \cdot \vec{S}' = R_2 \circ R_1 \cdot \vec{S}$ for $\tau = 0$, $\vec{S}^* = (S_x^*, S_y^*, S_z^*)$).

Thus the spin precession around the z^*-sxis is simply given by the follow-ging equations (cf. fig. A-2).

$$\boxed{\begin{aligned} S_x^*(\tau) &= \sigma_0 \cos(\omega'\tau + \delta) \\ S_y^*(\tau) &= \sigma_0 \sin(\omega'\tau + \delta) \\ S_z^*(\tau) &= S_z^*(\tau=0) \end{aligned}} \qquad \text{(A-14)}$$

where $\tan\delta = S_y^*(\tau=0)/S_x^*(\tau=0)$.

$\Delta\varepsilon$ is defined as the sngle between the spin vector $\vec{S}^*(\tau=0)$, before pre-cession, and the vector $\vec{S}^*(\tau)$ after precession.

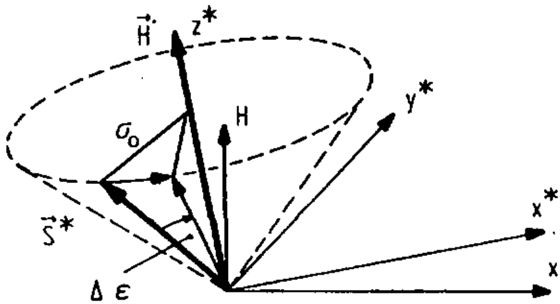

Fig. A-2 : Precession in c.m.s.

The new spin vector in the (x',y',z') c.m.s. is given by the inverse formula of (A-13) :

$$\vec{S}'(\tau) = R_1^{-1} \circ R_2^{-1}\, \vec{S}^*(\tau)$$

3. EXAMPLE

As an example, we plotted in fig. A-3 the dependence of the change in spin direction $\Delta\varepsilon$ as a function of the angles λ and ϕ (see fig. A-1) which define the direction of motion of the Λ particle in the laboratory frame.

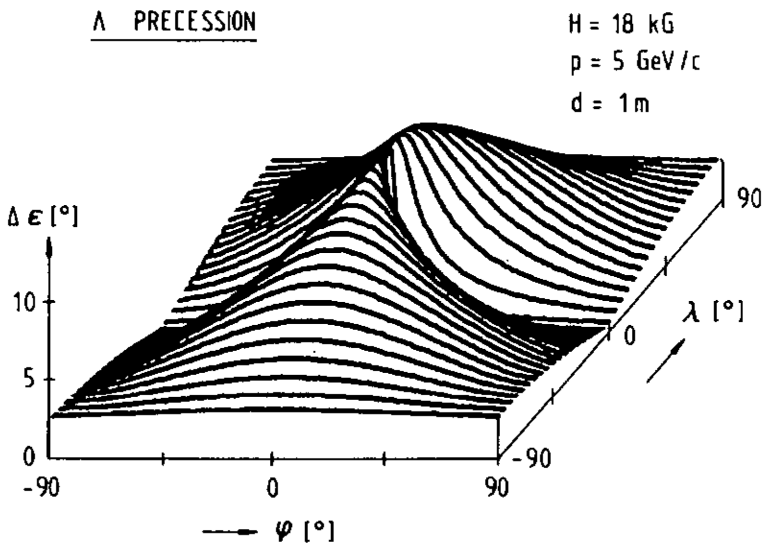

Fig. A-3 : Spin precession of 5 GeV/c Λ particles. $\Delta\varepsilon$ is the change in spin direction.

A.3 WA13 Elastic Reactions

This is a summary of the results for 2-prong data [BEL81] of WA13.
Table A-1 lists the fitted parameters of the d.c.s. parametrization :

$$\frac{d\sigma}{dt} = F(\cos\theta^*) \cdot \left(\frac{s}{s_o}\right)^{-n}$$

reaction	$F(0) \cdot 10^{23}$	n	χ^2	$\lvert t\rvert_{CIM}$	p_{beam}	Events used ($\lvert\cos\theta^*\rvert < .5$, $\lvert t\rvert > \lvert t\rvert_{CIM}$)	
1. $\bar{p}p \to \bar{p}p$	2.5	7.8 ± .8	.2	4.2	5 8 12	 208 70	Ref. this exp.
1'. $pp \to pp$	38 000	9.9 ± .3	19		5–19 (6 moments)		Ref.
2. $K^-p \to K^-p$	.59	7.3 ± .7	3.3		5 6.2 12 20	 - 14 2	Ref. Ref. this exp. Ref.
2'. $K^+p \to K^+p$	.53	7.1 ± 1.	9		5 12 20	 15 2	Ref. this exp. Ref.
2". $\bar{p}p \to K^-K^+$	178	10.2 ± 3.	3.6		5 8 12	 2 < 1	Ref. this exp.
3. $\pi^-p \to \pi^-p$	3.8	8.1 ± .3	5.4	3.2	5 8 9.75 12 20 30	112 276 10 4	this exp. Ref. this exp. Ref.
3'. $\pi^+p \to \pi^+p$	2.65	7.9 ± .3	1.9	3.2	5 10 12 20	 22	Ref. this exp. Ref.
3". $\bar{p}p \to \pi^+\pi^-$	.24	7.4 ± .9	.8	3.2	5 8 12	8 14 5	Ref. this exp.

Table A.1 : Results from WA13 elastic reactions.

REMERCIEMENTS

Je tiens à remercier tout particulièrement M. Peter Sonderegger du CERN pour ses nombreux conseils, des discussions fructueuses que nous avons eues, et de sa disponibilité permanente. Son intérêt pour ce travail n'a jamais cessé.

J'exprime ma gratitude au professeur Eric Jeannet, chef du groupe de physique corpusculaire, pour son accueil, ses conseils et sa confiance à mon égard.

Je n'oublie pas M. Michel Bogdanski qui m'a initié à la physique des hautes énergies, ni M. Jean-Bernard Jeanneret qui m'a fait profiter de son expérience.

Je dois remercier mes collaborateurs au CERN : MM. Denis Perrin, José Gago, Alain de Bellefon, Georges Schuler et François Bourgeois qui ont participé à l'expérience WA13.

Ma gratitude va à M. Jean-Michel Brunet pour son programme de simulation si transparent, ainsi qu'à ses collaborateurs au Collège de France : Alban Volte, Pierre Billoir, Gérard Tristram et Pierre Rivet.

Pendant l'analyse de l'expérience à Neuchâtel, j'ai profité du support informatique réalisé par MM. Christian Nussbaum et Pierre Tissot.
Je remercie M. P. Santschi et toute l'équipe du Centre de Calcul de l'EPFL pour leur collaboration efficace.
Je n'oublie pas Mmes Claudine Gretillat, Francine Jeanneret et Yvonne Grosjean, collaboratrices techniques du groupe, pour leur participation à l'analyse.

Je remercie M. Larry Bachman pour ses critiques constructives et la lecture du manuscrit de ce travail.
J'ai beaucoup apprécié maints calculs que M. Louis Fluri a fournis.

Pendant la rédaction de cette thèse, j'ai été heureux d'avoir un soutien constant apporté par mon amie Lily Khalily.

La plupart des dessins ont été exécutés avec minutie par M. Alain Schneiter.

La dactylographie parfaite a été réalisée en un temps record par Mme Blanche Serag-El-Dine.

Je tiens à remercier M. le professeur Jean Rossel d'avoir accepté d'être membre du jury de thèse.

C U R R I C U L U M   V I T A E

****

<u>NOM</u> : SCHWARZ Reinhard

<u>NE</u> : le 23 septembre 1950 à Grosskōris / Allemagne.

<u>NATIONALITE</u> : Allemande.

<u>ETUDES</u> :
- Daimler-Gymnasium à Schorndorf / Allemagne
- Université de Stuttgart (1971-1974 et 1975-1977, physique et mathématiques)
- Université de Warwick / Grande-Bretagne (1974-1975, mathématiques appliquées).

<u>DIPLOMES</u> : 1. Staatsexamen dans les branches Physique et Mathématiques à l'Université de Stuttgart.

<u>ACTIVITES</u> : Stages à IBM Deutschland (été 1973) et au CERN à Genève (été 1975).

Assistant à l'Institut de Physique de l'Université de Neuchâtel et préparation d'une thèse en physique des hautes énergies sous la direction du Prof. E. Jeannet (1977-1982).